

Modelling of Hypervelocity Impact on Foam-Core Sandwich Panel with Enhanced Capability for Orbital Debris Protection

by

Alexander James Bryan Jones

A Thesis submitted to the Faculty of Graduate Studies of

The University of Manitoba

In partial fulfilment of the requirements of the degree of

MASTER OF SCIENCE

Faculty of Engineering

University of Manitoba

Winnipeg

Copyright © 2018 by Alexander James Bryan Jones

ABSTRACT

Many commonly-used orbits are increasingly cluttered with orbital debris, posing a significant threat to space assets, which require enhanced protection. Recent studies demonstrate that foam-core structural and orbital debris protection panels are a promising alternative to single-function shields.

The objective of this thesis was to develop a two-dimensional model capable of simulating orbital debris impacts with foam-core panels cheaply and quickly, for initial shielding evaluation. The selected strategy combines explicit time integration, SPH, and FE methods, found by comparison of numerical and physical experiments.

It was found that the Johnson-Cook strength and failure equations, with the Mie-Gruneisen equation of state provide the best fit with selected test data. It was suggested that the multi-shock effect of open-cell foam ligaments could be replicated using a multi-layered structure of equivalent mass. The developed model predicted the outcome of all simulated NASA tests while completing the numerical analysis significantly faster than three-dimensional models.

ACKNOWLEDGEMENTS

I would like to sincerely thank Dr. Igor Telichev for his mentorship throughout the completion of this thesis, and for his invaluable editing skills. I would also like to thank the University of Manitoba MMOD Protection Group for their guidance when my simulations would go awry. Finally, I would like to thank my partner Nadine, without her patience and support this thesis would never have been completed.

CONTENTS

List of Tables	VII
Table of Figures	VIII
Glossary of Terms	XII
1 Introduction	1
1.1 Problem Statement	4
1.1.1 Motivation	5
1.1.2 Problem Definition	5
1.1.3 Proposed Solution	5
1.2 Thesis Formalization	6
1.2.1 Aim of the Thesis	6
1.2.2 Core Concepts within the Thesis	6
1.2.3 Thesis Statements	6
1.2.4 Scope of the Thesis	6
1.2.5 Research Questions	7
1.2.6 Thesis Organization	7
2 Literature Review	8
2.1 Hypervelocity Impact Physics	8
2.2 Review of MMOD Shielding Systems	11

2.2.1	Single-Function Shields	12
2.2.2	Multi-Functional Panels	18
2.3	Conclusions	23
3	Simulation Methodology	24
3.1	Selection of Computational Methods	27
3.1.1	Finite Element Method in the Lagrangian Formulation	27
3.1.2	SPH Solver	30
3.2	Components of Material Model	35
3.2.1	Equations of State	36
3.2.2	Strength Models	39
3.2.3	Failure Model	42
3.3	Calibration of Computational Model	43
3.3.1	SPH Particle Size	44
3.3.2	Erosion Factor	47
3.3.3	Summary	48
3.4	Evaluation of Material Equations	48
3.4.1	Impact Hole Size	49
3.4.2	Debris Cloud Shape	52
3.4.3	Impact response of Rear Wall	55
3.4.4	Summary	58

3.5	Conclusions	58
4	Modelling of HVI on Conventional Honeycomb Panels	59
4.1	2D Honeycomb Panel Simulation	61
4.1.1	Simulation Setup	63
4.1.2	Simulation Results	63
4.2	3D Honeycomb Panel Simulation	66
4.2.1	Simulation Setup	66
4.2.2	Simulation Results	67
4.3	Comparison of 2D and 3D Simulations	68
5	Modelling of HVI on Structural Foam Core Panels	71
5.1	Comparison Data	73
5.2	Model Design Approach	75
5.3	Penetration/Non-Penetration Mathematical Model	76
5.4	Foam Core Penetration Models	82
5.4.1	Model Foam with Flat Segments	83
5.4.2	Multi-Layer Foam Model	85
5.5	Conclusions	88
6	Validation of Foam-Core Models	89
6.1	10 PPI Foam	89
6.2	40 PPI Foam	93

6.3	Conclusions	95
7	Conclusions and Future Work	96
7.1	Conclusions and contributions	97
7.2	Limitations of the Analysis	98
7.3	Future Work	99
	References	102
	Appendix A	108

LIST OF TABLES

TABLE I: JOHNSON-COOK DATA FOR 6061-T6 ALUMINIUM.....	40
TABLE II: JOHNSON-COOK FAILURE CONSTANTS.....	43
TABLE III: MATERIAL EQUATION COMBINATIONS	49
TABLE IV: NASA TEST DATA.....	77
TABLE V: NUMERICAL SIMULATION RESULTS.....	80
TABLE VI: VALIDATION DATA FOR 10 PPI AND 2.0"-THICKNESS FOAM-CORE PANELS	89
TABLE VII: VALIDATION DATA FOR 10 PPI AND 0.5"-THICKNESS FOAM -CORE PANELS	91
TABLE VIII: VALIDATION DATA FOR 40 PPI AND 2.0"-THICKNESS FOAM -CORE PANELS	93
TABLE IX: VALIDATION DATA FOR 40 PPI AND 0.5"-THICKNESS FOAM -CORE PANELS	95

TABLE OF FIGURES

Figure 1.1: Classification of orbital debris sources	1
Figure 1.2: Depiction of MMOD particle orbits - NASA.....	2
Figure 1.3: Number of trackable debris objects in orbit by object type – NASA.....	4
Figure 2.1: Shock and reflection waves in a thin plate	9
Figure 2.2: Cratering (a), incipient spall (b), detached spall (c), and penetration (d) of an aluminium target - NASA.....	10
Figure 2.3: Render of Whipple shield elements.....	13
Figure 2.4: Ballistic limit curve for a Whipple and monolithic shield – NASA	14
Figure 2.5: Render of Stuffed Whipple elements	16
Figure 2.6: Render of MDB elements.....	17
Figure 2.7: Render of flexible shield elements	18
Figure 2.8: Channelling due to honeycomb cells – University of Manitoba	20
Figure 2.9: Comparison between two equivalent shield panels, foam core HITF04151 (left), and honeycomb HITF04150 (right). From top to bottom, front panel, impact cross section, and rear panel views - NASA	21
Figure 2.10: Ballistic limit curve for four structurally equivalent shield designs - NASA	22
Figure 3.1: Two-dimensional foam model extrapolated to three dimensions using axial (centre) and planar (right) symmetries.	25
Figure 3.2: Deformed Lagrange cells in a honeycomb core panel HVI simulation.	28
Figure 3.3: Explicit calculation method.....	30
Figure 3.4: Cubic B-spline smoothing function.....	34
Figure 3.5: Tillotson EOS curve	37

Figure 3.6: Impact hole with 0.015 mm particle size	45
Figure 3.7: Comparison of 0.01 mm experiments with min density 0.5 (left), and 0.55 (right) with runaway particles indicated in the red circles	46
Figure 3.8: A1076 (left) and A1077 (right) numerical experiments with an erosion factor of 1.5, showing penetration as expected from NASA physical experiments.	47
Figure 3.9: Image of bumper from physical test.....	50
Figure 3.10: 2D (a) and 3D (b) impact hole diameter results using combination 1, Mie-Gruneisen EOS, and Johnson-Cook strength model	50
Figure 3.11: 2D impact hole diameter using combination 4, Tillotson EOS and Steinberg-Guinan strength model.....	51
Figure 3.12: 3D impact hole diameter using combination 4, Puff EOS and Steinberg-Guinan strength model.....	52
Figure 3.13: Debris cloud shapes from NASA physical experiments (a), and 2D (b) and 3D (c) numerical experiments using material combination 1 at 0,1,2, and 3 μ s.....	53
Figure 3.14: Rear wall centre at simulation end in two dimensions.....	56
Figure 3.15: Rear wall centre at simulation end in three dimensions.....	57
Figure 4.1: NASA experiment HITF04150 showing damage to front panel (left), honeycomb core (centre) and rear panel (right) – NASA.	60
Figure 4.2: Geometry of two-dimensional honeycomb panel	60
Figure 4.3: Honeycomb cells with two cross sections.....	61
Figure 4.4: Simplified honeycomb cells	62
Figure 4.5: Close view of damage to honeycomb core – NASA.....	64
Figure 4.6: 2D Debris channelling.....	65

Figure 4.7: Damage at simulation end using FE for rear wall.	67
Figure 4.8: Damage at simulation end using an SPH body for rear wall.....	68
Figure 4.9: Concentration of debris in 3D honeycomb, corner concentration highlighted	69
Figure 4.10: Concentration of debris in 2D honeycomb.....	70
Figure 5.1: Recommended shielding design workflow	72
Figure 5.2: Damage to interior of foam core during experiment HITF04151 – adapted from [27] – NASA.....	73
Figure 5.3: Effect of PPI and density on metal foams of equal area	74
Figure 5.4: Foam reduction from realistic, randomized ligaments to simplified tessellated squares.....	76
Figure 5.5: Damage pattern of Whipple design with foam core mass added equally to both facesheets	82
Figure 5.6: Model of foam with flat segments: setup (a) and simulation results (b).....	85
Figure 5.7: Multi-layer model of foam: setup (a) and simulation results for the equal mass model (b) and equal ligament thickness model (c)	86
Figure 5.8: Illustration of positioning of inspection cylinders.....	87
Figure 5.9 Multi-layer equal ligament thickness model of foam with effective PPI (numerical experiment representing experiment HITF04151).....	88
Figure 6.1: Numerical experiment representing test HITF04161 (a) Rear wall of foam panel used in test HITF04161 (b) -NASA	90
Figure 6.2: One-layer simulation results of HITF03147-2 (a) and HITF03147-3 (b)	91
Figure 6.3: Two-layers simulation results of HITF03147-2 (a) and HITF03147-3 (b).....	92
Figure 6.4: Simulation results of HITF04152 (a) and HITF04163 (b).....	94

Figure 6.5: Simulation results of HITF05036-2 (a) and HITF05036-3 (b) 95

Figure 7.1: Paths of off-axis fragments through the layer of multilayer model of foam 99

Figure 7.2: Illustration of curved layered design 100

Figure 7.3: Application of curved layered design to simulation of oblique impact 100

GLOSSARY OF TERMS

ALE	Arbitrary Euler-Lagrange
CFD	Computational Fluid Dynamics
EOS	Equations of State
FE	Finite Element
GEO	Geosynchronous Orbit
GTO	Geosynchronous Transfer Orbit
HEO	High Earth Orbit
HVI	Hypervelocity Impact
ISS	International Space Station
J-C	Johnson-Cook
LEO	Low Earth Orbit
MEO	Middle Earth Orbit
MMOD	Micrometeoroid and Orbital Debris
MSA	Multi-Shock Action
MSS	Multi-Shock Shield
S-G	Steinberg-Guinan
SPH	Smoothed Particle Hydrodynamic
SWS	Stuffed Whipple Shield

1 INTRODUCTION

NASA defines orbital debris as “artificial space objects that serve no useful function—in orbit around the Earth” [1]. Orbital debris comes from a variety of sources, and can range in size from micrometre scale to rocket bodies. Various sources of orbital debris objects are shown in Figure 1.1.

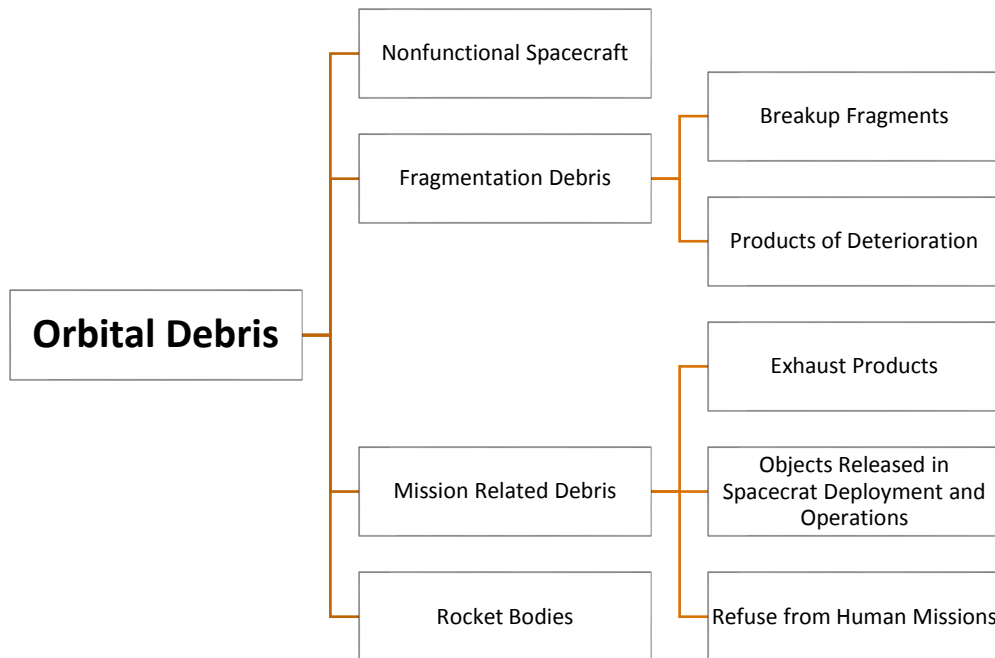


Figure 1.1: Classification of orbital debris sources [1]

Orbital debris poses a significant threat to space flight due to the very high velocities involved in a collision. Average impact velocities are in the range of 10-11 km/s, so even a small particle can cause catastrophic damage to satellites [2]. Orbital debris is a problem that agencies around the world are beginning to pay a lot more attention to. The average impact velocity is also dependent on the type of orbit the two colliding objects, summaries of which can be seen in Figure 1.2 which is labelled as follows:

A. Low Earth orbit (LEO) [3]

Perigee: 200-2000 km Apogee: 200-2000 km Velocity: 6.5-8.2 km/s
(depending on circularity of orbit)

B. 12-hour period middle Earth orbit (MEO) [3]

Perigee: 20,200 km Apogee: 20,200 km Velocity: 3.87 km/s

C. Active craft in geosynchronous orbit (GEO) [4]

Perigee: 35,786 km Apogee: 35,786 km Velocity: 3.1 km/s

D. Inactive craft in GEO [4]

Perigee: 35,786 km Apogee: 35,786 km Velocity: 3.1 km/s

E. Molniya orbit [4]

Perigee: 500 km Apogee: 39,900 km Velocity: 1.5 km/s-10km/s

F. GEO transfer orbit (GTO) [3]

Perigee: 100-500 km Apogee: >35,786 km Velocity: 1.64 km/s-9.88 km/s

G. Highly eccentric orbit (HEO) [5]

Perigee: <1000 km Apogee: >35,786 km Velocity: 1.64 km/s-9.88 km/s

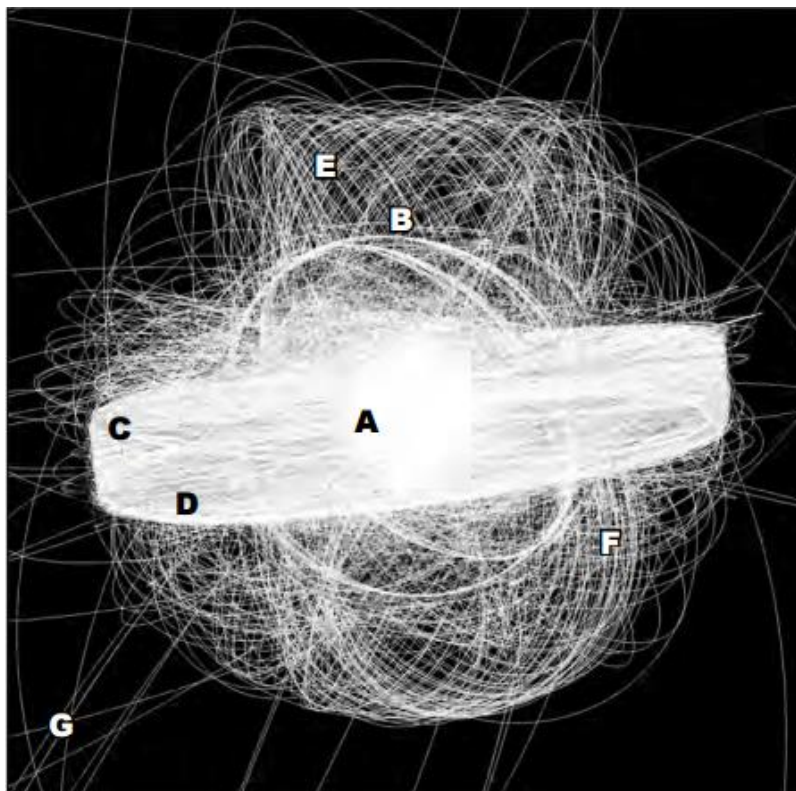


Figure 1.2: Depiction of MMOD particle orbits [6]- NASA

It can be seen from Figure 1.2 that the orbits most commonly used, LEO and GEO, have the highest density of micrometeorite and orbital debris (MMOD) particles. It follows that spacecraft in these orbits are at a higher risk than those in less frequently used orbits [6].

Orbital debris can be divided into two broad categories, debris that can be detected and tracked from Earth, and debris that cannot. Detectable debris is anything larger than 10 centimetres in diameter, but can be as large as non-functional satellites and used rocket stages. Undetectable debris is anything smaller than 10 centimetres in diameter, and includes objects as small as paint chips or solid rocket propellant particles. There are about 23,000 catalogued detectable debris objects being tracked by facilities like the Haystack Radio Telescope (Massachusetts), or the Teide Observatory (Spain). These objects can be avoided by functional satellites, and so do not pose a direct threat, however collisions between trackable debris produce many more non-trackable debris particles. The Space Surveillance Network estimates that there are over 500,000 non-trackable objects with a diameter over one centimetre, but several million smaller objects [7]. These smaller debris particles can still penetrate the satellite's structure with enough energy to cause catastrophic failure, and if a pressurized vessel is breached explosive decompression of the vessel will result.

There have been some efforts to both reduce the number of new debris objects being formed, and to move larger objects such as defunct satellites to safe orbits by either;

- Lowering the orbit of the satellite until it deorbits and re-enters the atmosphere.
- Moving the satellite into a parking orbit where it is unlikely to impact other objects.

These approaches are not universally followed, however, and the number of MMOD particles in Earth's orbit has steadily increased over time, as shown in Figure 1.3. With this increase, the

protection and mitigation of orbital debris become an important tool for future space missions. Canada has a keen interest in taking an active role in the orbital debris study. The Canadian Space Agency (CSA-ASC) joined the Inter-Agency Debris Coordination Committee (IADC) in 2010 and considers the orbital debris as a continuing high priority issue.

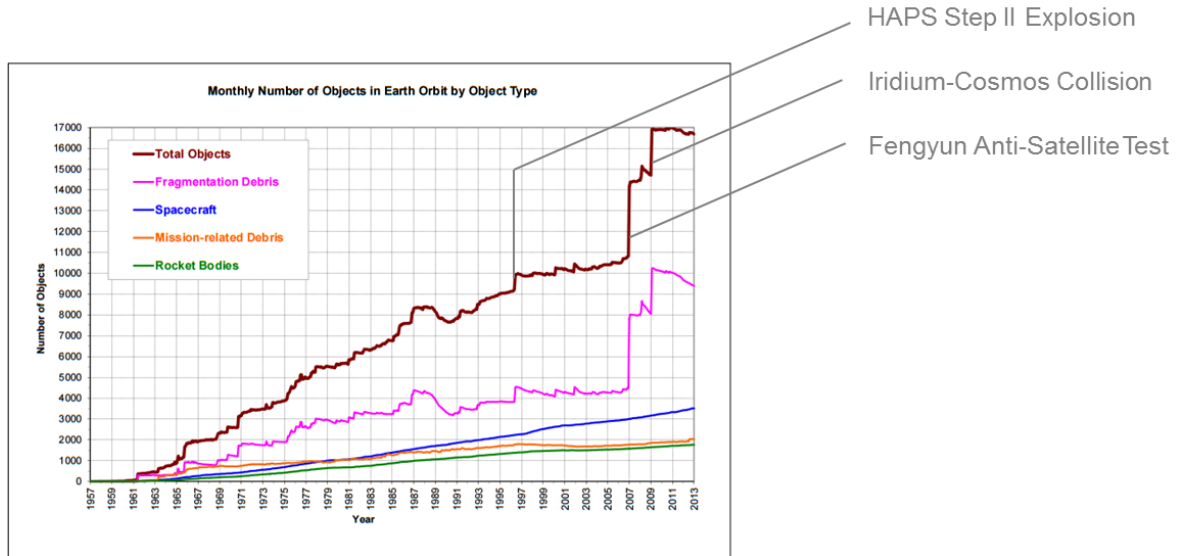


Figure 1.3: Number of trackable debris objects in orbit by object type [8] – NASA

1.1 PROBLEM STATEMENT

More satellites are launched every year, and national and international bodies are placing stricter requirements on satellite designers to reduce the formation of debris after an MMOD impact. This means that more time and resources must be spent designing appropriate MMOD shielding for current satellite missions, to keep orbital debris levels below critical levels. Current techniques of testing MMOD shielding designs either are extremely expensive - physical hypervelocity impact (HVI) experiments - or time consuming – three-dimensional numerical HVI experiments. HVI on simple shielding configurations can be simulated using two-dimensional numerical models, but structural shielding panels do not exhibit the type of symmetry that allows for easy reduction to two dimensions. The numerical and experimental studies [9] [10] demonstrated that multifunctional panels that integrate load-bearing and MMOD

protection capabilities are a promising alternative to single function shields. The present study is focused on the development of the simulation approach that will be able to accurately predict the impact behaviour of such panels.

1.1.1 Motivation

To reduce the cost of planning new satellite missions, a two-dimensional method of evaluating multifunctional MMOD shielding panels that is both time and resource efficient is desired. This would be used in concert with other methods to develop panel complying with design requirements for both structural support and MMOD protection with minimal expenditure of time and financial resources.

1.1.2 Problem Definition

While they do not require significant expenditures of time or money, two-dimensional numerical experiments rely on either radial or planar symmetry to extrapolate the results to three dimensions. Honeycomb and foam-core sandwich panels can be used as multifunctional panel components, but exhibit neither of these types of symmetry. Therefore, a method must be found to simulate the results of physical or three-dimensional numerical HVI experiments using these geometries, with minimal loss of accuracy.

1.1.3 Proposed Solution

The University of Manitoba team has already proposed a means of reducing the honeycomb-core sandwich panels to two dimensions, and this method is validated in chapter 4. To produce a method for simulating foam-core sandwich panels various material models must be evaluated to find the best combinations for compliance with test data. Using the selected combination various two-dimensional geometries will be examined, to determine which provides a result most like

NASA physical experimental data. The final goal of this thesis is to have successfully predicted the penetration or non-penetration of the NASA HVI experiments found in [11]. This will shorten the design time of weight-efficient combined structural and MMOD protection panels, and a commensurate reduction in launch costs [12].

1.2 THESIS FORMALIZATION

The sections below detail the specifics of this thesis:

1.2.1 Aim of the Thesis

The aim of this thesis is to develop an accurate method of performing two-dimensional HVI experiments on a foam-core sandwich multifunctional panel. This method will be validated against multiple physical experiments performed by NASA.

1.2.2 Core Concepts within the Thesis

This thesis deals primarily with the concepts of HVI physics and the simulation thereof. Specifically, various computational methods and characteristic material equations are described as needed within the thesis.

1.2.3 Thesis Statements

With this thesis, it will be shown that non-symmetric multifunctional panels undergoing HVI can be simulated in two dimensions with minimal losses in accuracy.

1.2.4 Scope of the Thesis

This thesis deals only with two multifunctional sandwich panel designs, honeycomb and foam-core. Explicit computational methods were used, as were the smoothed particle

hydrodynamic (SPH) and Lagrange finite element methods, in combination with six sets of characteristic material equations.

1.2.5 Research Questions

The research involved in this thesis is working towards answering the following questions:

- How should the numerical methods be selected and calibrated to properly simulate HVI events?
- Which combinations of characteristic material equations are most effective when simulating HVI events?
- Can known impacts involving honeycomb and foam-core sandwich panels be recreated in a two-dimensional numerical experiment?

1.2.6 Thesis Organization

This thesis consists of seven chapters including this Introduction. Chapter 2 begins with a review of modern shielding designs, and the physics behind HVI. Here the concept of a multifunctional shield that provides both protection and structural support together is introduced. In Chapter 3 the methodology of simulation of HVI events is discussed, including: a breakdown of different material models, details of the SPH and Lagrange solvers, and a review of the simulation parameter selection process. The combinations of these models are compared to actual HVI test data and ballistic limit equation (BLE) calculations to verify their effectiveness. Of interest is the conversion of the numerical systems to two dimensions, vastly decreasing the simulation run time compared to similar three-dimensional systems. Chapters 4 and 5 respectively detail the setup and numerical results for common multifunctional panel structures.

Chapter 4 is focused on honeycomb core sandwich panels, which are commonly used in modern satellites, whereas Chapter 5 deals with metal-foam core sandwich panels, which are a new development in shielding technology being researched by the University of Manitoba team, and how to simulate these panels in two dimensions. The method found in Chapter 5 is validated in Chapter 6, by using it to simulate multiple NASA experiments. Finally, Chapter 7 consists of the conclusions that can be drawn from this research, and future work that can be done using the presented work as a starting point.

2 LITERATURE REVIEW

There are two main topics in need of review before an effective discussion on simulated HVI events can be held. The first is the physics behind HVI events themselves, including shock and rarefaction wave formation and interaction. The second topic in need of review is the types of shielding systems already in use. Most shielding designs are single-purpose, meaning that they are added to the external surface of the satellite, but this report will focus on the design of multipurpose shielding panels, which function as both shielding and as a load-bearing structure.

2.1 HYPERVELOCITY IMPACT PHYSICS

During hypervelocity impact events, materials behave very differently than at more terrestrial speeds. Firstly, the kinetic energy during HVI is high enough to cause melting or vaporization of metals such as aluminium, which is commonly used in structural components of satellites. Secondly, the impact is so fast that it generates a shock wave which moves at high speed through the materials of impacting bodies [13]. Because the pressure caused by the shock

wave is generally much higher than σ_{yield} , the colliding solids can be treated as inviscid, compressible fluids [6]. When the shockwave hits a free surface, it reflects and turns from a compression wave into a high-intensity rarefaction wave, causing the material to fragment and form a cloud of ejecta. This is illustrated in Figure 2.1. As we can see, the shock waves (shown in red) first radiate away from the interface between the impactor and target. Then, as the waves strike the free surface around the interface, reflection waves (shown in blue) are formed and radiate toward the centre of the body, bounded by the shock waves. Debris is first ejected from the side of the plate on which the impact occurred, due to the tensile waves between the shock waves in each of the two bodies. Once the shockwave inside the plate reaches the rear wall, it causes another set of rarefaction waves to radiate back up the plate, forming a secondary zone of failure, which can cause internal damage, ejecta formation, or even penetration of the larger body [14].

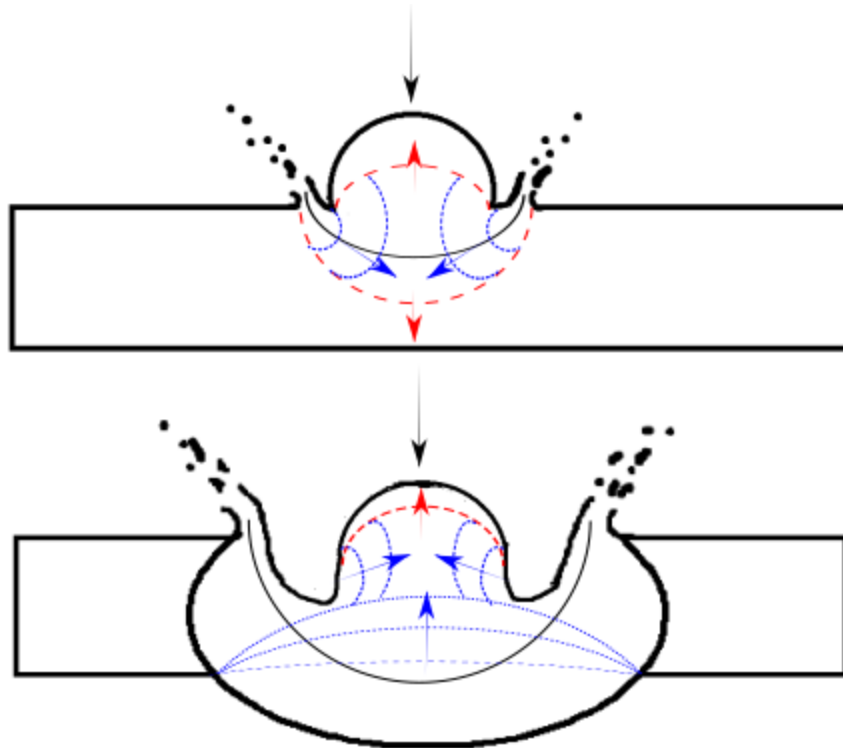


Figure 2.1: Shock and reflection waves in a thin plate

If the plate is sufficiently thick, the impactor will come to a rest within the plate, forming a crater. For thinner plates, the shockwaves will cause the plate to fail, allowing the projectile to penetrate the plate and form a secondary debris cloud which spreads out from the point of penetration. If the projectile comes to rest approximately 70% through the thickness of the plate, the plate will spall at the rear surface [15]. Both incipient and detached types of spall are shown in Figure 2.2. Incipient spall, discussed above, occurs when the wave interaction causes cracks in the plate to form and widen but not so far that they could reach the free surfaces of the plate. Detached spall occurs in the same manner as incipient spall, but the cracks are large enough to cause parts of the plate to detach from the whole.

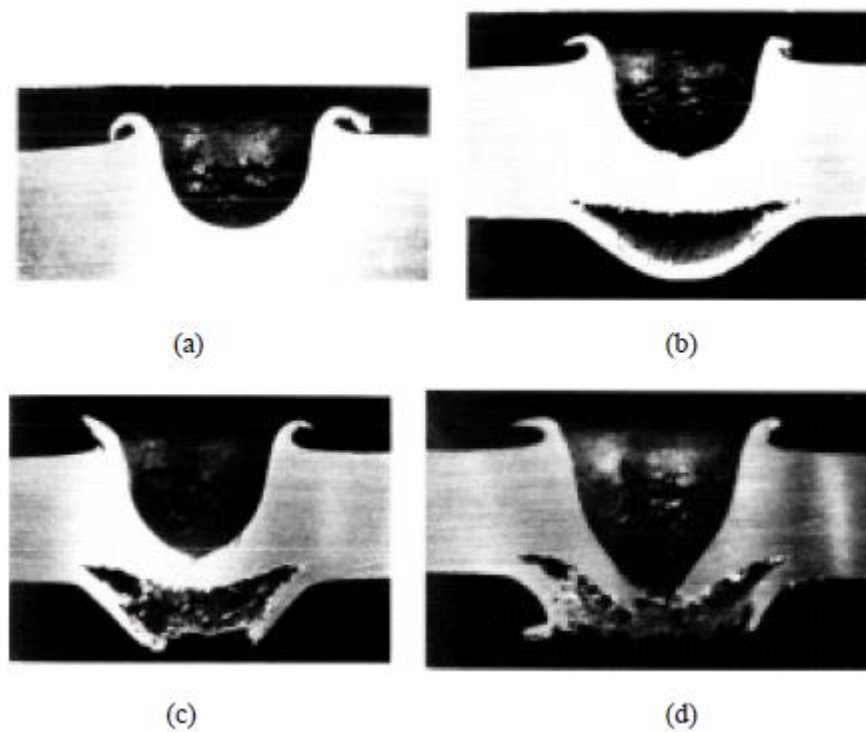


Figure 2.2: Cratering (a), incipient spall (b), detached spall (c), and penetration (d) of an aluminium target [6] - NASA

The thickness (t) at which perforation, incipient and detached spall will occur can be estimated using the empirical relationship obtained for the penetration depth P_{∞} . The following failure thresholds were defined in [6] for the aluminium plates: a) incipient spall: $t \geq 3 P_{\infty}$; b) detached spall: $t \geq 2.2 P_{\infty}$; c) perforation: $t \geq 1.8 P_{\infty}$.

2.2 REVIEW OF MMOD SHIELDING SYSTEMS

MMOD shielding comes in several configurations, the selection of which depends on the needs of the mission for which the shield is being designed. To maintain a given orbit, each satellite must move at a prescribed velocity, which means the maximum impact velocity with orbital debris will be twice the satellites orbital velocity in a head-on collision. Micrometeorites can travel at up to 72km/s, but their mass is very small, limiting the damage they cause to shielded structures. At a given impact velocity each shielding configuration has a certain critical projectile diameter (d_c) which represents the largest diameter MMOD particle that will not penetrate the inner surface of the shield.

Different satellite missions require different levels of protection, for example, a satellite that is going to use an uncommon orbit or is not meant to last for a long time, will have much less shielding with a lower d_c than a structure like the International Space Station (ISS) or the Hubble telescope. While we cannot track small particles with a diameter less than 10 cm, we do know the probability of different impact events occurring based upon observations of debris-causing events and past missions. This allows engineers to account for the likelihood of a certain impact event occurring, and design the satellite accordingly [16]. For example, the ISS is a large structure, and has been in orbit since 1998 [17]; this means that there is a higher probability of it to be impacted by a larger piece of debris compared to most other orbital structures, and since the ISS is manned such impacts are even less acceptable than those involving unmanned satellites. Therefore, the shielding for the space station was designed to be more robust than that used on satellites and to provide a higher level of protection for more critical components of the space station such as habitat pressurized modules or pressure vessels for the on-board systems. MMOD with a diameter greater than 10 cm are tracked using a network of ground and space-based

radars, which gives some time to move the satellite out of the way of the MMOD before the collision occurs. This provides an absolute upper bound for what size of debris a shield must protect against, however, based on the probabilistic analysis all existing shielding systems are developed for protection against debris particles under 1 cm in diameter [6] (with only a few exceptions made for ISS components). The primary goal is to develop a minimum weight shielding system, which can provide the necessary level of MMOD protection. This section of the thesis summarizes the status of MMOD protection systems methods which, in general, can be divided into two categories - *Single-function shields* and *Multi-functional panels*.

2.2.1 Single-Function Shields

Single-function shields provide the protection against orbital debris of up to a certain size to spacecraft without any additional functional capabilities. Below are presented the most common designs of single-function MMOD shields, along with the ballistic-limit equations for each configuration.

2.2.1.1 Whipple Shield

In 1947 Fred Whipple proposed using two aluminium sheets separated by a standoff distance (S) [18], as shown in Figure 2.3, as a lightweight alternative to monolithic shields. The outer wall, or bumper, is impacted first - breaking the projectile into small fragments. This has the effect of both removing some of the kinetic energy of the projectile, and spreading the resulting secondary debris over a larger area when it impacts the rear wall. The rear wall is often also the structural wall of the spacecraft, maintaining the shape, and if the spacecraft component is pressurized, the required internal pressure. The performance of a sample Whipple shield compared to a monolithic shield of the same total mass is given by the ballistic limit curve in Figure 2.4. The ballistic limit curve is the line shown, which gives the critical projectile diameter d_c for the shield

at each impact normal velocity (V_n), as the behaviour of the shield changes as the velocity increases, moving between the three regimes shown.



Figure 2.3: Render of Whipple shield elements

While at low velocities (“ballistic regime”), there is no measurable difference between a Whipple and a monolithic shield of the same weight, at speeds approaching that of most MMOD impacts [1], the Whipple Shield has a far higher d_c than the monolithic shield. This is because the first layer, known as a “bumper” absorbs kinetic energy from the projectile, turning the kinetic energy into heat and a pressure wave inside the material. This has the effect of breaking and possibly melting the particle, which lead to the formation of a secondary debris cloud. This allows spreading the momentum of debris cloud over a larger area of the inner wall, helping to prevent a material failure due to the impact.

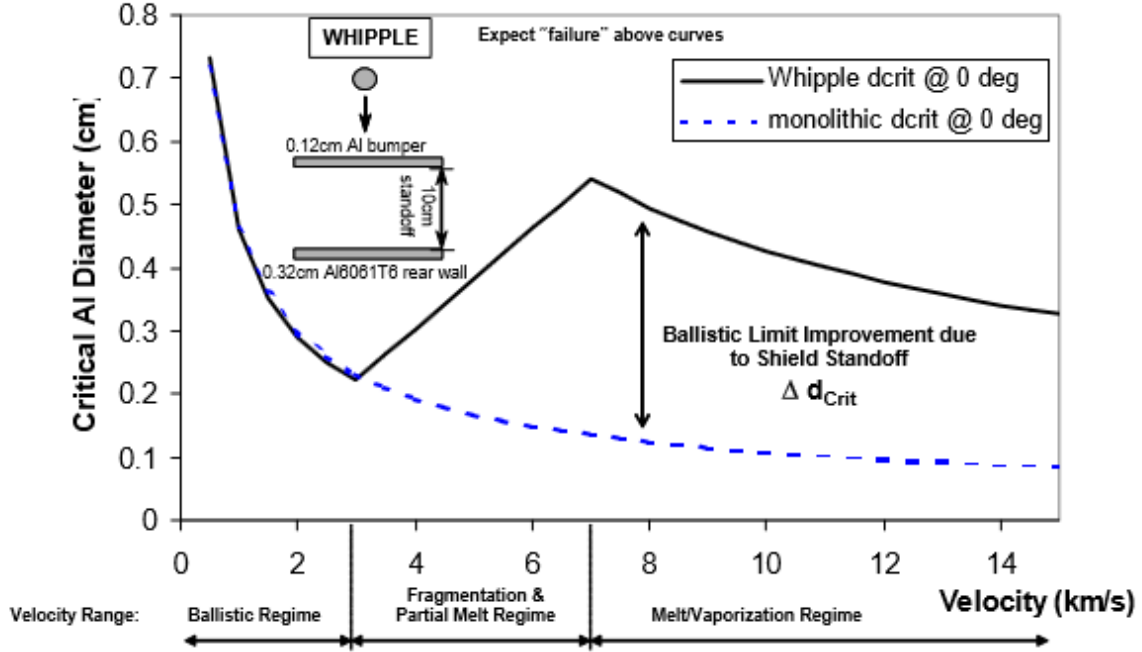


Figure 2.4: Ballistic limit curve for a Whipple and monolithic shield [7] – NASA

There are a variety of equations used to describe the behaviour of Whipple shields, depending on the construction of the shield and the normal impact velocity [6]. The equations described below are used to determine the thickness of the rear and bumper when impact velocity exceeds 7km/s. The input parameters are the projectile areal density (m_p), bumper density (ρ_b), projectile mass (M_p), rear wall yield stress (σ), as well as the projectile diameter, projectile density, standoff and normal velocity. The bumper thickness (t_b) is calculated by the formula;

$$t_b = c_b \frac{m_p}{\rho_b} \quad (1)$$

In this formula, the constant c_b depends on the ratio of the standoff to the projectile diameter, S/d , if $S/d < 30$, $c_b = 0.25$, and $c_b = 0.2$ if $S/d \geq 30$. To determine the corresponding rear wall thickness (t_w), we need to use the following equation;

$$t_w = c_w d^{0.5} (\rho_p \rho_b)^{\left(\frac{1}{6}\right)} (M_p)^{\left(\frac{1}{3}\right)} \left(\frac{V_n}{S^{0.5}}\right) \left(\frac{70}{\sigma}\right)^{0.5} \quad (2)$$

In this equation, the constant c_w is a constant with a value of $0.16 \text{ cm}^2\text{-sec}/(\text{g}^{2/3} \text{ km})$. These two equations allow for the design of a shield to withstand an impact with a particle of a certain size. To determine the critical projectile diameter of a shield that has already been built, one of three equations (depending on the impact velocity) can be used. Since the present work is focused on impacts between 3 and 7 km/s, the d_c for this impact velocity range is found as follows;

$$d_c = \left[\left(\frac{\left(t_w \left(\frac{\sigma}{40} \right)^{0.5} + t_b \right)^{\left(\frac{18}{19} \right)}}{\left(1.248 \rho_p^{0.5} \cos \theta \right)} \right) \times \left(1.75 - \frac{V_n}{4} \right) \right] \quad (3)$$

$$+ \left[\left(1.071 t_w^{\left(\frac{2}{3} \right)} \rho_p^{\left(\frac{-1}{3} \right)} \rho_b^{\left(\frac{-1}{9} \right)} S^{\left(\frac{1}{3} \right)} \left(\frac{\sigma}{70} \right)^{\left(\frac{1}{3} \right)} \right) \times \left(\frac{V_n}{4} - 0.75 \right) \right]$$

These equations can be used to predict the behaviour for different shield configurations, for example, honeycomb panels. However, this would not account for the honeycomb core, and for oblique impacts the equations for a MSS would be more accurate [2].

2.2.1.2 Stuffed Whipple Shield

A stuffed Whipple shield, shown in Figure 2.5, is an improvement over a regular Whipple shield. A stuffed Whipple shield also consists of a bumper and rear plate, separated by some distance. The protection performance is increased considerably using high-strength fabrics (like Kevlar) in combination with ceramic fabrics (like Nextel) as intermediate layers, or “stuffing”. Nextel is a flexible, ceramic fabric product manufactured by 3M Corporation which contains alumina, boron oxide and silica. Kevlar is a product of the E.I. DuPont Co.

Shield performance is improved compared to aluminium-only designs because Nextel ceramic fabric is better at shocking projectile fragments than aluminium, and Kevlar is better at

slowing debris cloud expansion than aluminium. Also, in comparison with an aluminium bumper the Nextel/Kevlar layers contribute smaller fragments into the debris cloud resulting in less rear wall damage [19], [20].



Figure 2.5: Render of Stuffed Whipple elements

2.2.1.3 Mesh Double-Bumper

The mesh double-bumper (MDB) shield is very similar in construction to a stuffed Whipple shield, with one addition. It has a metallic mesh layer placed before the bumper plate, to cause fragmentation of the MMOD particle prior to impact with the bumper, this mesh can be seen in Figure 2.6. This design is an improvement over previous iterations, because it has been shown that for a panel of equivalent areal density, a metallic mesh causes more fragmentation and a wider secondary debris cone than a solid metal plate [21]. It has been shown using both numerical simulations and HVI testing that the performance of a MDB shield against a relatively big particle (~1 cm) is also superior to that of a standard Whipple shield, as there is again more

particle melt and debris dispersal [22]. Compared to a solid plate the mesh layer produces fewer fragments upon impact, and it is better at breaking up particles than ceramic fabric [6]. This mesh layer can also be added to other shield configurations, to provide a first barrier to penetration by MMOD particles.

The protection capability of a MDB shield is strongly influenced by spatial constraints. This type of shielding is not suitable where a short standoff is needed. When the shield spacing to projectile diameter ratio is 15 or less, the Stuffed Whipple or deployable Multi-Shock shields are the best solutions.

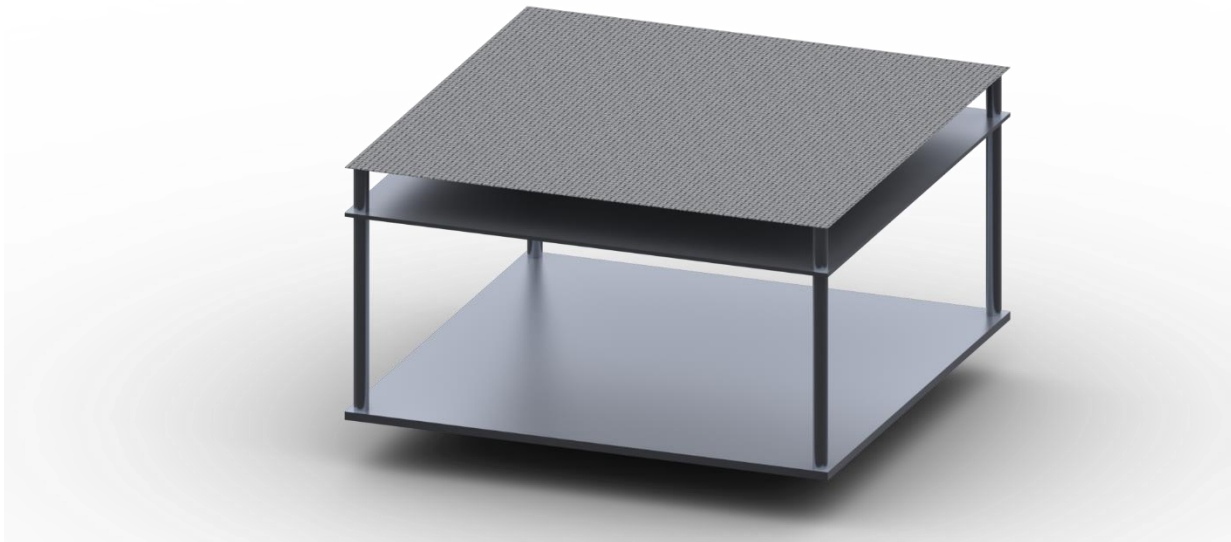


Figure 2.6: Render of MDB elements

2.2.1.4 Multi-Shock/Hybrid Multi-Shock Shield

As previously discussed, strong and lightweight fabrics are very effective at stopping MMOD particles without creating additional damaging fragments. However, a single layer of fabric is inefficient at fragmenting particles by itself; in previous designs an outer bumper was

used to cause the initial fragmentation, and the fabric layer was used to stop the debris from that impact.

In a multi-shock shield, several layers of fabric (e.g. ceramic fabric Nextel) are used in succession to repeatedly shock the projectile and debris cloud until the remaining fragments are no longer able to breach the primary structure; these layers are shown in Figure 2.7 in yellow. This design requires a large standoff between layers, but is much lighter than other designs so far discussed [23], [24]. The combination of high ballistic performance and flexibility makes fabric-based multi-shock shields especially well-suited for the inflatable manned space habitats [25].

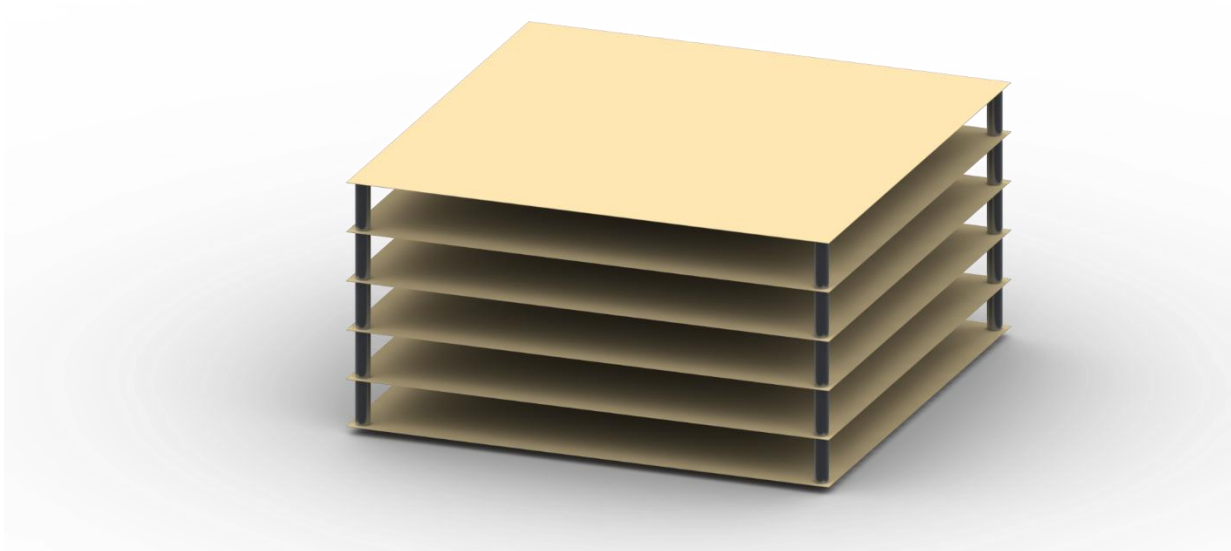


Figure 2.7: Render of flexible shield elements

2.2.2 Multi-Functional Panels

Many satellites simply do not have the capacity to have extra mass added to protect against MMOD impacts. Accordingly, a new trend is beginning where many researchers, including the University of Manitoba team, are investigating the possibility of combining structural support and MMOD protection into a single panel. The non-structural shield elements

such as spacers, fasteners, and supports can add an extra 35% to the mass of a Whipple Shield [12]. Therefore, a single structural and shielding panel is desirable to eliminate the need for this extra weight, and to provide some measure of protection from MMOD impacts.

Panels of this kind are generic elements of spacecraft load-bearing structures and may also perform as shielding systems at no extra cost for the mounting/fastening elements typically needed to attach an external shield.

The honeycomb sandwich panel is most common structural panel, which consists of two facesheets sandwiching a core of honeycomb cells. The sandwich panel is assumed to perform as shielding system; however, the honeycomb cells have the effect of channelling the debris cloud [6]. Thus, more secondary debris from the impact with the bumper hits the rear wall in the area directly below the impact site. However, when the MMOD particle impacts the plate at an angle, the honeycomb cells act instead as a series of thin bumpers, fracturing the particle and debris even further. Figure 2.8 shows a close view of a simulation with a 2 mm particle impacting a honeycomb panel at 7km/s [26]. We can see that the honeycomb channelled the debris from the impact, lowering the area over which the impact is applied to the rear wall, and this caused the rear wall to be penetrated by the debris cloud.

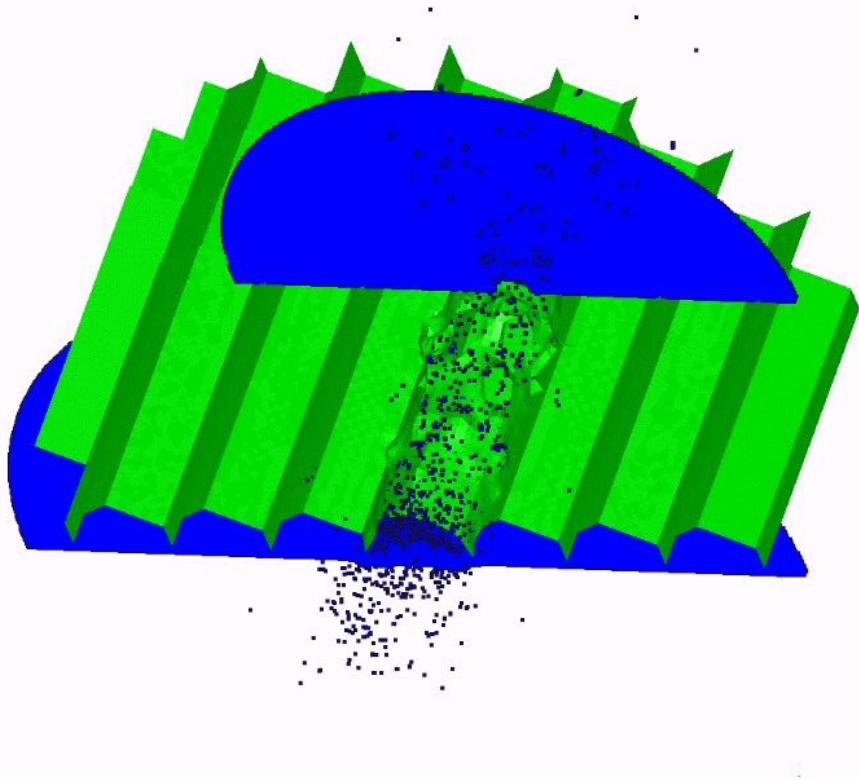
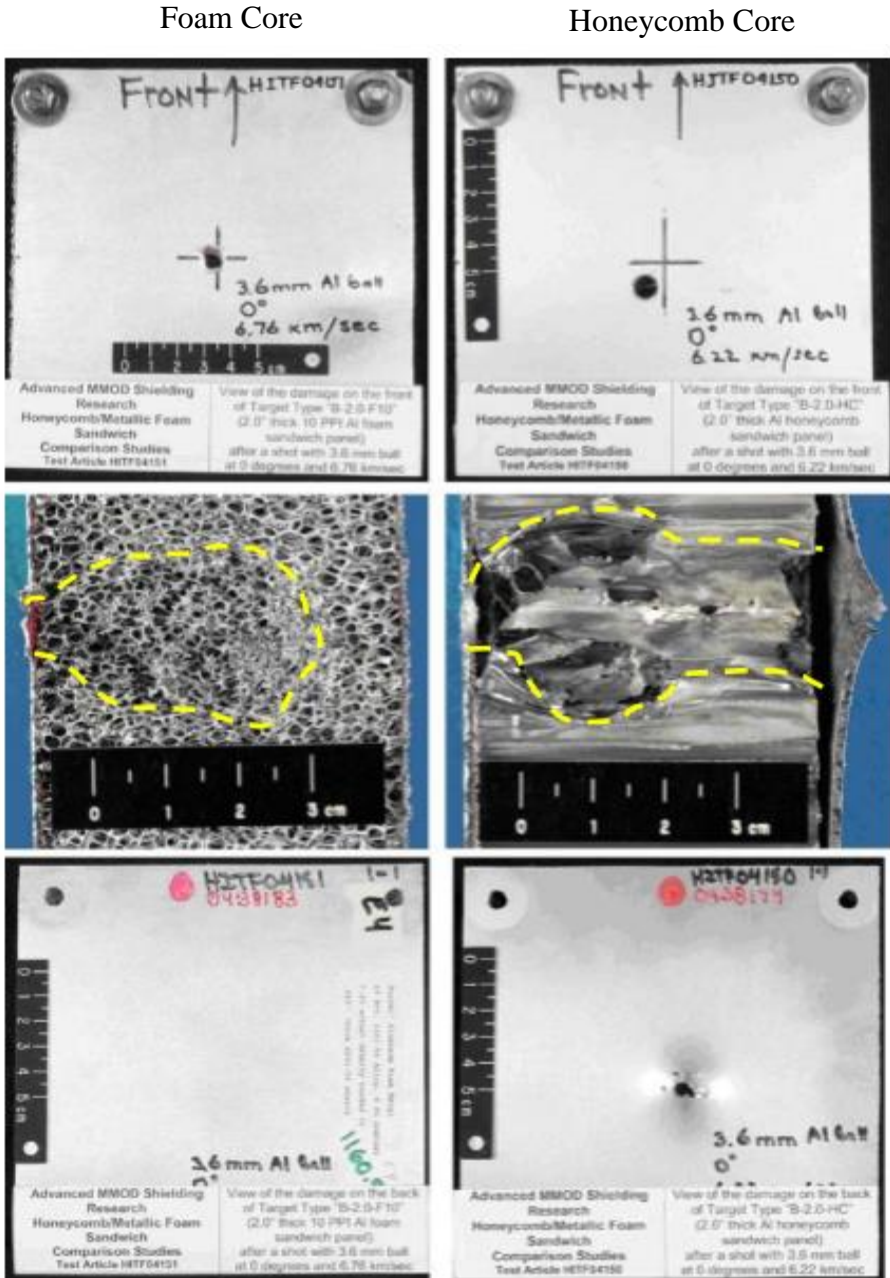


Figure 2.8: Channelling due to honeycomb cells [26] – University of Manitoba

Open-cell foam cored panels have increasingly been of interest to satellite manufacturers. The effectiveness of these panels has shown to be greater than that of similarly constructed honeycomb panels [27]. Figure 2.9 illustrates very different results obtained for two panel configurations of equal thickness subjected to an impact of 3.6 mm aluminium spherical particles at 6.5 km/s normal to the surface. We can observe the absence of such channelling in the foam-core panel as well as the multi-shock action of the foam ligaments on the debris cloud

propagating through the foam core. The latter has the effect of fragmenting and melting the debris at much lower velocities than in the traditional Whipple shield of similar dimensions.



- Front view showing impact site
- Cutaway view, showing penetration depth and damage shape
- Rear view, showing damage in the honeycomb panel – foam core is intact

Figure 2.9: Comparison between two equivalent shield panels, foam core HITF04151 (left), and honeycomb HITF04150 (right). From top to bottom, front panel, impact cross section, and rear panel views [26] - NASA

A complete melting of the MMOD particle is predicted to occur at around 8 km/s while impacting traditional Whipple shields, whereas the particle melts at only 4 km/s upon impact with a foam-core panel [12]. Figure 2.10 shows that the foam core panel can withstand impacts with larger particles than the Whipple and Stuffed Whipple configurations at velocities lower than approximately 5 km/s, and perform better than the honeycomb shields across all impact velocities.

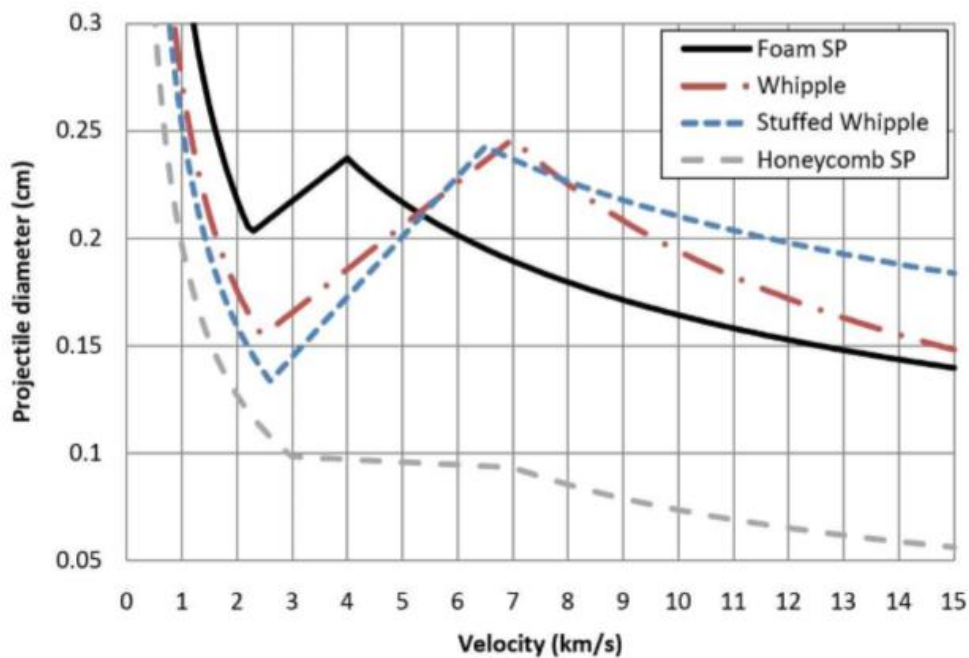


Figure 2.10: Ballistic limit curve for four structurally equivalent shield designs [28] - NASA

The comparison shields were chosen so that the total mass, including fasteners, was equal across all designs [28], but the honeycomb and foam panel shields are much thinner than the other designs. It is also important to note that the BLE curve in Figure 2.10 compares the Whipple and SWS to only one foam configuration; foams made with a greater or smaller number of pores per inch (PPI) will have different BLE curves. It is the intent of this paper to develop a tool which will allow comparing various honeycomb and foam configurations to determine how to surpass the performance of other shielding configurations at higher velocities.

2.3 CONCLUSIONS

MMOD shielding must be specifically designed for each satellite mission, which is an expensive and time-consuming process. While there is data on the design and performance of many common shielding types, it is still necessary to perform both physical and numerical experiments to validate the design selected. Most shielding configurations are designed to be attached to the primary structure, adding weight and volume to the spacecraft. This can be prohibitive in the case of smaller or cheaper satellites, where the projected mission lifespan and orbit make such protection unfeasible. In these circumstances, multifunctional sandwich panels can provide the required degree of protection at a lower cost. Many satellites use honeycomb core sandwich panels, but these panels channel secondary debris, nullifying one of the major benefits of MMOD shielding. Foam core sandwich panels represent the next step in multifunctional shielding design. Physical HVI experiments require equipment capable of accelerating projectiles to the speed of orbital debris and are therefore costly, so the development of a numerical tool for designers to use in conjunction with physical experiments will lower costs and design time. Simulating the actual 3D impact events in two dimensions further reduces design time, with minimal loss in accuracy. 2D modelling approach for numerical simulation of HVI on honeycomb multifunctional panels was recently developed by the University of Manitoba team, but there is no accepted methodology for 2D simulation of metal-foam core sandwich panels, which is where the research within this thesis will be focused.

3 SIMULATION METHODOLOGY

There are many decisions that must be made to produce a viable method of performing numerical HVI experiments, that do not have to be made when simulating less extreme deformation events. Firstly, the type of computational method must be selected; the smoothed particle hydrodynamic and Lagrange finite element methods are two techniques which are used to discretize the space simulated in the experiment. Explicit and implicit methods are used in conjunction with a space discretizing method to calculate the change in the experiment over time [29]. Secondly, once the computational methods have been selected, the correct material models must also be determined. Three components of material model are used in this analysis, an equation of state (EOS), a strength model, and a failure model. Finally, the geometry of the physical experiment must be created within the simulation. In three dimensions, the physical experiment can be reproduced faithfully, but if using only two dimensions the geometry must be altered to accommodate the type of symmetry used. The two types of symmetry are shown below in Figure 3.1, both types of symmetry are used during different experiments, as each has its own advantages and disadvantages, although only axial symmetry is used in this thesis.

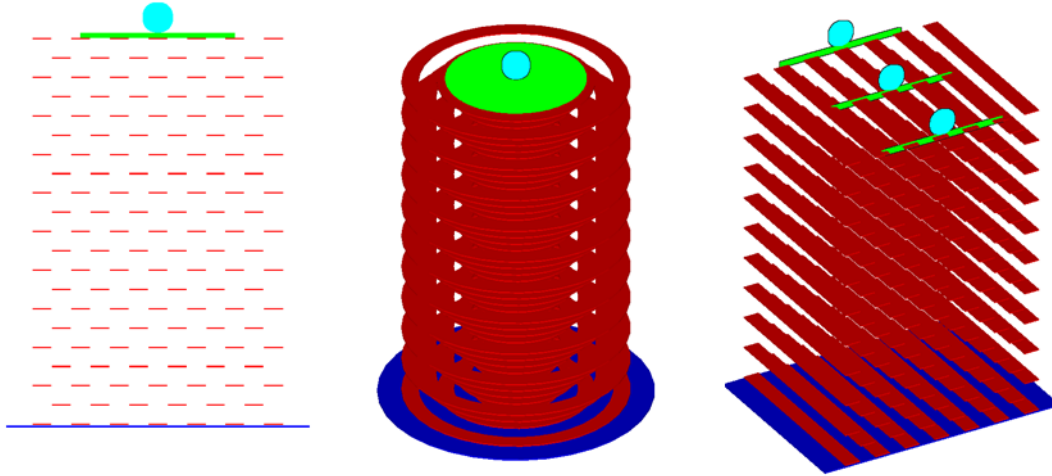


Figure 3.1: Two-dimensional foam model extrapolated to three dimensions using axial (centre) and planar (right) symmetries.

In this chapter, first a brief introduction to the various computational methods and material models used throughout this study is provided, material models not considered are listed in Appendix A, along with a brief note on why they were excluded. Following that the preliminary numerical experiments performed to refine the experiments methodology are described in detail. Two series of numerical experiments were conducted where the first one was needed to refine the computational methods, determining the best SPH particle size and Lagrange erosion factor to model HVI impacts. This set of experiments were conducted in axial symmetry only, as the symmetry has no effect on these parameters, and axial symmetry requires less processing time. The second series of numerical experiments was conducted to select the best combination of material models, and were also conducted using axial symmetry.

The procedure of numerical simulation method for determining both the SPH particle size and erosion factor is the same. Firstly, a set of data from either a physical or numerical HVI experiment or a BLE is selected; this data allows the numerical experiment behaviour to be compared to actual physical results, to determine if the model can authentically represent reality. Secondly, the physical experiments or results of the BLE are re-created within the simulation

space, these experiments were all performed on either Whipple shields, or just a thin bumper plate; therefore, in this stage axial symmetry was sufficient to represent all geometries, as plates and spheres exhibit this type of symmetry. Lastly, the numerical experiment is run, and the results are compared to the physical data. When comparing the numerical experiments to the available data the parameters of most interest are HVI test outcome, i.e. rear wall perforation/non-perforation, as well as the impact hole size and debris cloud shape. Once these tools are validated with these simpler geometries, other experiments can be performed to extend this method to honeycomb and foam core sandwich panels, which will be discussed in Chapters 4 and 5.

These numerical experiments were conducted in both two and three dimensions. The three-dimensional experiments are expected to more accurately model complex geometries and shield behaviours, but they demand a significant increase in computational and time resources compared to two-dimensional experiments. The two-dimensional model can be developed using either planar or radial symmetry to extrapolate the behaviour back into three dimensions. In both symmetry cases structures like a honeycomb or foam core cannot be exactly reproduced, as they display neither of these types of symmetry. The time to complete three-dimensional simulation can be enormous (from weeks to months). E.g., using a workstation with 4 cores running at 3.7 GHz and 128 Gb of RAM, a 3D simulation of HVI on honeycomb takes several weeks to completion, compared to several days for two-dimensional experiments. This means that for the purposes of reducing the time for development of a foam core sandwich panel shield, the two-dimensional experiments can be conducted first to refine a shielding design before being further tested in three-dimensional and physical experiments.

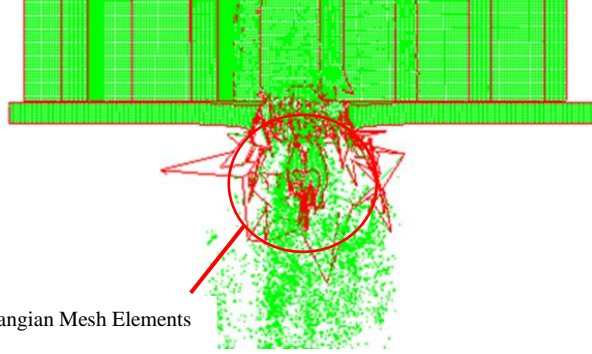
3.1 SELECTION OF COMPUTATIONAL METHODS

Two essential components of hypervelocity impacts which critically influence the choice of numerical approach for simulation are: penetration of a target, and fragmentation of both target and projectile. Two numerical techniques have been generally used to simulate penetration/fragmentation events are: the mesh-based Finite Element Method (FEM) in the Lagrangian formulation, and mesh-free Smoothed Particles Hydrodynamics (SPH) method. They are both effective at tracking materials' interfaces and establishing different contact conditions along interfaces of interacting bodies. This section reviews the above methods, and discuss the advantages of using explicit methods for experiments involving shock physics. Other modelling approaches, such as the Euler or Arbitrary Euler-Lagrange exist, but are better suited to fluid flow and explosive experiments respectively [29].

3.1.1 Finite Element Method in the Lagrangian Formulation

FEM in the Lagrangian formulation employs a mesh of computational nodes attached to the structure and the position and condition of each node is calculated at each point in time. As the time scales involved are very small, the small mesh sizes are needed to model shock waves which in turn requires the smaller difference between each point in time, known as the 'time step' [29]. One problem with HVI application of FEM in the Lagrangian formulation is associated with excessive mesh distortions and tangling at high deformation when grid lines have crossed over one another [30]. An example of this breakdown is shown in Figure 3.2, which came from an early experiment on honeycomb core sandwich panels, discussed in Chapter 4. Here, the large white shards are Lagrange cells which have been distorted beyond the computational limits of the program. This deficiency can be addressed by using of non-physical erosion algorithm. The algorithm prevents excessive mesh distortions and tangling by

eliminating those finite elements which belong to the domains where geometric strain has reached a critical value. That critical geometric strain is not known a priori and requires its calibration by comparison with experimental data.



Deformed Lagrangian Mesh Elements

Figure 3.2: Deformed Lagrange cells in a honeycomb core panel HVI simulation.

Another option to avoid the mesh distortion and tangling at high deformation is to employ a mesh-free method. The application of mesh-free Smoothed Particle Hydrodynamic method for HVI simulation is discussed in the following section.

3.1.1.1 Explicit Finite Element Methods

In situations where high strains and strain rates cause large local deformations with pressures orders of magnitude above σ_{yield} , explicit calculations are much more accurate than more commonly used implicit formulations [31]. The two methods are simply different means of integrating time steps over the course of the simulation. Implicit time integration uses the backwards-difference method, where the property of interest at time $n+1$ is dependent on its value at time n , and its time derivative at time $n+1$, given by the general equation;

$$u_i^{n+1} = u_i^n + \Delta t \left. \frac{\partial u}{\partial t} \right|_i^{n+1} + O(\Delta t) \quad (4)$$

which requires interpolation to solve. Explicit methods, for which an example calculation cycle is shown in Figure 3.3, require no interpolation to solve, as it uses the forward-difference method of time integration. This means that properties at $n+1$ are dependent only upon the values at time n , given by the general equation;

$$u_i^{n+1} = u_i^n + \Delta t \left. \frac{\partial u}{\partial t} \right|_i^n + O(\Delta t) \quad (5)$$

The advantage of implicit methods is that they are stable, independent of the size of the simulation time step. The size of the stable time step in an explicit method is linked to the size of the area of influence of the element being observed, call the element 'A'. If the time step is too small, the area of influence of A will be too small, and will not take neighbouring elements into account. However, if the time step is too large, too many neighbouring particles will be included in the area of influence. This stable time step can be much smaller than an equivalent implicit method, for the same computation resources. Therefore, explicit methods are selected for numerical experiments where high strain rates can lead to elastic and shock wave propagation, implicit methods will require more resources to obtain a fine enough time resolution to observe the effects of these waves [29].

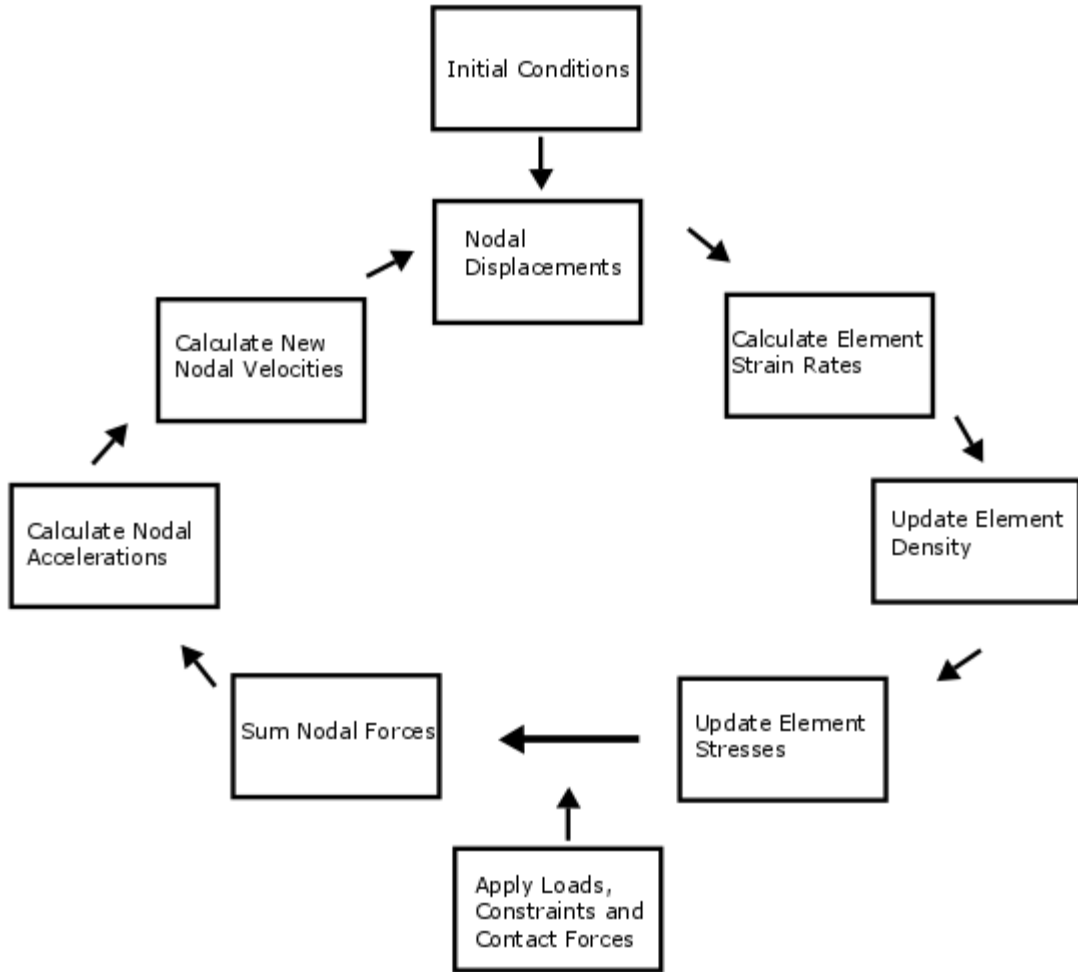


Figure 3.3: Explicit calculation method

3.1.2 SPH Solver

Smoothed Particle Hydrodynamics is a mesh-free form of the Lagrangian method, which was originally designed to simulate astronomical events, such as planetary or solar motion, but then modified to model material flow in cases of high deformations, such as when modelling liquids, brittle solids or HVI's. The SPH method uses particles to discretize continuum where each particle represents an element of mass with a specific material properties while acting as a focus for the computer to interpolate data upon. This makes a visual analysis of material locations very

easy, and removes the necessity of adding a mass conservation equation to the system, it is only necessary to keep the number of particles constant [32].

The first step when representing a body as a system of SPH particles is to find what is called the ‘kernel approximation’ of a desired function. The kernel approximation is a method of approximating a function using a process called a smoothing function. The second step, called ‘particle approximation’, is the discretizing of the continuous function of interest into a series of summations that represents the conditions the system is under at $t = 0$ [33]. The kernel approximation starts with a function, $f(x)$, of position, x :

$$f(x) = \iiint f(x')\delta(x - x')dx' \quad (6)$$

Where $\delta(x - x')$ is the Dirac delta function, but this cannot be used in the type of numerical modelling used in SPH calculations. Therefore, we approximate $f(x)$ with the kernel approximation, denoted $\langle f(x) \rangle$, where the Dirac delta function has been replaced by the smoothing function to give us

$$\langle f(x) \rangle \cong \iiint f(x')W(x - x', h)dx' \quad (7)$$

The new variable h is called the smoothing length, over which their properties are "smoothed" by a smoothing function. The smoothing length is what describes the area about a particle of interest where other particles have an influence upon it, this is called the ‘support area’ of the smoothing function about that particle. The smoothing function is arbitrary if it fulfils seven distinct criteria;

1. **The unity condition:** ensures a small level of consistency C^0 of the function, which means that the results of the simulation are a reasonable approximation of zero order terms, and is given mathematically as;

$$\iiint W(x - x', h) dx' = 1 \quad (8)$$

2. **The compact support condition:** If $|x - x'| > kh$, where k is some arbitrary scalar, equation 9 limits the area of effect acting on each SPH particle. This condition changes the general operation to a local operation about the particle of interest at x , which has a support area defined by $|x - x'| \leq kh$. Basically, the smoothing function must be equal to zero outside of this area.

$$W(x - x') = 0 \quad (9)$$

3. **The positivity condition:** at any given point within the support area, equation 10 below must be true. This is not required for the SPH method to reach a converging solution, but it prevents physically impossible results from being obtained.

$$W(x - x') \geq 0 \quad (10)$$

4. **The decay condition:** This corresponds with the compact support condition above, stating that the smoothing function must decay as we move further from the particle of interest. This makes sense physically, as we expect particles nearest to the one of interest to have the greatest effect upon it.
5. **The delta function property:** This means that as the smoothing length goes to zero, the approximate value must go towards the actual value, therefore the following must be true;

$$\lim_{h \rightarrow 0} W(x - x', h) = \delta(x - x'). \quad (11)$$

6. **The symmetric property:** This means that the smoothing function should be symmetric about the particle of interest, so that particles an equal distance away have an equal effect upon it. This is of course not true at the boundaries of the system, as the smoothing function does not exist outside of the material. The simulation must take steps to correct for this during calculations.
7. **The smoothness condition:** This helps ensure simulation accuracy by ensuring that the smoothing function and any relevant derivatives are continuous.

The most commonly used smoothing function used is called the cubic B-spline function, developed by Monaghan and Lattanzio [34]. Defining R as the distance between any two particles, $R = |x - x'|/h$, we write the cubic B-spline as;

$$W(R, h) = \alpha_d \times \begin{cases} \frac{2}{3} - R^2 + \frac{1}{2}R^3, & 0 \leq R < 1 \\ \frac{1}{6}(2 - R)^3, & 1 \leq R < 2 \\ 0, & R \geq 2 \end{cases} \quad (12)$$

In this equation, the value of α_d depends on the number of dimensions used, $\alpha_d = 1/h$, $15/7\pi h^2$, and $3/2\pi h^3$ in one, two, and three dimensions respectively. This results in a stable and accurate approximation of the original function [33], this function is shown below in Figure 3.4 where we can see that each successive particle from the one at $r/h = 0$ has a smaller influence on that particle.

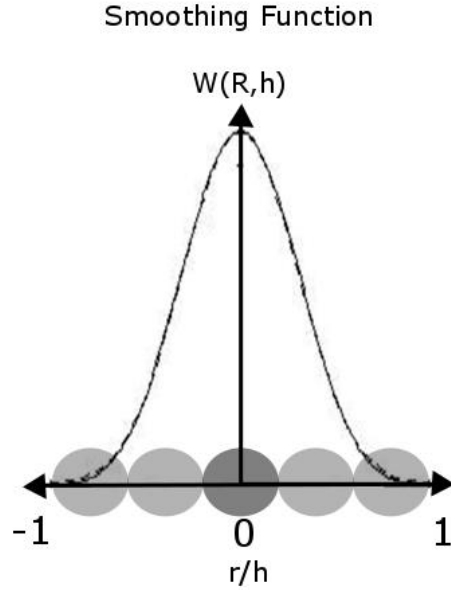


Figure 3.4: Cubic B-spline smoothing function

The next step, particle approximation, is done by creating an empty volume in the shape of the structure being simulated and then packing it with particles using a space-discretization model [33]. These particles each represent a distinct volume of the structure, and if we represent these volumes with an individual mass to density ratio, m_i/ρ_i , we can then discretize the earlier kernel approximation about each individual particle. This takes the form of a summation where N represents all the particles that have an influence on the particle of interest:

$$\langle f(x) \rangle = \sum_{i=1}^N \frac{m_i}{\rho_i} f(x_i) W(x - x_i, h) \quad (13)$$

This equation basically means that the value of a function of interest on a single particle can be approximated by averaging the value of that function for all other particles in the support area of the particle, weighted by the smoothing function. Again, the smoothing function weighting means that closer particles have a greater effect on the value of the function at a particle than

those farther away [33]. Using this method, a computer can calculate functions like velocity, strain, or position over time and throughout a body. To conclude, the SPH method has many advantages over traditional mesh-based Lagrangean formulations, especially when modelling high-deformation events, such as HVIs.

3.2 COMPONENTS OF MATERIAL MODEL

The three components of the material model are generally needed to simulate a HVI event, namely: the equation of state (EOS), the material strength model, and the failure model. Most hydrocodes have large databases of material models, including the above components.

Three EOS's, two strength models and one failure model were selected for analysis, other models not used and the reasons why are presented in Appendix A. Each combination of material equations will be run once in 2D, and once in 3D, to see which one better represents a real impact, when compared to NASA and University of Manitoba physical experimental results. The Mie-Gruneisen, Tillotson or Puff EOS, the Johnson-Cook or Steinberg-Guinan strength models, and the Johnson-Cook failure model were evaluated, and more information on each is presented below.

ANSYS Autodyn hydrocode was used to perform all numerical experiments in the present study. It is an explicit solver, also it has the capability to use both the Lagrange and SPH methods in tandem, and with any combination of material models. Autodyn is also capable of performing experiments in both two and three dimensions, and when working in three-dimensions it has the capability to leverage multiple CPU cores to speed up processing.

3.2.1 Equations of State

One of the material equations needed to accurately simulate metals under high strain rate stresses is the equation of state, as it accounts for the change in volume due to pressure or shock waves [35]. An equation of state is called that because it relates different state variables, those which depend only on the current state of the material. A simple example of an EOS is the ideal gas law, relating pressure, volume, and temperature. The EOS's used in these experiments are more complex, due to the processes involved. The Mie-Gruneisen, Tillotson, and Puff EOS's were compared, both the Tillotson and puff EOS' are more computationally expensive than the Mie-Gruneisen EOS, but more accurately reflect the physics of any situation involving a phase change. This means that they may not be worth the extra computation time for many designs, but when impact speeds exceed 7 km/s they are comparatively more useful.

3.2.1.1 *Mie-Gruneisen EOS*

One of the EOS' that will be evaluated in this report is the Mie-Gruneisen EOS, which is a relation between the volume and pressure of a solid that is undergoing a shock, like that experienced during an HVI. This equation relates the pressure (p) and internal energy (e) of a system at a given state to reference values (p_0), the reference pressure, and (e_0), the reference energy (both found at 0°K) using the formula:

$$p = p_0 + \frac{\Gamma(V)}{V} (e - e_0) \quad (14)$$

Here the coefficient $\Gamma(V)$, which is a function of volume (V), is called the Gruneisen coefficient, and is found using the formula:

$$\Gamma(V) = V \left(\frac{\partial p}{\partial e} \right)_V \quad (15)$$

In the Mie-Gruneisen EOS the values of the reference pressure and energy are found using the Hugoniot equation [35]. The Shock Hugoniot equation is derived experimentally, and relates the speed of the shockwave (V_s), to the bulk speed of sound in the solid (α) and the velocity of the particles behind the shockwave (u_p). The Hugoniot equation is as follows:

$$V_s = \alpha + su_p \quad (16)$$

The slope of the Hugoniot (s) is determined experimentally for each solid [36]. However, the Mie-Gruneisen EOS does not account for the melting of the material being modelled [14], and that can play an important role in the function of a foam-core shielding panel.

3.2.1.2 Tillotson EOS

The Tillotson EOS behaves very similarly to the Mie-Gruneisen EOS during low speed collisions, but has extra terms that account for circumstances where the energy from the impact is sufficient to melt or vaporize the metal. It separates the pressure-volume relationship into four distinct regions, as shown in Figure 3.5, which was adapted from [14]. The Tillotson EOS is very good at describing very high energy impacts, however it is not useful for situations where the

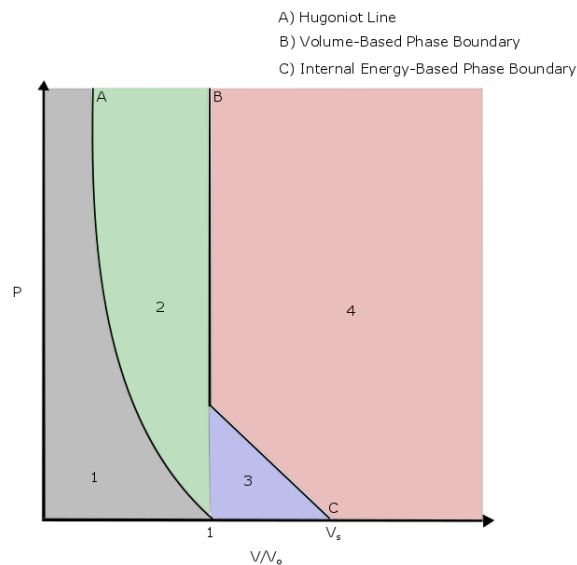


Figure 3.5: Tillotson EOS curve

material in question is undergoing tension, due to the lack of any negative terms on the pressure axis [37]. Region 1 is the area where the normalized volume (V/V_0) is below the Hugoniot line of the metal. In this region, there is no shock wave formation, and the material behaviour can be adequately described without the use of an equation of state. Regions 2 and 3 lie between the Hugoniot and phase boundary lines, and represent a solid material experiencing an isentropic expansion. Both regions use the following equation of state to relate the pressure and volume:

$$P = \left(a + \frac{b}{\frac{E}{E_0\eta^2} + 1} \right) \frac{E}{V} + A\mu + B\mu^2 \quad (17)$$

where P is the pressure, E is the specific internal energy, V is the specific volume, and a , b , A , B , and E_0 are constants. The constants a , b , and A are derived for each material, and then B and E_0 are selected to provide the best curve fit. The quantities η and μ are both related to the specific volume [37]. The only difference between regions 2 and 3 is that in region 2 the phase change is governed by volumetric changes, and in region 3 it is governed by changes in internal energy of the material, and that the values for μ are negative in this region [14].

Region 4 is the region where the material is assumed to have sublimated into a gas, with a large amount of the shockwaves energy being converted into heat. Figure 3.5 shows two boundaries to this region, the volume-based phase boundary and the internal energy-based phase boundary. The volume-based phase boundary line is usually chosen as the ambient density line, and the internal energy-based phase boundary is the line where the internal energy of the material is equal to the sublimation energy. The equation of state for region 4 was designed so that at high volumes it becomes the ideal gas equation of state, while still adequately

representing the material in regions between the solid and ideal gas stages. The EOS for region 4 is given by;

$$P = aE_p + \left(\frac{bE_p}{\frac{E}{E_0\eta^2} + 1} + A\mu e^{-\beta[(V/V_0)-1]} \right) e^{-\alpha[(V/V_0)-1]^2} \quad (18)$$

in which the second term approaches zero as volume increases with the constants α and β controlling the rate at which it does so.

3.2.1.3 Puff EOS

The puff EOS is also used to describe materials that undergo a phase transition from solid to vapour, but is described using only two regions. In the solid region, the material behaviour is described using the Gruneisen EOS. When the material reaches a state where the specific volume (V) is greater than the reference specific volume (V_0) the puff EOS requires the use of a more complex equation to account for the behaviour of the gas [38];

$$P = \rho \left[H + (\Gamma_0 - H) \left(\frac{\rho}{\rho_0} \right)^n \right] \left[E - E_s \left(1 - e^{-(N_0\rho_0/\rho)(1-(\rho_0/\rho))} \right) \right] \quad (19)$$

This equation requires the sublimation energy (E_s), density (ρ), reference density (ρ_0), the specific heat ratio of the gas (γ), the constants n , N_0 , and H , and a Hugoniot parameter (Γ_0).

3.2.2 Strength Models

Strength models in general relate the stresses applied to a material, and the strains that these stresses cause. During HVI's the temperatures of the materials involved are high enough to alter the strength of the materials. As well, the rate at which the strain is applied is much higher than in many other applications, which can change the deformation behaviour of the metal as

well [29]. As such the strength models for the simulation of HVI event must be able to predict the deformation behaviour of ductile metals under these extreme conditions. Two strength models, specifically the Johnson-Cook and Steinberg-Guinan strength models, were evaluated in term of their performance; each model is described briefly in the following sub-sections.

3.2.2.1 Johnson-Cook Strength

The Johnson-Cook (J-C) strength model was derived empirically for use with computer simulations of high strain problems, and accounts for the material strain, strain rate, and temperature softening independently [39]:

$$\sigma_{yield} = [A + B\varepsilon_p^n][1 + C \log \dot{\varepsilon}_p^*][1 - T_H^m] \quad (20)$$

In this formula, (ε_p) is the effective plastic strain, $(\dot{\varepsilon}_p^*)$ is the normalized effective plastic strain rate in s^{-1} , and (T_H) is called the homologous temperature, and it is a non-dimensional quantity given by:

$$T_H = \frac{T - T_{transition}}{T_{melt} - T_{transition}} \quad (21)$$

$(T_{transition})$ is the temperature at which a material moves from the brittle to ductile failure regime. The constants A , B , C , n , and m are all material properties that must be derived experimentally, in conditions at or below $T_{transition}$. For 6061-T6 aluminium, a commonly used aluminium alloy, the following data in TABLE I was obtained by Fish, Oskay, and Fan [40].

TABLE I: JOHNSON-COOK DATA FOR 6061-T6 ALUMINIUM [40]

A	B	C	N	M	T_{melt}	$T_{transition}$
289.6MPa	203.4MPa	0.011	0.35	1.34	925.37K	294.26K

3.2.2.2 Steinberg-Guinan Strength

The Steinberg-Guinan (S-G) strength model is also developed for use in high strain-rate applications, but unlike the J-C strength model the S-G strength model accounts for the effect strain rate has on the other components of the yield strength. This makes the S-G model more accurate for metals that are very sensitive to strain rate, but it is more computationally expensive than the J-C model [14]. It uses two main formulas, one to find the shear modulus (G), and the other to find σ_{yield} , which together describe the yield conditions using strain, strain rate, and temperature effects. The shear modulus is defined as following:

$$G = G_0 \left[1 + \left(\frac{G'_P}{G_0} \right) \left(\frac{P}{\left(\frac{V_0}{V} \right)^{1/3}} \right) + \left(\frac{G'_T}{G_0} \right) (T - 300) \right] \quad (22)$$

where (G_0) is the shear modulus at 300K and zero pressure; (G'_P) and (G'_T) are the derivatives of G with respect to pressure and temperature respectively.

To find the yield stress, several new parameters, namely the initial yield stress (σ_0), the strain hardening parameters (β) and (n), the initial plastic strain (ε_i) which is normally zero, and the pressure and temperature derivatives of the yield stress (σ'_P) and (σ'_T) are required [41]:

$$\sigma_{yield} = \sigma_0 [1 + \beta(\varepsilon_p + \varepsilon_i)]^n \left[1 + \left(\frac{\sigma'_P}{\sigma_0} \right) \left(\frac{P}{\left(\frac{V_0}{V} \right)^{1/3}} \right) + \left(\frac{\sigma'_T}{G_0} \right) (T - 300) \right] \quad (23)$$

This equation is more complex than that of the J-C model, that is why the S-G model takes more computing time to use, but can be more accurate in many high temperature and pressure applications [42].

3.2.3 Failure Model

Two sets of calculations are needed to describe the process of failure [35]. The first set of calculations describes the failure initiation, and then the second describes the post failure response. The post failure response is split into two regimes, instantaneous and gradual failure, representing the immediate and delayed effects of the initial failure. HVI simulations occur over the scale of microseconds, so we can assume that all failure is instantaneous. The tensile pressure, Johnson-Cook, and Grady spall failure models are all ductile material failure models [35]. Of these, the Johnson-Cook failure model is recommended for use in high deformation applications, and data exists for this model over a range of materials. The Johnson-Cook failure model is broken down into three factors, which are multiplied together to obtain a value for the failure strain (ϵ_f). The three factors are the stress dependence, the strain rate dependence, and the temperature dependence. Because these factors are independent, materials where a change in one of these factors can alter the materials response to the others are not well modelled by the Johnson-Cook method. However, metals commonly used in the aerospace industry such as aluminium and titanium are not affected by this limitation [43].

The basis of the Johnson-Cook failure model is the cumulative damage law, where a damage constant (D) is used to represent the degree to which the material has been deformed. A value of $D=0$ means that the material is not deformed, and a value of $D=1$ means that the material has failed. The formulation of D is given by:

$$D = \sum \frac{\Delta\epsilon}{\epsilon_f} \quad (24)$$

where $\Delta\epsilon$ is the incremental change in the local strain of the material at a point in time.

The failure strain (ϵ_f) depends on both the material and the loading of the system. It is found using the formula:

$$\epsilon_f = [D_1 + D_2 e^{(D_3 \sigma^*)}] [1 + D_4 \ln(\dot{\epsilon}_p^*)] [1 + D_5 T^*] \quad (25)$$

where σ^* is the mean stress normalized by the effective stress; $\dot{\epsilon}_p^*$ and T_H reappear from the formulation of the Johnson-Cook strength. Each material also has a set of five constants, D_1 - D_5 , that help characterize the contribution of each of the three factors to the failure strain. The values of five D -constants obtained by Leuser, Kay, and LeBlanc [44] for 6061-T6 aluminium are presented here in TABLE II.

TABLE II: JOHNSON-COOK FAILURE CONSTANTS [44]

D_1	D_2	D_3	D_4	D_5
-0.77	1.45	-0.47	0	1.60

3.3 CALIBRATION OF COMPUTATIONAL MODEL

To run a simulation that gives results as much like physical tests as possible, two simulation parameters must be calibrated, the SPH particle size and the erosion factor of the rear wall. These two parameters are not analogous to any aspect of a physical system, but calibration of these parameters is necessary for successfully modelling a physical system. The SPH particle size is analogous to the mesh size in a finite element simulation. The smaller the particle size, the more accurate the simulation will be - to a limit - but the longer the simulation will take to run. The erosion factor is needed because the rear wall of the model is a Lagrangean Finite Element Model, and so at high strains the simulation must allow the nodes within it to ‘erode’. This prevents non-physical results due to the mesh warping too far, but allows the simulation to

continue running. Autodyn still accounts for the mass and energy of the eroded nodes, but there is some loss of accuracy, therefore the erosion factor must fall within a specific range.

The calibration of each of these parameters is presented below. The calibration of the SPH particle size, presented in section 3.3.1, is performed by recreating an impact between a thin plate and a small aluminium particle, in the same configuration as used in the recent physical experiments conducted by the University of Manitoba team [10]. The model consists of only SPH particles, as both the projectile and thin plate are predicted to deform greatly. The calibration of the erosion factor, presented in section 3.3.2, is performed by recreating a hypervelocity impact on Whipple shields. The projectile and bumper layer are again represented by SPH particles, but the rear wall is comprised of finite elements, as it is not expected to deform as greatly, and because the erosion factor is used only with meshed bodies.

3.3.1 SPH Particle Size

A common rule of thumb when building an SPH body to be penetrated is that such body must have at least ten particles through its thickness [10]. The University of Manitoba team performed experiments on a shield design with a bumper thickness of 0.8 mm, and this is the data to which these numerical experiments are compared, giving a maximum SPH particle size of 0.08 mm. The ideal particle size was determined by simulating the bumper and projectile elements of the physical experiment, which caused the formation of an impact hole with diameter of 6.7 mm. In 2D a particle size of 0.03 mm was used initially, and decreased incrementally to 0.01mm, and each simulation was run for 3 μ s. In the 3D case, it was found that if the particle size was any smaller than 0.06 mm there would be too many elements for the program to process, and the model would not even run. This value is very close to the maximum particle size, and still gave satisfactory results and so was selected.

Too large an SPH particle size may lead to more than 5% of the total energy discrepancy in comparison with the initial energy, which is called an energy error. This indicates that too much energy is lost from the internal shock wave, because the particles are too large to model the discontinuity, or errors in the hydrocode have incorrectly added energy to the system. At a particle size of 0.02 mm the numerical experiments ran to completion in the least time, only one day, but with the greatest deviation of the simulated penetration diameter from the test data. With a 0.02 mm SPH particle size throughout, the hole in the bumper was only 6.1 mm in diameter, an 11% error when compared to the HVI tests performed by the University of Manitoba team. Decreasing the particle size to 0.015 mm reduced the error in the impact hole diameter to only 3%, and the experiment concluded after approximately 36 hours. Figure 3.6 shows the damage to the thin plate at the end of the simulation, with the diameter notation added after the experiment concluded.

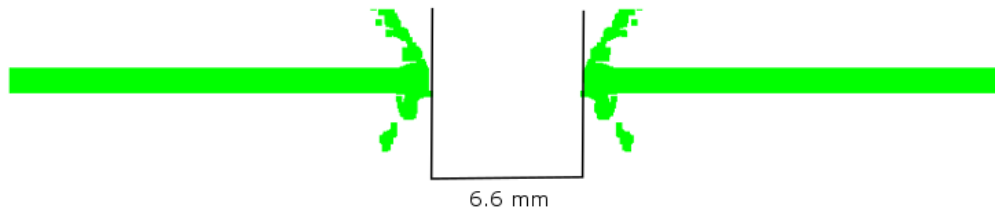


Figure 3.6: Impact hole with 0.015 mm particle size

Particle sizes lower than 0.015 mm caused numerical errors, which is when a large deformation moves SPH particles outside of the area of influence of the surrounding particles, where no break in the material would be expected based on physical experiments. This has the effect of creating an artificial weak point or crack where one would not exist, causing premature failure of the SPH body. This is called a numerical failure, as it is a problem with the numerical model itself, and has no equivalent in physical systems. In the case shown in Figure 3.7, the numerical failure became noticeable when several runaway particles accelerated well below the main body of the cloud. These particles are undesirable because they are moving much faster than the remaining cloud, having been ejected erroneously, and can cause damage to further bodies where it is not expected. These runaway particles do not behave as debris particles are expected too, often accelerating in a manner that is inconsistent with physical results. The particles can be deleted if detected, but the formation of these errors can be reduced by increasing the minimum density of the SPH particles.

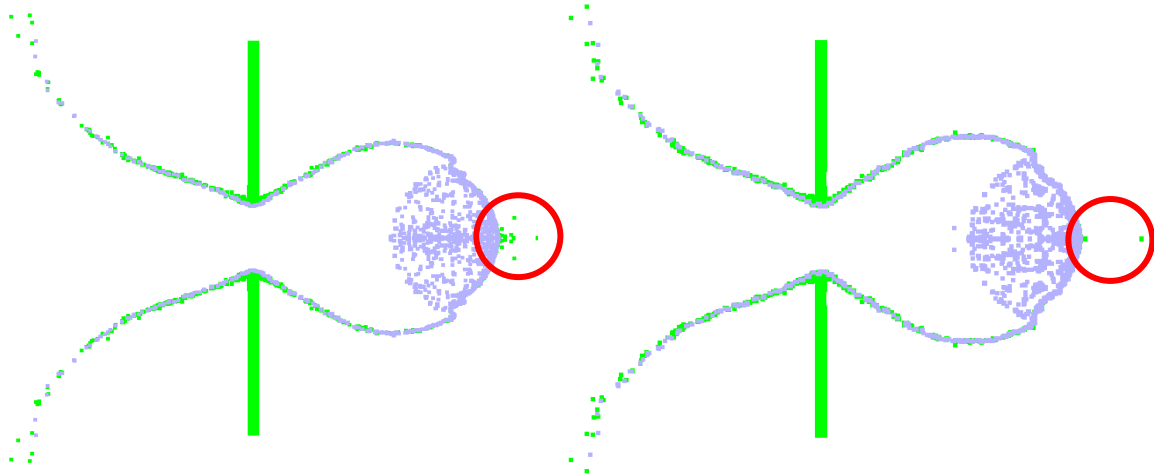


Figure 3.7: Comparison of 0.01 mm experiments with min density 0.5 (left), and 0.55 (right) with runaway particles indicated in the red circles

3.3.2 Erosion Factor

The erosion factor was determined by re-creating a series of impacts performed by NASA, in one of which perforation of the rear wall occurred, and it did not in the other. By comparing the simulations to the real data, the best erosion factor for this simulation was found employing the approach used in [10]. Three erosion factors were compared, 0.5, 1.0, and 1.5.

The NASA experiment A1076 experienced penetration of the rear wall in the test case; this result was obtained in numerical simulation for all three erosion factors. Simulating numerically NASA experiment A1077 where no rear wall perforation was expected, only the last erosion factor led to the “no perforation” outcome. Therefore, an erosion factor of 1.5 was selected to be used in the subsequent numerical experiments.

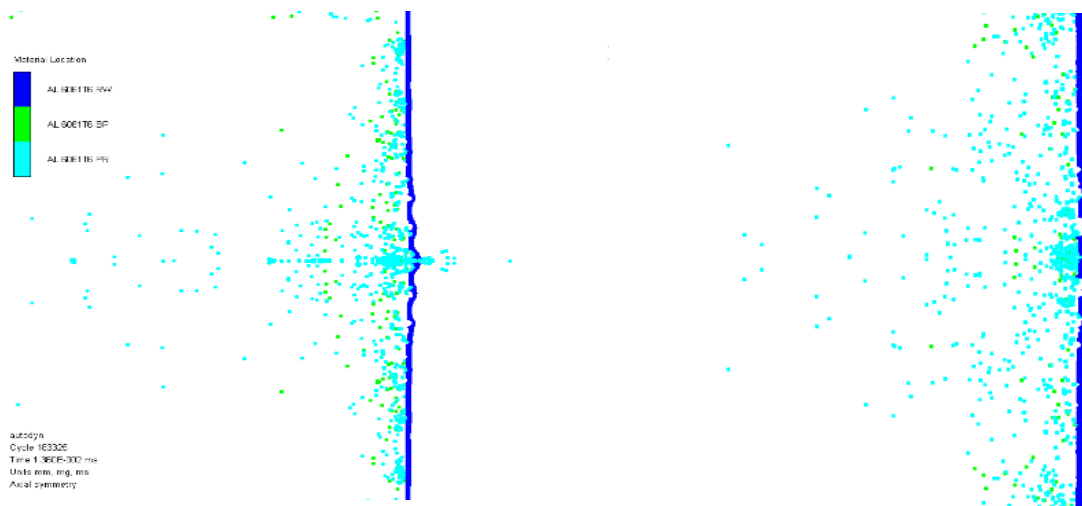


Figure 3.8: A1076 (left) and A1077 (right) numerical experiments with an erosion factor of 1.5, showing penetration as expected from NASA physical experiments.

3.3.3 Summary

The objective of this phase of research was to calibrate two computational parameters, SPH particle size and the erosion factor of the Lagrangean finite element model. It is necessary to calibrate these parameters before validating the material equations, as improper parameter selection will lead to non-physical results in later numerical experiments. The parameters chosen for impacts within this regime are;

- Erosion factor of 1.5.
- 2D SPH particle size of 0.015 mm.
- 3D SPH particle size of 0.06 mm.

3.4 EVALUATION OF MATERIAL EQUATIONS

This section details the process of evaluating six combinations of material models in the context of numerical HVI simulations, to determine the best set to move forward with when modelling multifunctional panels. All six of these numerical experiments are conducted on a model Whipple shield, built to reproduce the physical test conditions. The experimental setup consists of an aluminium 6061-T6 bumper and rear wall, being impacted by a 3.125 mm projectile travelling at 6.847 km/s, made of the same material. The bumper is 0.8 mm thick, and the rear wall is 1.7 mm thick. The thickness of the rear wall was determined to be sufficient to prevent penetration of the rear wall, per the BLE's. The projectile and bumper were simulated using SPH elements, due to the predicted large deformations they would experience. Initially the rear wall was also simulated using SPH particles, but it was found in earlier experiments that SPH bodies tend to over predict failure.

Three criteria by which the accuracy of the simulation will be gauged are: the diameter of the hole formed in the bumper, the shape of the debris cloud behind the bumper, and the rear wall damage. These criteria are arranged and described below in this order, as each criterion is affected by previous criteria. TABLE III shows the six experiments, with each of the six combinations of the listed material equations. Each experiment was run until 14 μ s had passed, unless the damage to the rear wall indicated that the rear wall was close to being penetrated. In that case the experiment was run for a longer period, to verify whether it would be penetrated or not. This end time was selected as in each experiment much of the debris had reflected from the rear wall by this time. As found in the previous section, an SPH particle size of 0.015 mm was used, and the rear wall is a Lagrangean finite element body with a geometric erosion factor of 1.5.

TABLE III: MATERIAL EQUATION COMBINATIONS

Combination	1	2	3	4	5	6
EOS	Mie-Gruneisen		Tillotson		Puff	
Strength	Johnson-Cook	Steinberg-Guinan	Johnson-Cook	Steinberg-Guinan	Johnson-Cook	Steinberg-Guinan
Failure	Johnson-Cook Failure					

3.4.1 Impact Hole Size

The first criterion used for evaluation of the material model combinations was the size of the impact hole formed in the bumper. A physical experiment performed by the University of Manitoba team on the identical Whipple shield gave a penetration diameter of 6.7 mm, as shown in Figure 3.9 [10]. The accuracy of impact hole diameter calculation is very important since it affects the two other criteria, due to the addition of mass from the bumper to the debris cloud and

ejecta. As such a percent difference of 5% was selected as the point beyond which a material combination will be deemed unacceptable.

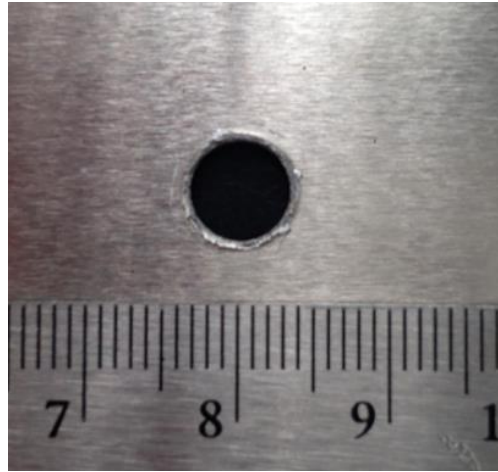


Figure 3.9: Image of bumper from physical test [44]

Combination one, shown in Figure 3.10, performed the best in both two and three dimensions, the impact hole diameter had a 0% error in two dimensions, and only 2.9% in three dimensions. The discrepancy between the two-dimensional results and those from the SPH particle size experiments is due to the longer simulation time.

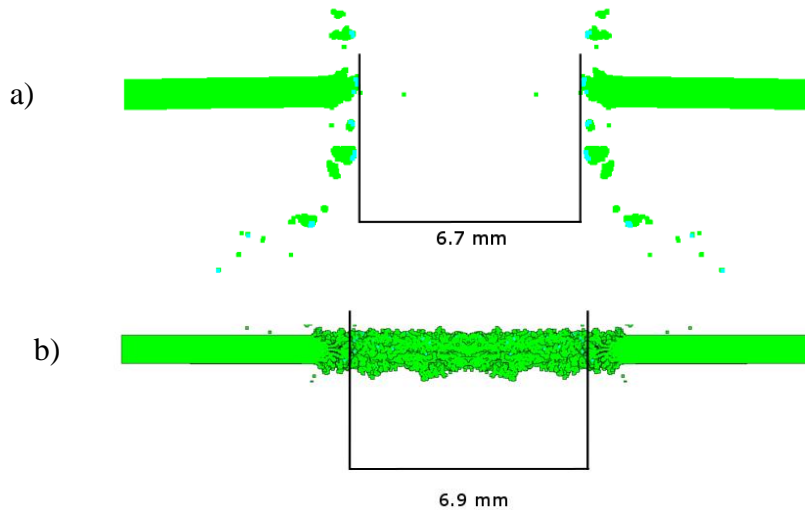


Figure 3.10: 2D (a) and 3D (b) impact hole diameter results using combination 1, Mie-Gruneisen EOS, and Johnson-Cook strength model

Combination 4 had the least accurate impact hole diameter in two dimensions, with a percent error of 55%. The debris from the impact also had a more fluid appearance than the debris in

other numerical experiments. Figure 3.11 shows how the debris forms four solid tendrils of material radiating from the impact site, which is not how the material is expected to behave based on physical test data. Combinations 2, 3, and 5 also had a percent difference greater than 5% when compared to the physical test, only trials 1 and 6 had an acceptable percent difference when compared to the physical experiment in two dimensions.

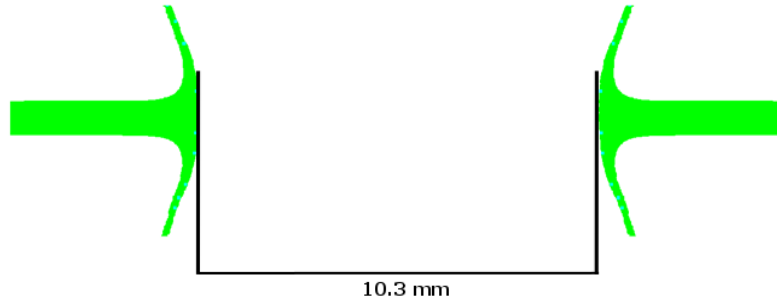


Figure 3.11: 2D impact hole diameter using combination 4, Tillotson EOS and Steinberg-Guinan strength model.

The results are expected to be different in the three dimensional as fewer simplifications must be made to the model compared to two dimensions, and this should have a positive effect on the experiments accuracy. However, due to constraints from the program itself the particle size had to be increased from 0.015 mm to 0.06 mm, which will decrease the accuracy of the experiment. A larger number of impact hole diameters fall within the specified 5% difference in the 3D trials. Trial 6, shown in Figure 3.12, is the notable exception, it is the only trial that moved from an acceptable percent difference to one that is unacceptable, although the diameter of the hole in trial 1 did increase. Of the trials that showed a decrease in percent difference, trial 4 made the most noticeable improvement, with a percent error in three dimensions of only 4.4%.

Compared to the 2D trials, the holes in the 3D trials tend to be larger than 6.7 mm in diameter, not smaller, which could be a result of the increased particle size.

Overall the combination of material models used in experiment 1, J-C strength and the Mie-Gruneisen EOS, performed the best in both two and three dimensions when being evaluated using this criterion.

3.4.2 Debris Cloud Shape

This stage of the material model evaluation process focused on the debris cloud shape. This is a critical factor in determining the validity of a material model, as the cloud shape is the best indicator of the amount of debris, and its velocity after the impact between projectile and

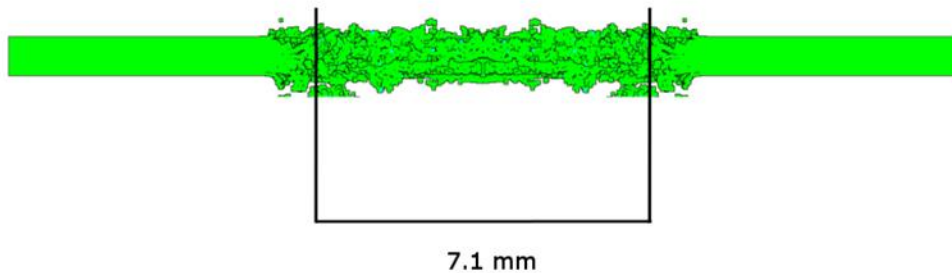


Figure 3.12: 3D impact hole diameter using combination 4, Puff EOS and Steinberg-Guinan strength model.

bumper. The debris cloud on the side of the bumper plate impacted by the projectile will be referred to as the ejecta, and the cloud between the bumper and rear wall will be referred to as the debris cloud, terminology commonly used in the designing of MMOD protection [6]. This reflects the configuration of a Whipple shield used in a physical structure. The shape of the debris cloud will show us if there are any numerical errors in the SPH portion of the experiment.

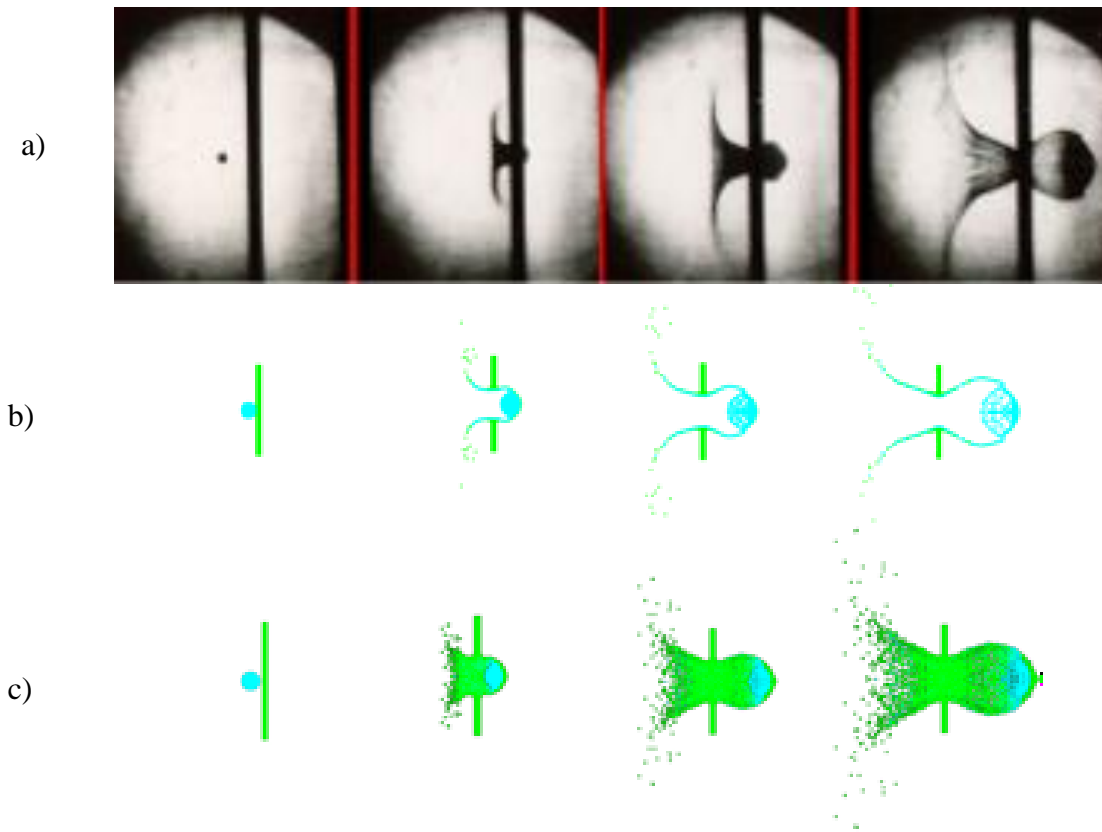


Figure 3.13: Debris cloud shapes from NASA physical experiments (a), and 2D (b) and 3D (c) numerical experiments using material combination 1 at 0,1,2, and 3 μ s

Because particles expelled during numerical errors can have a higher energy than would be expected, they are more likely damage or penetrate the rear wall. Besides numerical errors, we are also comparing the numerical data to that from a NASA test to ensure that the general shape is consistent with physical tests [16]. Figure 3.13 shows the two and three-dimensional experiments using combination 1, contrasting them to the debris cloud formed by an identical impact during a NASA test.

3.4.2.1 Time = 1 μ s

At 1 μ s both the 2D and 3D debris clouds are still relatively small, and many features that will become clear later are not yet visible. The projectile has fragmented and is starting to

expand within the debris cloud. In the physical experiment, the distal part of the cloud is flat, curving away only at the ends. However, this behaviour is only evident in numerical experiments for combinations 1, 3, and 6. In the remainder the exterior cloud gently curves along the whole length instead.

3.4.2.2 *Time = 2 μ s*

At 2 μ s the clouds have expanded, making observation much easier. In the two-dimensional experiments, the flattening of the debris cloud in a ring around the clouds midsection is much more noticeable in numerical experiments for combinations 1 and 5 than for the others. Numerical experiment for combination 3 has some particles in the debris cloud that look out of place, which could possibly be due to a numerical error. The ejecta cloud remains mostly flat in the physical experiment, and even the curving away at the ends seems to have dissipated. Numerical experiment for combination 1 is the only one where the distal edge of the ejecta cloud remains relatively flat, experiments 3 and 6 have begun to disperse and curve away. In fact, only combinations 1 and 2 give the thin cloud of ejecta expected from looking at the physical tests, all the rest have a large degree of dispersal.

Due to occlusion from particles behind the 2D viewing plane, features are much harder to distinguish in the 3D trials. In none of them the plateau around the debris cloud can be seen, and in all cases the ejecta cloud is very thick. The lack of the plateau likely relates to the increased particle size, as there are not enough details to distinguish such a small feature.

3.4.2.3 *Time = 3 μ s*

At 3 μ s the differences between the numerical experiments is much more noticeable. Numerical experiments for combinations 1, 2, and 4 have better debris cloud shapes, as the

debris is tightly packed at the leading edge of the cloud. As for the ejecta cloud, debris has begun to disperse even for combination 1, leaving only simulation for combinations 2 with the expected thin cloud at the distal edge.

The six 3D trials are now more easily distinguished from one another, however there is still no noticeable plateau in any of them, and the ejecta is even further expanded compared to the images at 2 μ s, although all six are slightly pointed at the leading end of the cloud. Numerical results for combinations 1 and 6 also have an odd spread in the debris left from the projectile, while for others it forms an oval at the leading edge.

Overall, in two dimensions the simulation for combination 1 was found to be the most consistent with NASA physical experiments, although none of the experiments demonstrated an extreme deviation from predicted behaviour. In three dimensions, the increased particle size and count obscured many details used to evaluate the debris cloud shape, but still no experiments produced results far outside what was expected.

3.4.3 Impact response of Rear Wall

The damage of the rear wall is the easiest criterion to quantify. The BLE's for this shield indicate that the rear wall would not be perforated, so any numerical experiments that do not reflect this are unacceptable. Beyond this simple metric, the damage patterns from each numerical experiment were compared, to see if any appeared to deviate visually from the others, or what is expected from physical experiments.

Figure 3.14 shows the rear wall from the two-dimensional numerical experiments at simulation end, and we can see clearly that both simulations for combinations 3 and 6 showed penetrations and are therefore not acceptable. What is also interesting is how the different numerical models produce very different looking damage patterns on the rear wall. Like the image of the impact hole, numerical simulation based on the combination 4 produced damage that appears very smooth and has deeper craters than any other non-perforated trial. Except for that result we can also observe that the deepest craters are formed in the centre of the plate, and that this is where the rear wall was perforated for the combinations 3 and 6. This is in line with expectations, as that is the area with the highest concentration of debris.

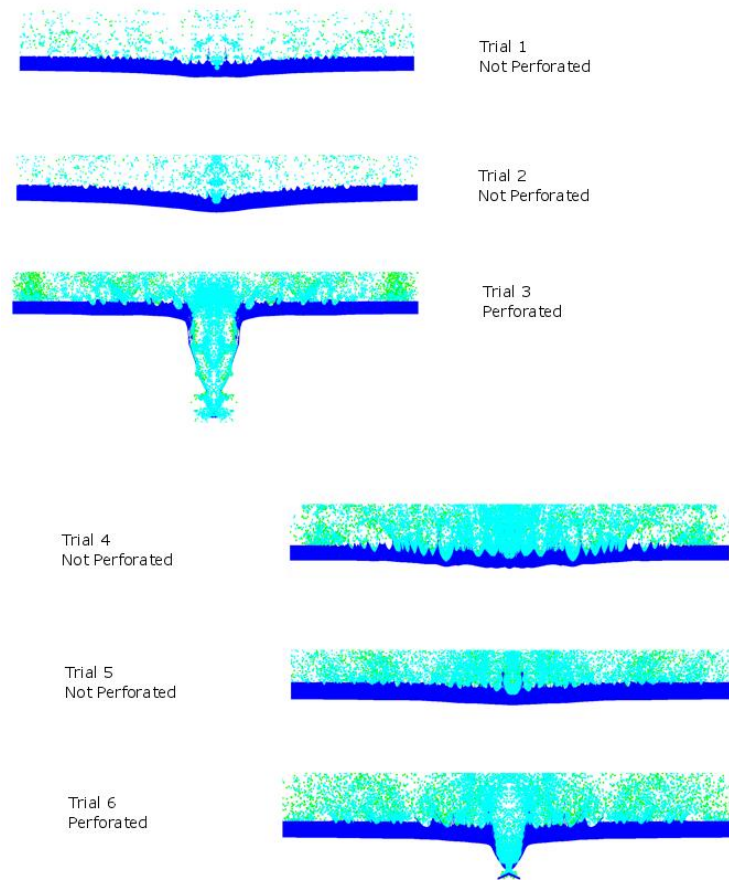


Figure 3.14: Rear wall centre at simulation end in two dimensions

In three dimensions, it is harder to see the exact damage patterns in the rear wall, but there are some noticeable differences between the images in Figure 3.15 and the two-dimensional images from Figure 3.14. First, none of the six experiments were perforated, a step up in accuracy from the 2D experiments. Also, the rear wall is noticeably deflected in the centre, forming a crater. The penetration of the rear wall is deepest in the very centre of all six trials, as is expected. Experiment 6 experienced an error in the very centre of the rear wall, where a large spike can be observed, which indicates that the Lagrange rear wall is very close to being penetrated.

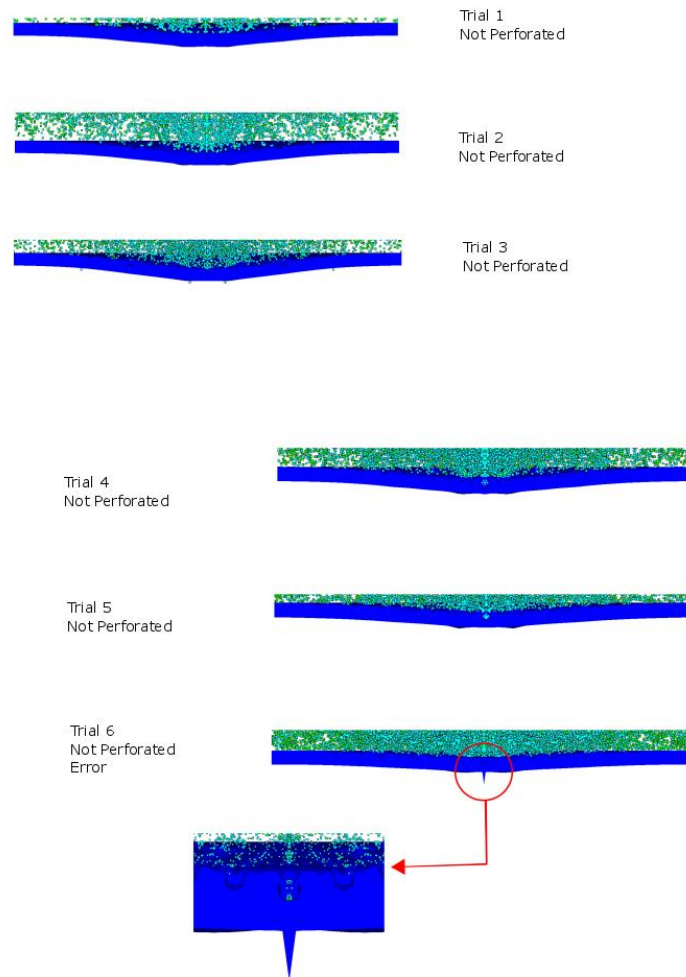


Figure 3.15: Rear wall centre at simulation end in three dimensions

Overall, in both two and three dimensions, most material model combinations seemed to adequately predict the response of the rear wall. Numerical experiments for combinations 3 and 5 demonstrate the least conformity with expected damage patterns making these combinations to be least acceptable by this criterion.

3.4.4 Summary

The evaluation and selection of the material models which will result in numerical results in greatest agreement with physical HVI testing was performed using numerical experiments. The same impact event was simulated with six different combinations of material models, and the resulting penetration diameter, debris cloud shape, and rear wall behaviour were compared to the other numerical experiments and to NASA and University of Manitoba physical experiments. It was found that, overall, the combination 1 provided the best results the numerical experiment. The other experiments may yield results that are as good or better for impact simulations in velocity regimes where temperature and melting effects will have a greater affect upon the behaviour of the shield, and so this phase should be repeated if investigating higher velocity impacts.

3.5 CONCLUSIONS

Based on these preliminary experiments the best computational and material parameters for this impact regime have been found. When simulating impacts between 4 and 7 km/s using aluminium, the values presented in this section will provide the best results, and are what will be used in all following sections of this thesis. If using a different set of materials, or a vastly different impact speed it would be suggested to repeat these experiments using those new values. This methodology can also be adjusted for advances in material characterization, new material

models can simply be added to the above combinations and tested in a similar manner. The final parameter selected for the geometry selection phases is as follows;

- Erosion factor of 1.5.
- 2D SPH particle size of 0.015 mm.
- 3D SPH particle size of 0.06 mm.
- Mie-Gruneisen EOS.
- Johnson-Cook Strength and Failure models.

4 MODELLING OF HVI ON CONVENTIONAL HONEYCOMB PANELS

Honeycomb panels are a lightweight load bearing structure, consisting of a hexagonal core between two face-sheets. The sandwich structure increases the bending strength and loading capacity of the panel compared to the face sheets alone, while having minimal effect on the mass of the structure. Honeycomb panels have an inherent impact protection capability; their front and rear face-sheets act on the MMOD particle as the bumper and rear wall of a Whipple shield. However, the hexagonal cells that give the panel its stiffness also limit the spread of the fragments (i.e. debris cloud) over the rear wall lowering the protection effectiveness of the panel compared to other designs of a similar weight [27].

In this section 2D and 3D numerical HVI tests on aluminium honeycomb panel will be performed and compared with the available physical experimental data, e.g. NASA test HITF04150 [11] shown in Figure 4.1 below. These simulations will be used for evaluation of

effectiveness of the conventional panel in comparison with metal foam sandwich panels, which will be discussed in Section 5.

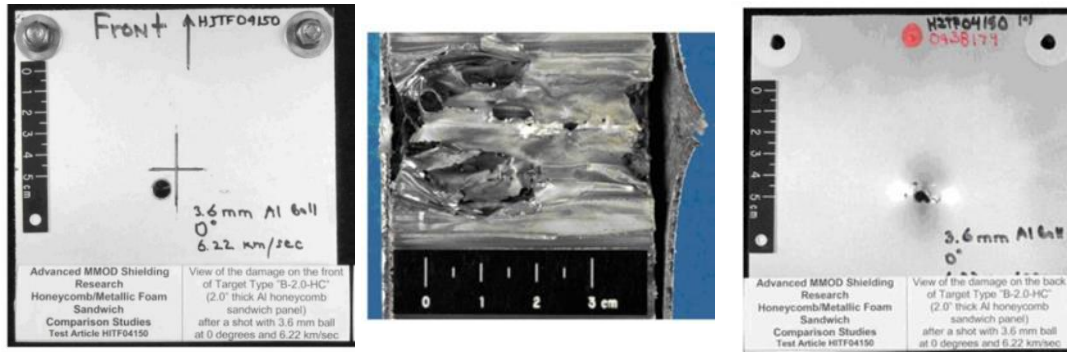


Figure 4.1: NASA experiment HITF04150 showing damage to front panel (left), honeycomb core (centre) and rear panel (right) [10] – NASA.

This experiment investigates the effect of a 3.6 mm particle travelling at 6.22 km/s, which impacts the shield at a right angle. The shielding panel consists of a two-inch honeycomb core, with 1.27 mm aluminium face sheets attached to the top and bottom as illustrated in Figure 4.2. This geometry can be reproduced in 3D, but simplifications to the geometry must be made when re-creating the physical experiment in 2D, as discussed in detail below.

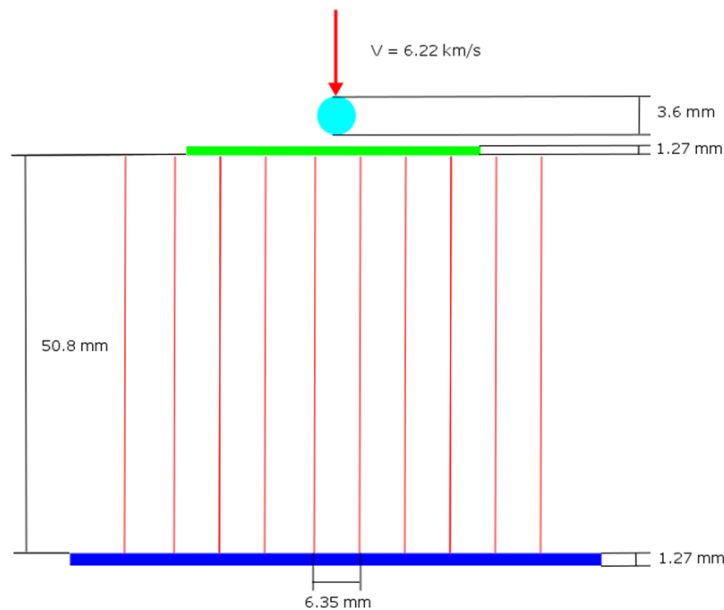


Figure 4.2: Geometry of two-dimensional honeycomb panel

4.1 2D HONEYCOMB PANEL SIMULATION

Representing a honeycomb panel structure in two dimensions is more challenging than just a simple Whipple shield. When taking a cross-section of the honeycomb core to reduce it from three to two dimensions, the hexagonal structure causes several different patterns between the face-sheets depending on the direction of the cross section, as seen in Figure 4.3. This is a major concern in two-dimensional analysis, as the simulation creates symmetry by rotating the 2D

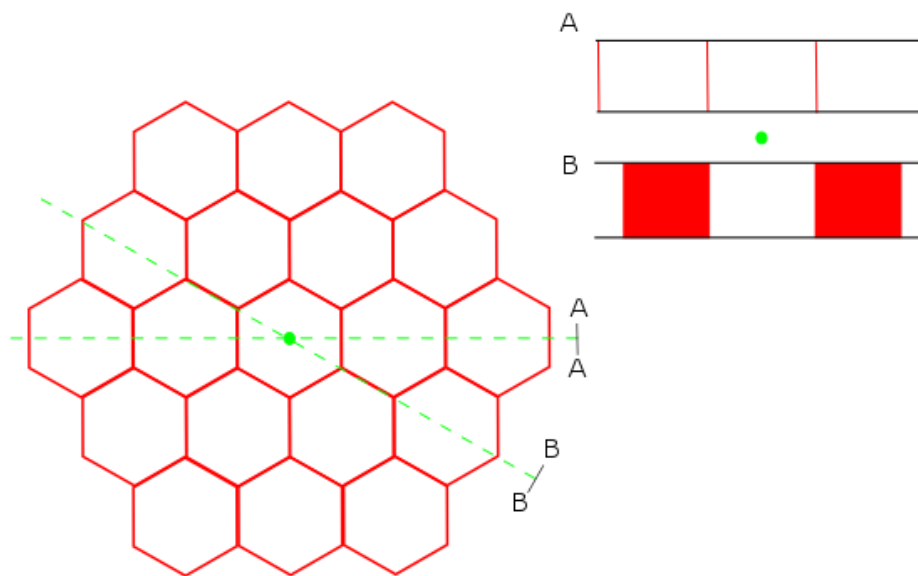


Figure 4.3: Honeycomb cells with two cross sections

object about its central axis, so what appears to be a rectangle in two dimensions is considered in fact either a solid or hollow cylinder in three dimensions, depending on the original rectangles position with respect to the axis of revolution. Since the hexagon cells have incredibly thin walls compared to the rest of the geometry, the walls are often treated as being two dimensional, and we can therefore simplify the structure with minimal effects on the accuracy of the experiment.

E.g., for the projectile position indicated by green point in Figure 4.3, all the honeycomb walls radial to the centre of that impact will have minimal effect on the debris cloud propagation. This means the honeycomb structure can be simplified by removing these walls, leaving a set of concentric rings made of the remaining walls. Since the hexagons are all the same size, these hexagonal rings can be further simplified to a set of concentric circular rings around the point of impact, like the example in Figure 4.4. This approach was initially introduced by A. Cherniaev [45] and implemented in the present analysis.

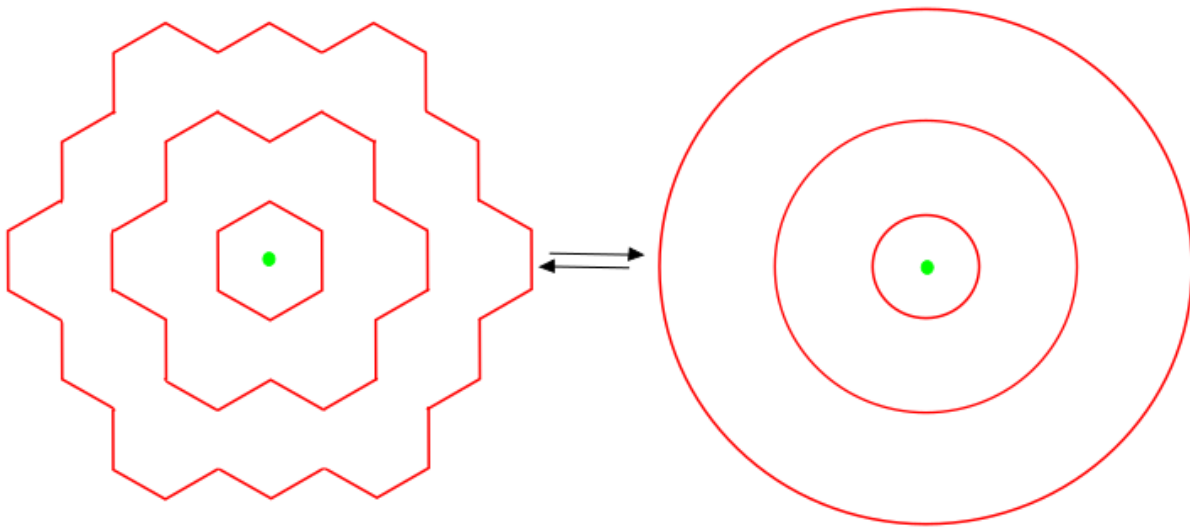


Figure 4.4: Simplified honeycomb cells

This approach means that the 2D cross-section is now the same in all directions, and this approach seems to have good agreement between the 2D and 3D experiments. One possible exception is the channelling of the debris inside the corners of the hexagonal cells, which cannot be modelled directly, this is discussed in more detail in a later section.

4.1.1 Simulation Setup

The two-dimensional numerical experiment was set up as shown in Figure 4.2, using the SPH method for the front bumper and projectile, and FEM for the honeycomb walls and rear wall, using the computational parameters found in chapter 3. From the preliminary numerical experiments, it was found that some SPH particles would experience a non-physical increase in velocity, reaching speeds much higher than the initial impact velocity causing excessive damage and shortening the simulation time step. Deleting these particles before they impacted the rear wall showed no negative effects on the accuracy of the simulation, and is the recommended method for rectifying this issue if it reoccurs. This experiment involves penetration of multiple bodies, and with each penetration some energy error is introduced by necessity by the program itself. Therefore, the energy error criterion is not well suited for tracking the performance of the experiment, as excess energy is unavoidable in this sort of experiment. However, if it is being used the reference cycle must be reset after each particle deletion, to reflect the new total energy.

4.1.2 Simulation Results

As it can be seen from Figure 4.5 the rear wall in the physical experiment is perforated and the damaged honeycomb has a greater diameter close to the point of impact. Not all details present in this image can be seen in a two-dimensional simulation, but we should expect the overall damage pattern from the numerical experiments to be as close as possible to the physical case.

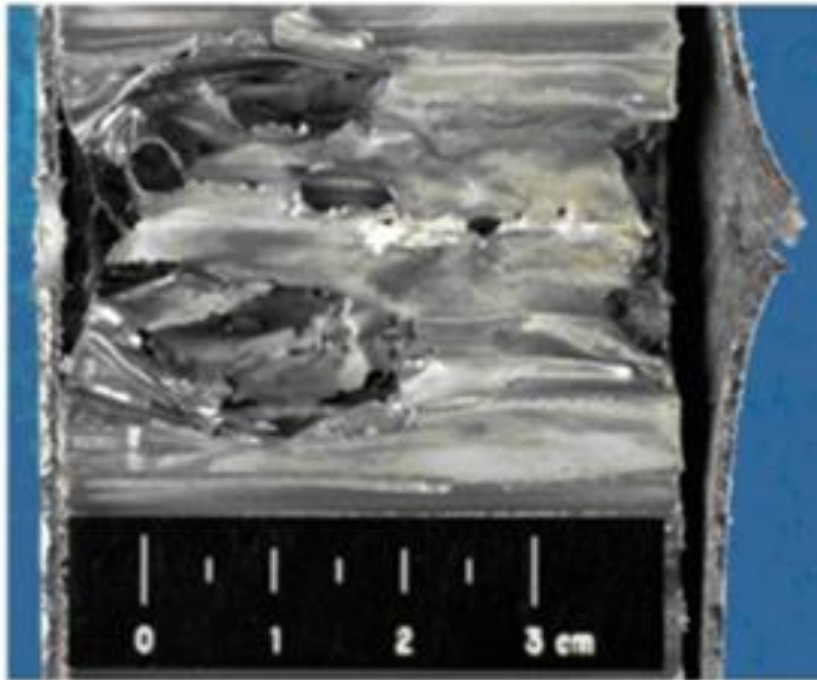


Figure 4.5: Close view of damage to honeycomb core [9] – NASA

In the physical experiment, NASA observed perforation of the rear wall. From the shape of the damaged area of the honeycomb core it can be inferred that the debris from the projectile and bumper was channelled by the honeycomb cells, concentrating the bulk of the debris into the few cells directly below the point of impact. This effect negates the advantage provided by the standoff between the plates, and there is no BLE that can account for both the standoff between the plates and the existence of the honeycomb core, existing equations such as those for the Whipple shield must be used and the parameters within those equations must be changed per physical HVI experiment data [2]. From Figure 4.5 we can also obtain some information about the damage to the honeycomb core itself, which can be used to compare the numerical and physical experiments. We can see that at its widest, the damage to the honeycomb core is 1.2 inches across, and the diameter of the hole in the bumper layer is 0.3 inches.

In the numerical experiment, perforation can be seen at the rear wall and the channelling of the debris could be observed as it occurred. The channelling of the debris can be clearly seen in Figure 4.6, where the front portion of the debris cloud is entirely contained within the central honeycomb cell. Figure 4.6 also shows that the debris is channelled inside honeycomb cells away from the axis of symmetry, this implies limited damage to the honeycomb cell walls as we move further from the point of impact, which is consistent with the NASA experiments. Further, the approximate maximum diameter of the damaged portion of the foam core is 1.23 inches, and the diameter of the hole in the bumper is 0.3 inches, both measured at the time the simulation ended. These results are consistent with data from the NASA experiments, and show that the simulations produce internal damage consistent with physical experiments.

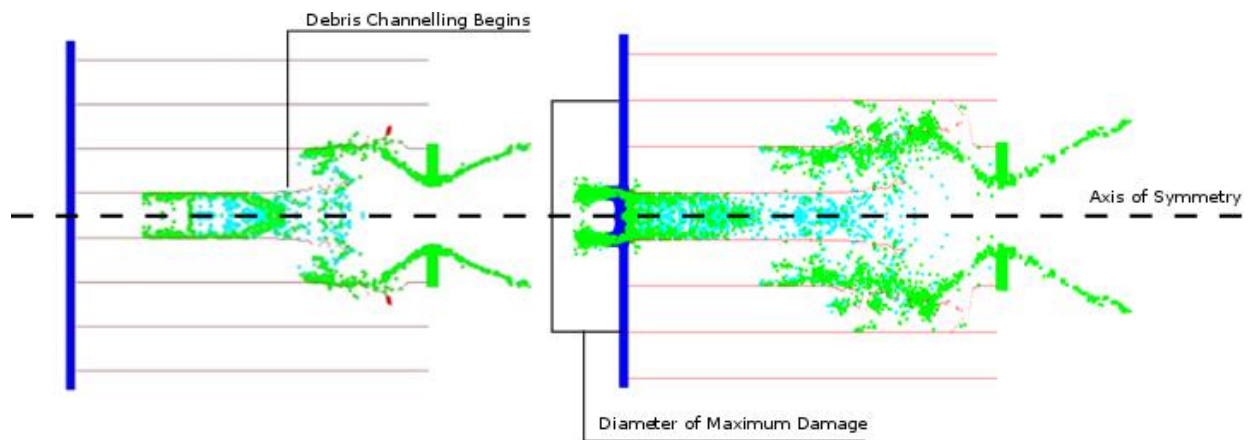


Figure 4.6: 2D Debris channelling

As can be seen in Figure 4.6 the numerical experiment did show penetration of the rear wall as in the physical experiment. However, the way the debris was channelled by the honeycomb cells means that the simulated rear wall was penetrated in a ring, forming a plug of rear wall material. Given the large mass of debris still moving towards the rear wall at the time the simulation was ended it is probable that this plug would be broken up further. Debris can also be seen reflecting from the rear wall back into the next cell radial from the centre in Figure 4.6. This indicates that

the rear wall is bending away at the point of impact, as in Figure 4.5. Once again, the numerical experiment ended before the point where we see the results from the physical experiment, but the overall simulated behaviour matches the NASA test results.

4.2 3D HONEYCOMB PANEL SIMULATION

Simulating the honeycomb in 3D does not require the same level of simplification as the 2D experiments, but each simulation took 2-3 times as long to complete, compared to the 2D experiments. One quarter of the cylindrical geometry was created within ANSYS, and reflected about the x and z axes to give the complete model. This reduces the complexity of the model and reduces computation time, but does mean that we see a regularity to the damage that does not exist.

4.2.1 Simulation Setup

Once again, the simulation was set up per NASA experiment HITF04150 [11], and the computational parameters were set as described in section 3. The honeycomb structure was set to not interact with itself because it was found that during these experiments the program would freeze and then crash when one piece of debris from the honeycomb would impact another, likely caused by an internal error within the hydrocode. Since the honeycomb walls are so thin, the amount of debris it produces is negligible, and removing it had no noticeable effect beyond visible pieces of honeycomb debris outside the original simulated body. It was also found that using FE when modelling the rear wall provided poor results, producing large deformed mesh elements at the point of penetration, as seen in Figure 4.7. Using an SPH for the rear wall eliminated this effect and produced a better damage pattern at the penetration point.

4.2.2 Simulation Results

Once the rear wall was reconstructed using SPH particles instead of FE|M, the 3D honeycomb provided results consistent with both NASA data and the 2D experiments performed earlier.

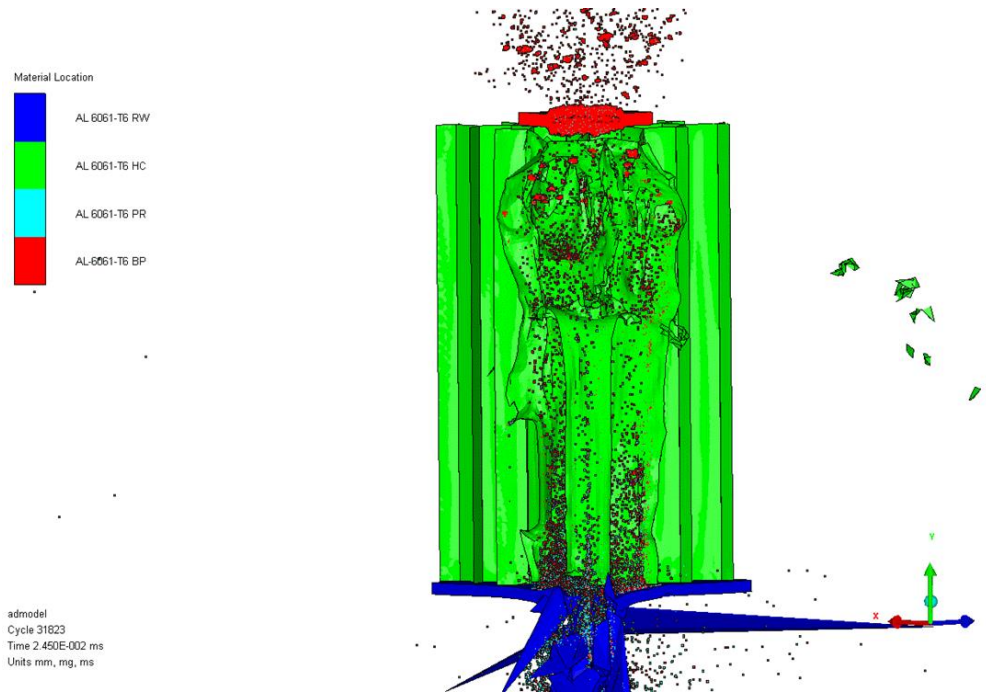


Figure 4.7: Damage at simulation end using FE for rear wall.

Once again, the debris was concentrated in the central cells close to the rear wall of the panel, as was seen from the damage patterns present in the NASA results. Figure 4.8 shows a quarter element of the simulated configuration at the time the numerical experiment was stopped. The debris in the cells not directly below the point of impact are lower energy than the debris in the central channel, it is likely that this debris is responsible for most of the bending of the rear wall that was seen in Figure 4.5, as this debris may not have enough energy to penetrate the rear wall.

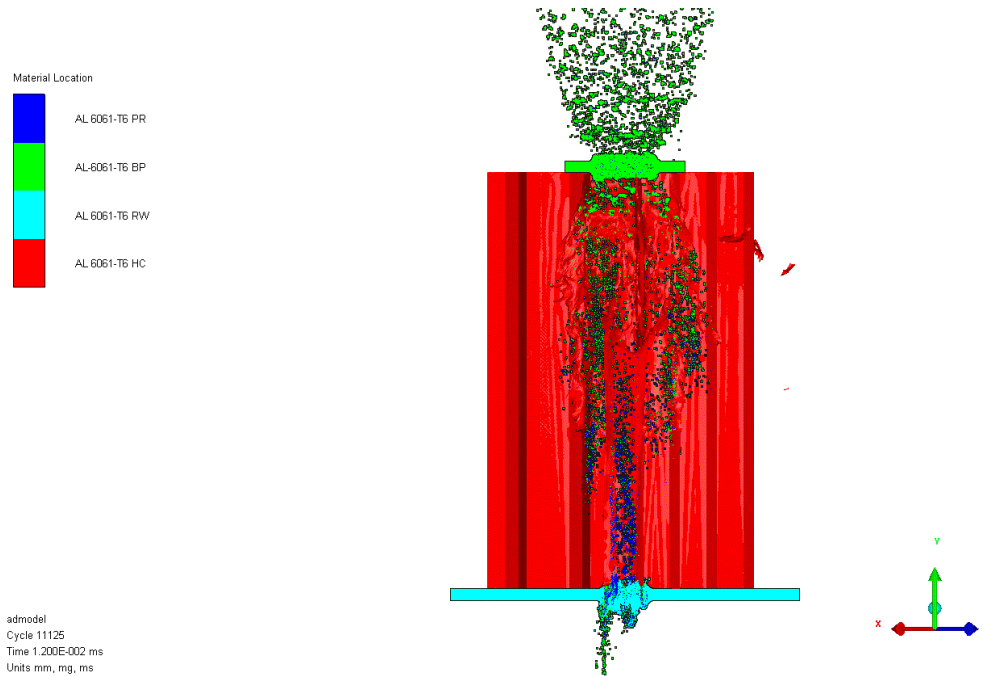


Figure 4.8: Damage at simulation end using an SPH body for rear wall.

4.2.2.1 Rear Wall Failure

As with the two-dimensional experiments, the simulation was stopped before the point where we could see the damage in the physical tests, giving us an idea of how the damage evolved during the impact. In Figure 4.8 several distinct clouds of debris can be seen on the far surface. These clouds correspond to the locations of the corners of the central hexagonal cell, implying that there is a secondary concentration effect occurring within each honeycomb cell. This effect is discussed in greater detail below.

4.3 COMPARISON OF 2D AND 3D SIMULATIONS

Both 2D and 3D models required some level of fine-tuning to prevent any errors that occurred in the initial setup, but in the end both produced satisfactory results, consistent with NASA experiment HITF04150 [11]. However, the three-dimensional case produced results after a calculation period of on average 1.5 weeks, whereas the two-dimensional experiments ran to

completion in an average of only three days. If a detailed picture of the damage to the honeycomb core is required, the 3D method is far superior, however the 2D experiment provides accurate results much faster, if the trade-off of losing detail is worth the fast acquisition of rear wall perforation data.

A discrepancy between two-dimensional and three-dimensional numerical experiments is the simplification of the concentration of debris in the corners of the honeycomb cells themselves. Figure 4.9 shows a close-up of the rear wall, with the honeycomb cells removed, shortly after perforation of the rear wall. We can clearly see that in the corners of the hexagon, there is a larger concentration of debris. These are the sites where penetration of the rear wall first occurs, which is consistent with results obtained by other members of the University of Manitoba team [10].

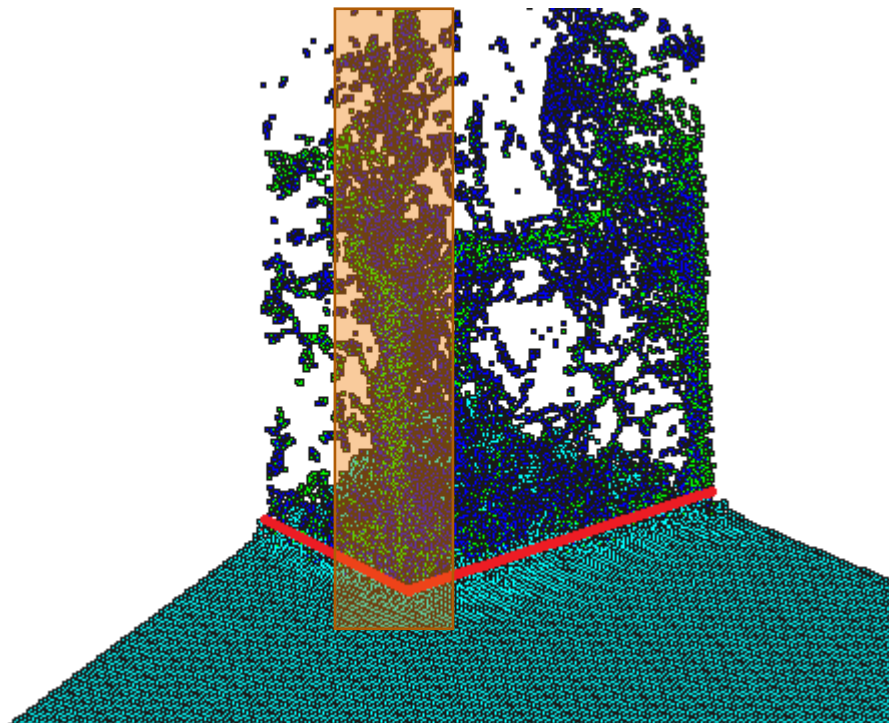


Figure 4.9: Concentration of debris in 3D honeycomb, corner concentration highlighted

This effect is not reproduced in 2D. As Figure 4.10 shows, the debris is concentrated along the entire outer wall of the honeycomb cell. This will lead to penetration of the rear wall in a ring, as opposed to discrete points. This may be an important factor to consider when the pattern of debris beyond the rear wall is important, for example in parts of a satellite where critical components are located. The inaccurate debris concentration could also be a factor during testing closer to the ballistic limit of the shield, as the larger hole penetrated through the rear wall in the 2D simulations could indicate that this setup is conservative with regards to predicting penetration. Further study should be done to determine the precise nature of the discrepancy in this area.

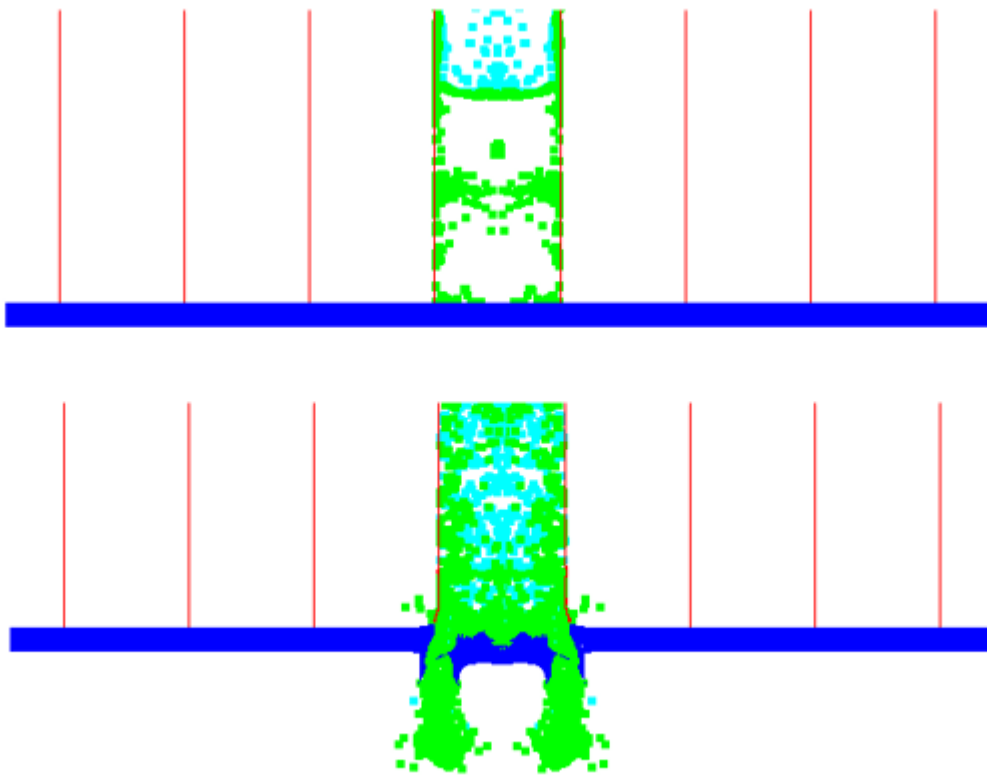


Figure 4.10: Concentration of debris in 2D honeycomb

5 MODELLING OF HVI ON STRUCTURAL FOAM CORE

PANELS

Performing three-dimensional numerical experiments on foam panels is a reliable way of assessing penetration depth of MMOD particles, however each simulation can take weeks [10]. This type of simulation is very valuable when assessing the performance of a specific shield, but when testing multiple configurations, the time to complete each experiment is just too long. Since it is not economically viable to perform physical experiments, a less expensive numerical alternative is necessary. This chapter will discuss relevant background information regarding metallic foams, and challenges with the simulation process, as well as two methods of obtaining initial design specifications for a structural foam core panel. The first method employs the BLE's obtained for a Whipple shield to evaluate the performance of foam core panel of equal mass. This method allows for the rough determination of the standoff required to protect against a given particle and impact velocity. The second method is a two-dimensional numerical experimental setup that gives information on the penetration depth of a given impact, faster but less accurately than a three-dimensional experiment. These two methods are envisioned to be used alongside three-dimensional and physical HVI testing to provide the desired balance between computational speed and accuracy while designing effective foam core shielding panels. Figure 5.1 shows how the various methods presented throughout this thesis are recommended to be used in concert. First, the constraints upon the shield should be determined. Information about what projectiles the shielding will need to be able to withstand for a given chance of mission failure can be found using a statistical analysis program such as NASA's ORDEM [46], or otherwise specified. The thickness of the shielding panel is determined by the designers, if the

panel is too thick the satellite may be too heavy, if it is too small the panel may not provide enough structural support for the satellites components (in the case of multifunctional panels only). The initial calculations can then be performed to get a rough estimate of how thick the foam panel must be to withstand an impact with the projectile specified in step 1. This estimate is refined using 2D simulations, with a quick turnaround, to find the lightest panel capable of protecting against MMOD impacts. The final step is to verify the results of step 3 using either 3D simulations or physical HVI experiments, depending on whether time or money is the greatest limiting factor in the project. Compared to using only 3D simulations or physical experiments, this method is faster and less expensive.

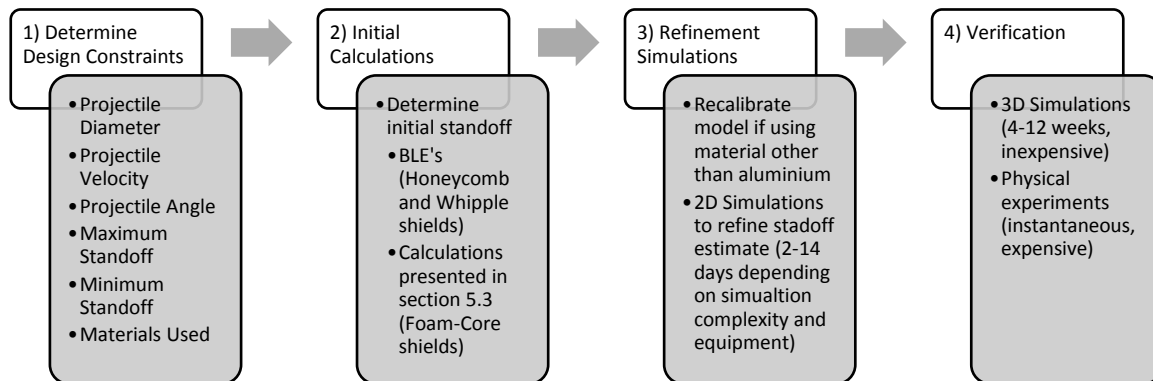


Figure 5.1: Recommended shielding design workflow

The bulk of this chapter discusses the third stage shown in Figure 5.1, as while there is currently a method for simulating foam panels in three dimensions, no such model exists in two dimensions [10]. We can still use the same material equations determined in section 3.4 to model the material within the foam panel. However, simulations must be performed to find a method of reducing a three-dimensional foam to two dimensions, in a manner that still represents the foams three-dimensional behaviour. In these simulations, the most important factor in determining if the

simulation was successful was whether the rear wall was penetrated, but the penetration depth and impact hole diameter are also of interest. A NASA HVI test HITF04151 [11], was selected as the basis for the models, and will be discussed in more depth in the next section. The NASA experiment was re-created within ANSYS with different two-dimensional geometries designed to represent the specific foam used in the NASA experiment.

5.1 COMPARISON DATA

NASA has compiled HVI test data for several foam and honeycomb core experiments, which will be used as the comparison data for the mathematical model and numerical experiments in this chapter [11]. The initial set of numerical experiments conducted to find the method of reducing the foam geometry to two dimensions were based off NASA experiment HITF04151 [11]. After the HVI test was conducted, NASA cut the sample in two, shown in Figure 5.2. From this figure, we can see that the debris penetrated 1.63 inches into the foam, and the impact hole diameter is 0.38 inches.

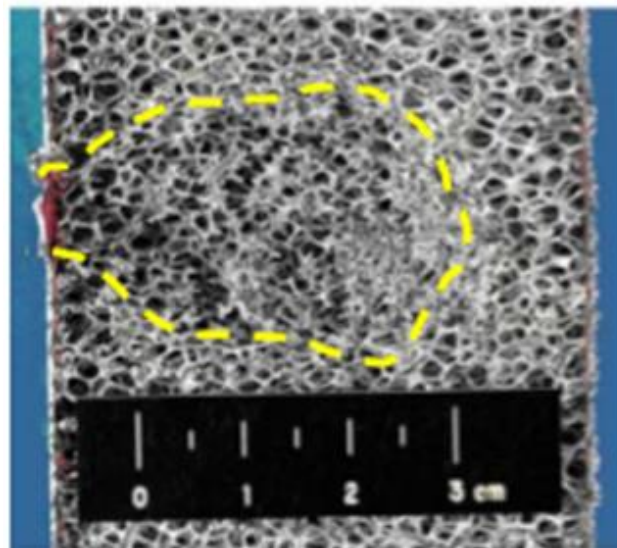


Figure 5.2: Damage to interior of foam core during experiment HITF04151 – adapted from [27] – NASA

The experiment setup of HITF04151 [11] consisted of a two-inch thick foam core, with ten pores per inch (PPI) and between 6-8% relative density compared to solid aluminium [11]. Both the PPI and relative density alter the structure of the foam, and are very easy to visualize in this model, like in Figure 5.3. In Figure 5.3 we can see that the foams with a higher PPI value have smaller cells, and foams with a higher density have thicker ligaments. By altering these two properties, it is possible to tailor both the weight and impact resistance of a foam panel to a high degree. For example, a high density, high PPI foam will be much stronger but also be much heavier than a low density, low PPI foam. However, the low density, low PPI foam has weaker cells that are more likely to be less effective upon impact with projectiles of a similar scale to the foam cells, like the kind simulated below.

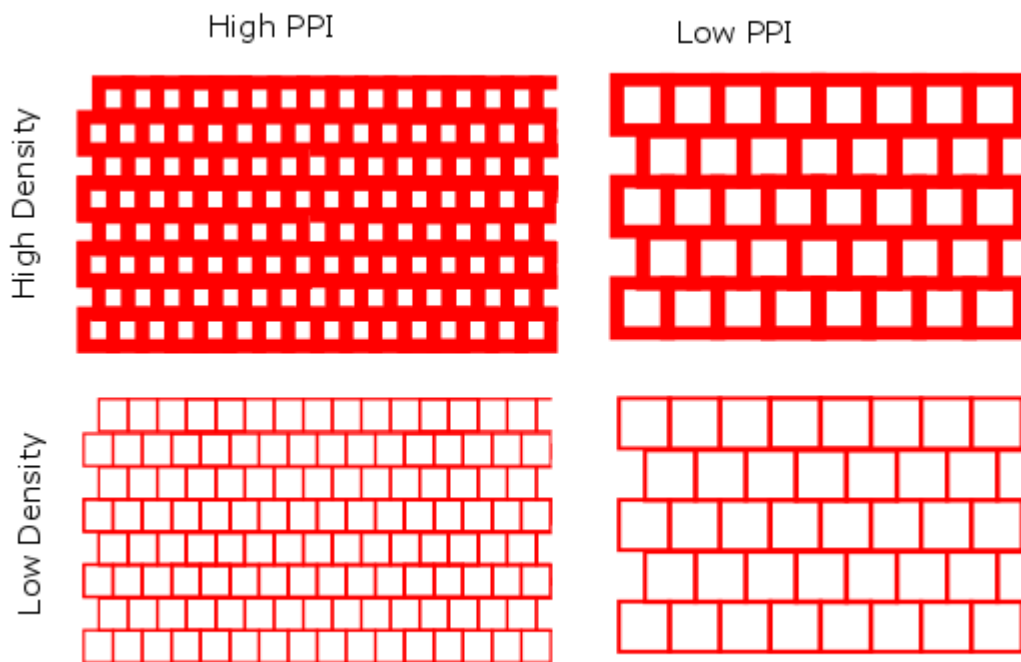


Figure 5.3: Effect of PPI and density on metal foams of equal area

The rear and front facesheets used to build the foam panel for experiment HITF04151 [11] are both 0.01 inches thick, bonded to the core with adhesive. The projectile was 3.6 mm in diameter, impacting normal to the surface of the panel at 6.76 km/s. The facesheets and projectile

used in this NASA experiment are reproduced in two dimensions in the same manner as used to create the Whipple shield panels in chapter 3. The following series of experiments trialled various methods of constructing the random foam core using axial symmetry.

5.2 MODEL DESIGN APPROACH

This thesis covers two parts of the foam core sandwich panel design process, the initial sizing, and the verification of the panels' performance. The initial idea for how to reduce the foam core into two dimensions was to take the mass of aluminium that would be in the foam core, and add it to the bumper and rear wall. This essentially means that we have created a Whipple shield with the same mass and thickness as the foam core panel, and therefore the BLE's for a Whipple shield can be used. Due to the simple nature of these BLE's they can also be re-arranged to find the dimensions of a Whipple shield capable of withstanding an impact with a given projectile and velocity. That Whipple shield can be transformed back to a foam core panel, giving an initial estimate for how thick the foam panel must be to withstand that same impact. The first stage of verifying this method was to compare the results of the BLE's with NASA physical data from [11]. This shows that the basic assumption of equivalency between the Whipple BLE's and foam performance is valid. Next, the equations were re-arranged to give shielding dimensions for a given impact. The re-arranged equations will then be compared to the same NASA data, to determine the accuracy of this method. This stage of the design process is discussed below in section 5.3.

Once a method that would produce results in compliance with the NASA data was found, some geometries with structures between the facesheets to represent the foam were tested, to see if the damage to the foam core could be predicted. Starting with a foam based on the Weaire-

Phelan model, which is a mathematical structure describing the geometry of foams, and slowly moving towards more abstract models [47]. Each model was first tested to see if it successfully predicted non-penetration of the rear wall. All models that showed penetration were discarded, and only successful models were examined and refined for accuracy in predicting damage to the foam core itself. Figure 5.4 shows how the actual structure of the foam core can be simplified, first to a set of random 2D ligaments, then to a Kelvin structure, and then to a set of tessellated squares. The results of the numerical experiments on various two-dimensional foam configurations are shown in section 5.4.

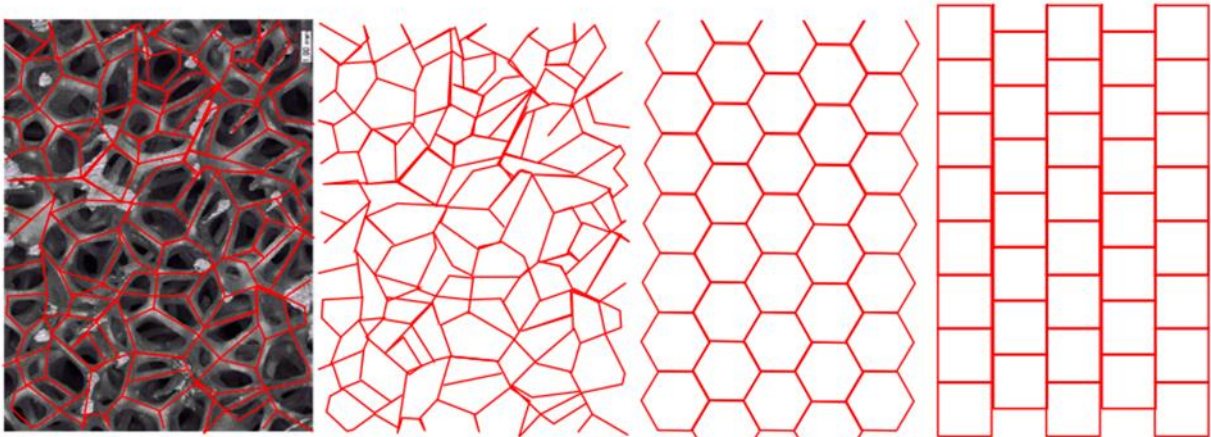


Figure 5.4: Foam reduction from realistic, randomized ligaments to simplified tessellated squares.

5.3 PENETRATION/NON-PENETRATION MATHEMATICAL MODEL

The BLE's for Whipple shields are the very well developed, and modified versions of these equations are used to describe the HVI behaviour of other shielding types, such as the honeycomb core panel [6]. We intend to use a similar approach, and use the Whipple BLE's as an initial design step to find an initial foam core thickness, which will then be refined using 2D simulations, reducing the number of simulations needed to optimize the panel thickness. TABLE IV summarizes the NASA experiments other than HITF04151 [11] which were used to validate

this approach. This set of NASA experiments were selected because they provide a range of impact conditions and shield configurations.

TABLE IV: NASA TEST DATA [11]

NASA Experiment	Projectile Velocity	Projectile Diameter	Standoff	Relative Density	PPI	Facesheet Thickness	P/NP
HITF04151	6.76 km/s	3.6 mm	50.8 mm	6-8 %	10	0.254 mm	NP
HITF04161	6.89 km/s	4.0 mm	50.8 mm	6-8 %	10	0.254 mm	P
HITF04152	6.79 km/s	3.6 mm	50.8 mm	6-8 %	40	0.254 mm	NP
HITF04163	6.79 km/s	4.0 mm	50.8 mm	6-8 %	40	0.254 mm	P
HITF03147-2	6.69 km/s	1.1 mm	12.7 mm	6-8 %	10	0.254 mm	NP
HITF03147-3	6.83 km/s	1.2 mm	12.7 mm	6-8 %	10	0.254 mm	P

Other potential means of distributing the mass from the foam core also exist. Beyond simply dividing it equally, Whipple shield design equations can be used to specify the appropriate ratio of mass in both panels. There is a design equation for both the rear wall and bumper, if designing a Whipple shield to withstand a certain impact both would be used to size the shield. When designing a Whipple shield both equations must be used, however, since in this application the total mass is constrained only one equation can be used at a time. For example, if using the formula to find the rear wall thickness, the equivalent mass of that rear wall can be found, and subtracted from the total allowable mass of the foam panel. The remaining mass can then be used to find the thickness of a bumper plate which will yield a Whipple shield of the same mass as the foam panel the calculations are based upon. The same process can be applied using the formula to find the thickness of the bumper plate, subtracting that mass to find the thickness of the rear wall. In both cases the standoff between the two plates must be known, so we select the standoff between the facesheets of the foam panel to be the standoff between the plates of the Whipple shield.

To see if the BLE's predict perforation of the shield for any of the impacts summarized in TABLE IV, we need to find the critical diameter (d_c) of each Whipple shield using equation (3) from section 2.2.1. This equation is used in the case when the normal impact velocity is between 3 and 7 km/s, which is the case for all impacts being analysed in this section. If the calculated d_c is lower than the one which impacted the foam panel, the BLE predicts that the shield will be perforated, and vice-versa. When converting a foam panel to a Whipple shield of equivalent mass we must first find the thickness of foam core if it were solid metal, this will determine the final thickness of the Whipple shield panels. Based on an assumption that the percent density of the entire foam is the average of the maximum and minimum values given by NASA, and the proportional relationship between volume and height of cylinders (axial symmetry means that two-dimensional rectangles represent three-dimensional cylinders), the equivalent solid thickness of the foam core is simply;

$$t_{foam} = \frac{\rho\%}{100} \times S \quad (26)$$

where (S) is the standoff between the front and rear facesheets in the foam panel. Adding t_{foam} to the thickness of the facesheets of the foam panel gives the maximum thickness of the two Whipple shield plates. From here the geometry of the Whipple shield can be determined in several ways. Three methods of dividing the mass were tested, even mass distribution, rear wall models, and bumper models. Even mass distribution refers to the case where the foam mass is evenly distributed between the bumper and rear wall, and the rear wall and bumper models are the cases where the Whipple shield was sized based on the equations for the rear wall and bumper respectively. Each of these cases successfully predicted non-penetration in the case of

experiment HITF04151 [11]. To calculate the thickness of the rear wall based on a specific projectile diameter the following equation should be used [6]:

$$t_w = c_w d^{0.5} (\rho_p \rho_b)^{\left(\frac{1}{6}\right)} (M_p)^{\left(\frac{1}{3}\right)} \left(\frac{V_n}{S^{0.5}}\right) \left(\frac{70}{\sigma}\right)^{0.5} \quad (27)$$

where (c_w) is a design parameter, (ρ_p) and (ρ_b) are the densities of the projectile and bumper, (V_n) is the normal projectile velocity. and (d) and (M_p) are the diameter and mass of the projectile, respectively. In this case the thickness of the bumper is determined by subtracting the thickness of the rear wall from the maximum thickness of the shield. The bumper thickness can also be calculated directly, and it is given as:

$$t_b = c_b \frac{m_p}{\rho_b} \quad (28)$$

Where (m_p) is the areal density of the projectile, and (c_b) is a parameter that changes value based on the ratio of standoff to projectile diameter. When this equation is used the thickness of the rear wall can be calculated in the same manner as finding the bumper thickness when using the rear wall equation. Both equations cannot be used at the same time because that results in a shield with greater total mass than the foam core panel.

TABLE V shows the dimensions of each of the simulated face sheets, and the results of the BLE prediction, green means that the model predicted the NASA result, red means that it did not. From the results shown in TABLE V it appears that the even mass distribution model tends to be conservative, especially with higher PPI foams, but tends to accurately predict penetration of the foam.

TABLE V: NUMERICAL SIMULATION RESULTS

NASA Experiment [11]	Even Mass Distribution			Rear Wall Formula Models			Bumper Formula Models		
	BP	RW	P/NP	BP	RW	P/NP	BP	RW	P/NP
	Thickness	Thickness		Thickness	Thickness		Thickness	Thickness	
HITF04151	2.032 mm	2.032 mm	NP	2.84 mm	1.22 mm	P	0.9 mm	3.164 mm	NP
HITF04161	2.032 mm	2.032 mm	P	2.602 mm	1.462 mm	P	1 mm	3.064 mm	NP
HITF04152	2.032 mm	2.032 mm	P	2.834 mm	1.23 mm	P	0.9 mm	3.164 mm	NP
HITF04163	2.032 mm	2.032 mm	P	2.623 mm	1.441 mm	P	1 mm	3.064 mm	NP
HITF03147-2	0.699 mm	0.699 mm	NP	0.988 mm	0.409 mm	P	0.275 mm	1.122 mm	NP
HITF03147-3	0.699 mm	0.699 mm	P*	0.921 mm	0.476 mm	P	0.3 mm	1.097 mm	NP

In TABLE V, the asterisk beside the result from the calculation based on NASA experiment HITF03147-3 means that the calculated critical diameter for that shield was very close to the diameter of the projectile that impacting it. Therefore, in some cases, a shield of this configuration may or may not be penetrated by a projectile 1.2 mm in diameter moving at 6.89km/s. We cannot know for sure because BLE's are inherently uncertain, there is a lot of variance in the experimental data used to create them, they are just the best fit to the data.

These results indicate that creating a Whipple shield with a standoff equal to the thickness of the foam panels' core, and the same mass as the foam panel to find a starting standoff is a good initial approximation. This approximation will provide accurate, if conservative results when compared to physical HVI experiments. Since the diameter and impact velocity will be specified, and the two thicknesses are the same, we can re-arrange the BLE of the Whipple shield to give an initial value for the foam panel thickness;

$$S_{initial} = \frac{\left[d - \left[\left(\frac{t \left(\frac{\sigma}{40} \right)^{0.5} + t}{(1.248 \rho_p^{0.5} \cos \theta)} \right)^{\left(\frac{18}{19} \right)} \times \left(1.75 - \frac{V_n}{4} \right) \right]}{\left(\frac{V_n}{4} - 0.75 \right) \times \left(1.071 t^{\left(\frac{2}{3} \right)} \rho_p^{\left(\frac{-1}{3} \right)} \rho_b^{\left(\frac{-1}{9} \right)} \left(\frac{\sigma}{70} \right)^{\left(\frac{1}{3} \right)} \right)} \right]^3 \quad (29)$$

The thickness of the panels is dependent on the size of the foam core, which is equal to the standoff, making this a system of two equations and two unknowns. Using these equations designers will be able to get an approximate idea of the size of panel needed, which can be refined using two or three-dimensional numerical experiments and physical tests.

Of course, not all materials have Whipple BLE's, and so this exact method cannot be applied in those cases. One advantage of two-dimensional numerical experiments is that they can be performed using any material, so long as the properties of that material are known. Simulating a Whipple shield is also much faster than simulating a foam panel. Therefore, if the material that the foam panel being designed is made of does not have a Whipple BLE, a series of quick simulations can be performed to obtain an initial panel thickness instead. To verify this theory a numerical experiment was run using an even mass distribution Whipple shield. Figure 5.5 shows that, when a Whipple shield representing the foam core panel used in NASA experiment HITF04151 [11] is simulated, the rear wall is not penetrated.

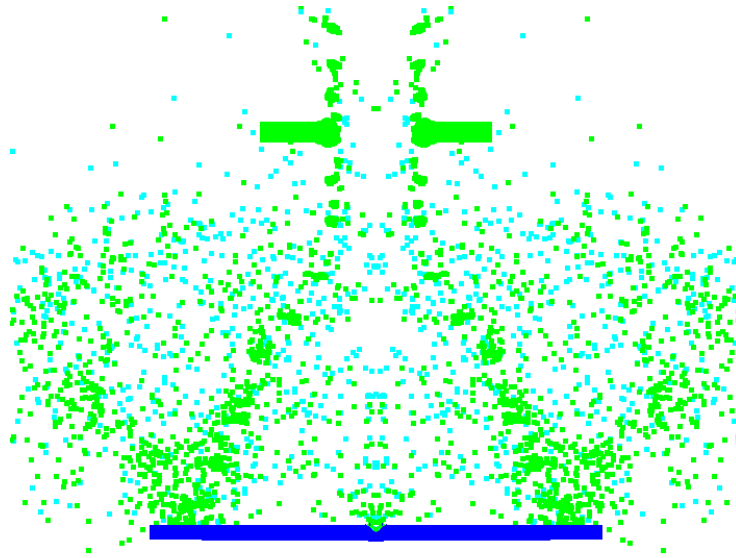


Figure 5.5: Damage pattern of Whipple design with foam core mass added equally to both facesheets

5.4 FOAM CORE PENETRATION MODELS

Once it was determined that the penetration behaviour of a foam core panel could be determined using a mass-equivalent Whipple structure, the next step was to model the damage to the foam core itself. Such an approach is more accurate than relying on BLE's, and capable of predicting the behaviour of a more diverse set of foam cores. Several different simulation designs were tested, with varying levels of complexity, including designs that were based on the mass or ligament thickness of the foam, and demonstrated foam-like behaviour. Each model was constructed using axial symmetry, as only half of the geometry needs to be modelled, and so the experiments concluded much more quickly. To determine if a simulation did not predict perforation it was run until either:

- the debris did not penetrate any new ligaments for a quarter of a microsecond,
- at least four microseconds had passed, since most failed trials showed penetration at around two microseconds, or,
- the leading edge of the debris is travelling at less than 100 m/s.

The actual geometry of the foam core was replaced in these experiments by a series of line segments. This design allows the debris to spread out after each impact, as it would in a real foam. It also has the advantage of being easy to produce and requires relatively little computing resources to simulate. Other, more complex methods of reducing the foam geometry were tested, and all had serious flaws which derived from the geometry itself.

It was found during these experiments that thin structures comprised of finite elements seem to have reduced strength along the axis of symmetry, causing the debris to penetrate much further into the foam core than expected. The final design used a simple multi-layered structure, which simulates the multi-shock action (MSA) of the foam core. This is where successive impacts on the foam ligaments further heat and break apart debris particles. The layers selected for the model were 0.36 mm thick, and separated by a gap of 5.08 mm, producing a model with half the PPI of the real foam, but the same mass. This model will be discussed in detail in section 5.4.2.

5.4.1 Model Foam with Flat Segments

While simulating impacts on the honeycomb core panels, it was seen that closed cell structures could suppress the expansion of debris cloud resulting in perforation of the rear wall, when none is expected. The entirely open nature of the configuration with short flat segments shown in Figure 5.6 allows lateral elements of the debris cloud to escape the simulation space.

This not only lessens the concentration of the debris along the impact axis, but means that some SPH particles can be deleted, speeding up the simulation. The idea behind this model was that a series of short, flat segments between the bumper and rear wall would act like the metal ligaments in a real open-cell foam core. This will cause repetitive fragmentation of the debris during the penetration process.

The thickness of the flat segments in the simulation setup was used to control the total mass of the foam. Since the density of the foam is given relative to the base material, a solid mass of metal with the same mass and diameter as a foam core of thickness S_{foam} , will have a thickness of;

$$t_{solid} = \frac{\rho\%}{100} \times S_{foam} \quad (30)$$

This is equivalent to the means of calculating the mass to be added to the Whipple shield facesheets when using the mathematical foam sizing equations derived in section 5.3. The thickness of the individual ligaments is then inversely proportional to the PPI of the foam, by the relationship;

$$t_{segment} = \frac{t_{solid}}{PPI * S_{foam}} \quad (31)$$

This allows the production of a foam that looks similar to a series of tessellated squares, but with the elements parallel to the direction of debris travel removed and correspondingly thicker ligaments perpendicular to the direction of debris travel. The number of such elements is

proposed to be equal to the number of pores in the real foam counting along a straight line perpendicular to the face sheets, this can be seen in Figure 5.6a below.

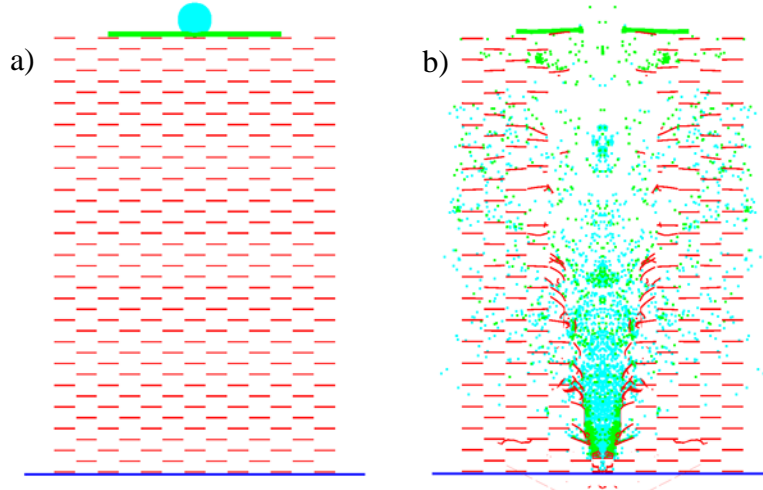


Figure 5.6: Model of foam with flat segments: setup (a) and simulation results (b)

The above model was employed to represent numerically the impact conditions of the NASA experiment HITF04151 [11] with exactly 20 foam cells across the foam, as in the real foam. A thickness of 0.18 mm was selected for all segments for the simulation based on Equations (30) and (31). The results of simulation is illustrated in Figure 5.6b where it can be seen that the numerical test outcome (perforation) differs from the physical experiments, which show non-perforation. To address the fact that short segments provide insufficient resistance to the debris cloud propagation, the multi-layer model of foam was proposed and evaluated.

5.4.2 Multi-Layer Foam Model

A simple adaptation from the foam with short flat segments, this new model uses multiple layers which span the entire width of the foam with no gaps, as shown in Figure 5.7a. This model has reduced number of elements to represent the foam which is easier to generate, and faster to run than the model with segments. As for the model with short flat segments, 20 full cells

between the two facesheets were used to simulate NASA experiment HITF04151 [11]. The thickness of each layers in Figure 5.7a was identical to the thickness of flat segments in Figure 5.6a.

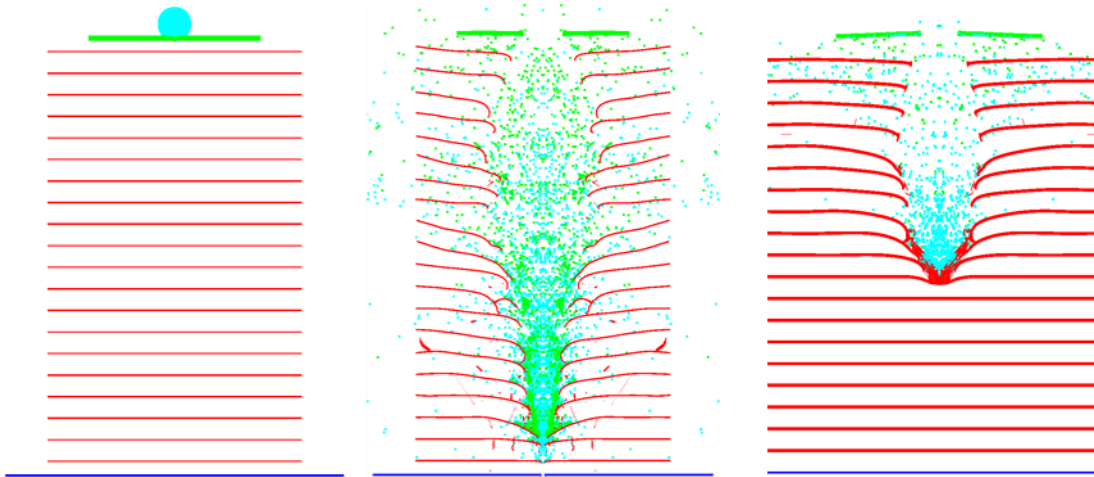


Figure 5.7: Multi-layer model of foam: setup (a) and simulation results for the equal mass model (b) and equal ligament thickness model (c)

The results of the first trial are presented in Figure 5.7b where the intermediate layers provide more significant, but still insufficient resistance to the debris compared to the foam model presented in section 5.4.1. The thicknesses of these layers were selected to make the mass of the foam equal to one in the NASA experiment. Since the material of the foam was uniformly spread over the surfaces of the layers they were thinner than the ligaments in the foam used by NASA. The ligaments thickness was measured and found to be around 0.38 mm, which is 2.1 times the thickness of the layer used in the model. Accordingly, the thickness of layers in the model was equalize to the real ligament thickness, i.e. to 0.38 mm. Figure 5.7c illustrates the results of numerical HVI test: the foam was not perforated, calculated penetration was

approximately 1.2 inches, which is 72% of the penetration seen in the NASA experiment. This indicates that the evaluated model provides excessive resistance to the penetration.

Since the foam is open-celled, it is reasonable to assume that individual debris particles will not impact all ligaments bounding the pores through which they are passing. Considering this, another iteration of the multi-layer foam model was considered with fewer layers than expected from the PPI of the foam. By test data presented in [48] the ratio of diameter of the large central fragment in the debris cloud to the diameter of the spherical aluminium projectile is slightly below 0.4. The further fragmentation due to repetitive impact with the ligaments quickly reduces this ratio as it was demonstrated in the numerical analysis performed by the University of Manitoba MMOD Protection Group [10]. The number of ligaments which individual fragment could potentially intersect on the way from the front sheet toward the rear sheet was estimated by inspecting randomly selected 0.1 mm cylindrical cross-sections cut from a three-dimensional model of 40 PPI foam, shown in Figure 5.8. The average number of ligaments encountered by the 28 cylindrical cross sections was found to be 49.21% of the total number of ligaments; based on this assessment the number of layers in the multilayer model of foam was reduced by 50%.

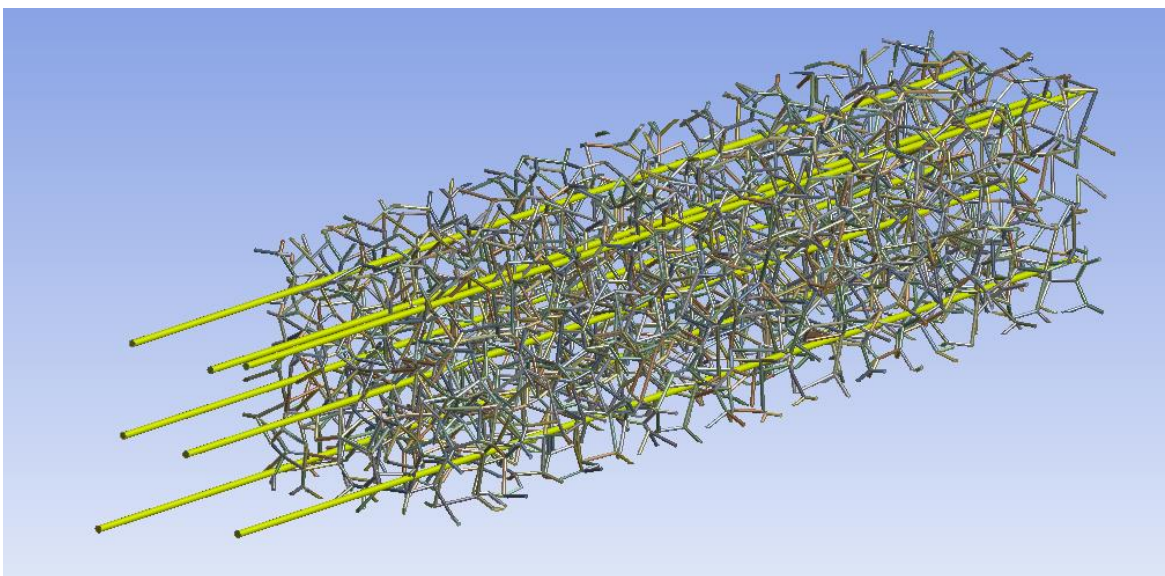


Figure 5.8: Illustration of positioning of inspection cylinders

Use of an effective PPI of 50% of the real value, using formula (31) gives a layer thickness close to the thickness of ligament, 0.36 mm. This is a major advantage when designing a new foam panel, as the engineer in question may not have a sample of the physical foam. A simulation was completed using this approach, shown in Figure 5.9, and the simulation predicted 97.5% of the penetration depth seen in the NASA experiment.

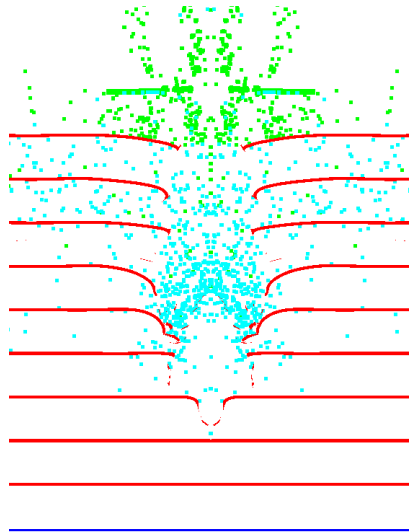


Figure 5.9 Multi-layer equal ligament thickness model of foam with effective PPI (numerical experiment representing experiment HITF04151)

5.5 CONCLUSIONS

A multi-layer model of foam was developed for simulating open-cell foams undergoing HVI events in two dimensions. The model foam has the mass of the real foam, and the layer thickness is equal to the actual thickness of the ligament. The comparison of the calculated depth of penetration with test data showed a good agreement. Further numerical experiments need to be performed for the model validation, which will be discussed in the next chapter.

6 VALIDATION OF FOAM-CORE MODELS

The mass-conserved multi-layer model with effective PPI has been established as the best candidate for two-dimensional simulations of hypervelocity impacts on metal foam core sandwich panels. Before it can be recommended for use by design engineers the proposed foam model should be validated and modified (if necessary) using available data. The results of HVI tests conducted by NASA on aluminium foam core panels [11] were used for the numerical analysis. These results were paired, one that is expected to penetrate the target and one which is not. The details of these numerical experiment are presented below.

6.1 10 PPI FOAM

The experiment HITF04151 simulated in chapter 5 (Figure 5.9) is paired with HITF04161, summarized in TABLE VI, which used the same foam but was penetrated by a 4mm particle moving at 6.89 km/s.

TABLE VI: VALIDATION DATA [10] FOR 10 PPI AND 2.0"-THICKNESS FOAM-CORE PANELS

NASA Experiment	Projectile Velocity	Projectile Diameter	Standoff	Relative Density	PPI	Facesheet Thickness	P/NP
HITF04151	6.76 km/s	3.6	50.8	6-8 %	10	0.254 mm	NP
HITF04161	6.89 km/s	4.0	50.8	6-8 %	10	0.254 mm	P

The result of numerical experiment representing test HITF04161 is illustrated in Figure 6.1a. Since in the numerical experiment the rear sheet of the panel was perforated primarily by the action of degenerate finite elements, it is believed that it corresponds to the perforation slightly above the ballistic limit. Figure 6.1b shows that after test HITF04161 the rear wall was penetrated in two places, both with a very small diameter. This supports the theory that the impact is only slightly above the ballistic limit.

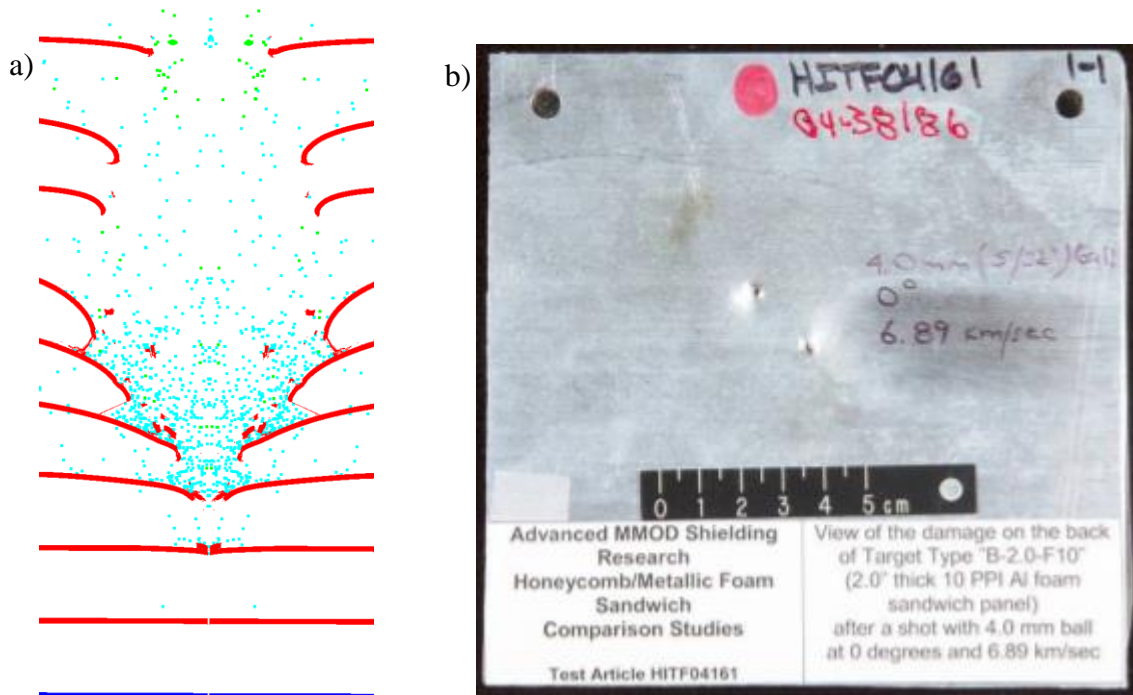


Figure 6.1: Numerical experiment representing test HITF04161 (a) Rear wall of foam panel used in test HITF04161 [10] (b) -NASA

Two more NASA tests (HITF3147-2 and HITF3147-3) with a 10 PPI foam core were simulated, and these tests are summarised in TABLE VII. The experiments were performed on half-inch sandwiches, and because of this they can be completed in a few hours. Compared to a week to complete a simulation of a two-inch foam core using the same method, and over a month to simulate a 16 mm foam core in three dimensions, this is significantly faster.

TABLE VII: VALIDATION DATA [10] FOR 10 PPI AND 0.5"-THICKNESS FOAM -CORE PANELS

NASA Experiment	Projectile Velocity	Projectile Diameter	Standoff	Relative Density	PPI	Facesheet Thickness	P/NP
HITF03147-2	6.89 km/s	1.1 mm	12.7 mm	6-8 %	10	0.254 mm	NP
HITF03147-3	6.83 km/s	1.2 mm	12.7 mm	6-8 %	10	0.254 mm	P

Immediately when setting up the foam model for the half-inch 10 PPI foam core there is a small problem. Halving the PPI would lead to the need for 2.5 gaps, and since it is impossible to create half a gap the experiment was simulated twice. First with one layer and second with two, to determine if rounding up or down is better in this case. The simulation with one layer had a layer 0.889 mm thick, halfway between the front and rear facesheets. Using only one layer, both numerical experiments representing HITF03147-2 and HITF03147-3 tests showed non-perforation, where the perforation is expected in case of HITF03147-2, based on the results of the physical test. The results of both numerical experiments can be seen in Figure 6.2 below, in both cases the simulation was ended because the debris reached a velocity lower than 100 m/s along the leading edge. While there was more damage done to the layer in HITF03147-3, there was no damage done to the rear wall.

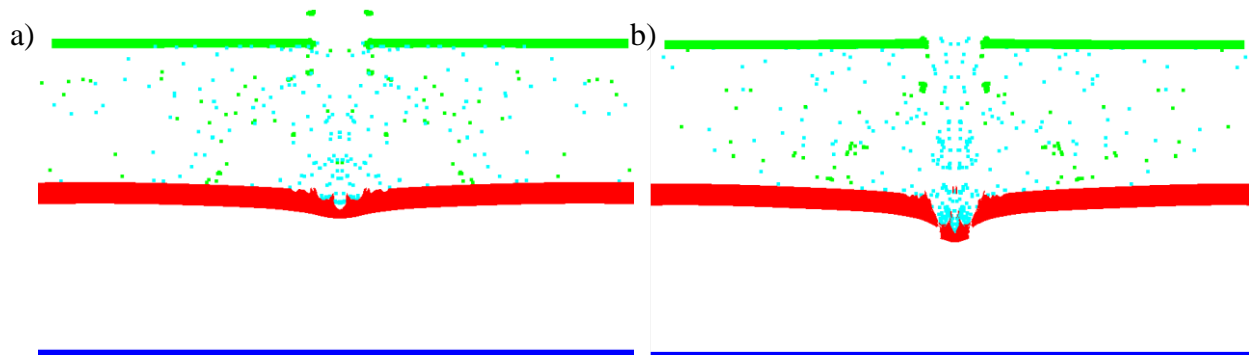


Figure 6.2: One-layer simulation results of HITF03147-2 (a) and HITF03147-3 (b)

The results of the two-layer model are significantly better, each numerical experiment corresponds to the physical test data [11]. Figure 6.3 shows the extent of the damage to both simulated foams, the layers in these simulations are 0.44 mm thick, spread evenly within the foam. The simulation of HITF03147-2 was run for longer to ensure that the large pieces of foam were not going to break through. The impact and resulting deformation of the rear wall in this simulation indicate that this experiment was probably very close to the ballistic limit, in fact the projectile is moving faster than in HITF03147-3 [11], it is just smaller. Similarly, the simulation of test HITF03147-3 [11] allows concluding that the relatively small damage of the rear wall indicates that this experiment would be just above the ballistic limit.

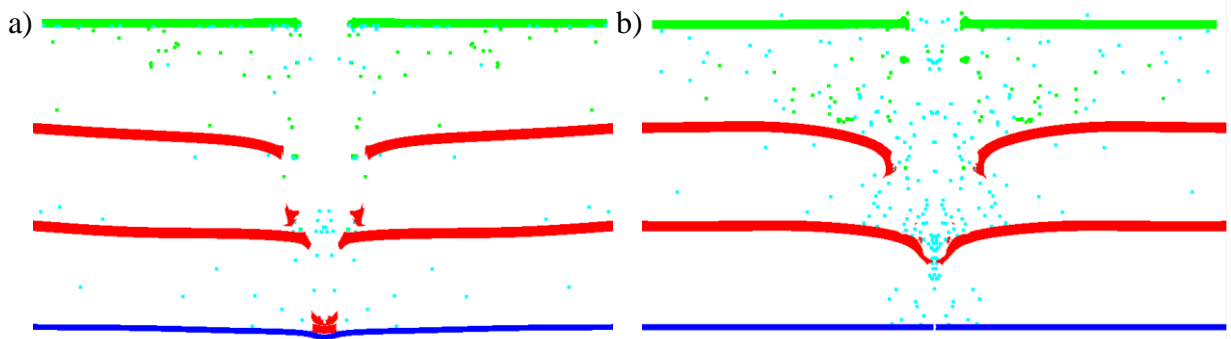


Figure 6.3: Two-layers simulation results of HITF03147-2 (a) and HITF03147-3 (b)

These four experiments show that the mass-conserved multi-layer model with half PPI can accurately predict the results of NASA experiments on 10 PPI half-inch foam samples as well as two-inch samples. The simulations also demonstrated that rounding the number of pores up in the case of needing half a pore produces more accurate results than rounding down.

6.2 40 PPI FOAM

To see if this model would work with foams with higher PPI values, two sets of simulations were conducted. The first set was based on NASA trials HITF04152 and HITF04163, with 40 PPI and were two inches thick, these tests are summarized in TABLE VIII below. The foam core was constructed using 39 layers, 0.098 mm in thickness which were spread evenly to create forty pores. While the simulation of HITF04152 was run longer than the simulation of HITF04163, we can see from Figure 6.4 that the debris did not penetrate as deeply into the foam core. In Figure 6.4b, SPH particles did in fact perforate the entire panel, and the bulk of the debris is much closer to the rear wall than in Figure 6.4a. Also, the debris at the leading edge of the HITF04163 numerical experiment is still moving faster than the debris in HITF04152, despite its greater penetration depth.

TABLE VIII: VALIDATION DATA [10] FOR 40 PPI AND 2.0"-THICKNESS FOAM -CORE PANELS

NASA Experiment	Projectile Velocity	Projectile Diameter	Standoff	Relative Density	PPI	Facesheet Thickness	P/NP
HITF04152	6.79 km/s	3.6 mm	50.8 mm	6-8 %	40	0.254 mm	NP
HITF04163	6.79 km/s	4.0 mm	50.8 mm	6-8 %	40	0.254 mm	P

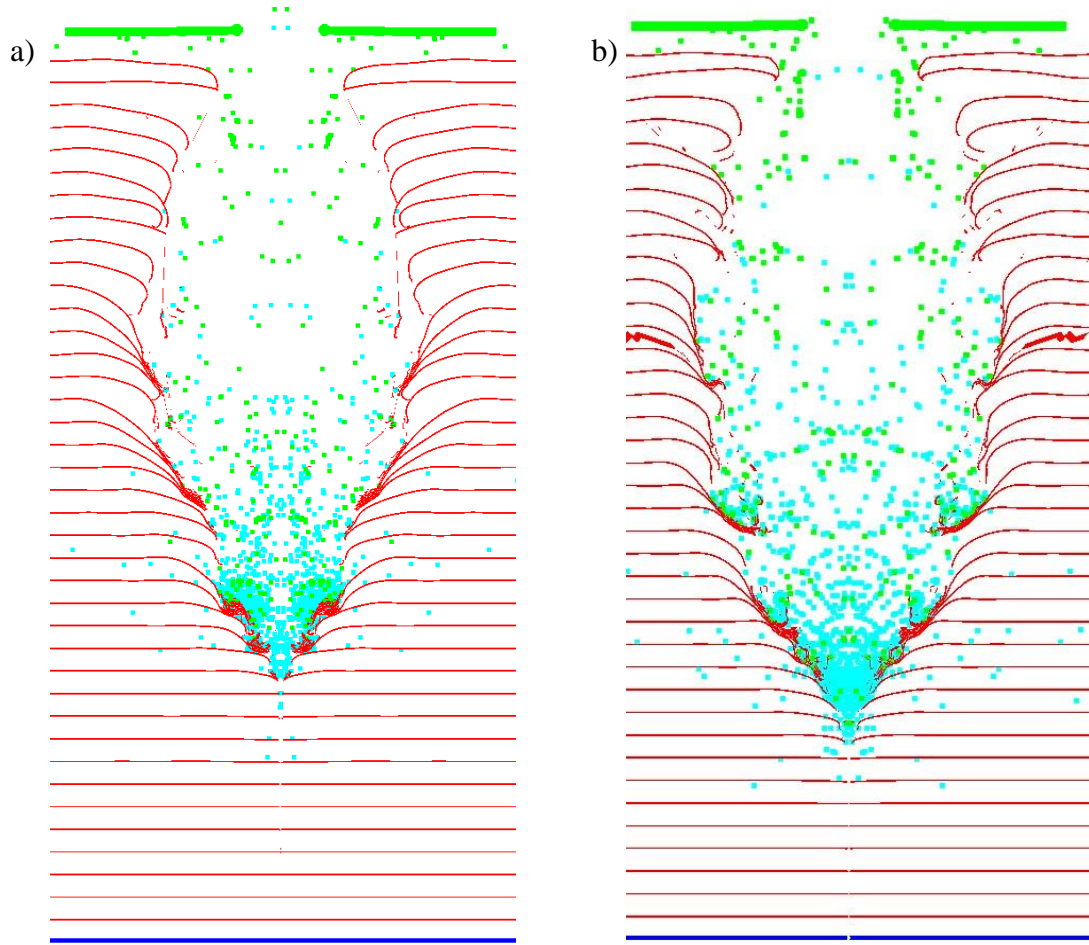


Figure 6.4: Simulation results of HITF04152 (a) and HITF04163 (b)

For simulating another two selected NASA experiments HITF05036-2 and HITF05036-3 with 40 PPI, as summarized in TABLE IX, the mass of the foam was broken into nine layers of 0.098 mm thickness. These layers were spread equally between the rear wall and the bumper to create ten pores. Since the ligament thickness for 40 PPI foam was not indicated in [10], it was assumed to be 25% of the 10 PPI foam ligament thickness, we believe that this is a reasonable assumption because the relative density of the foam is the same, but there are four times as many ligaments.

TABLE IX: VALIDATION DATA [10] FOR 40 PPI AND 0.5"-THICKNESS FOAM -CORE PANELS

NASA Experiment	Projectile Velocity	Projectile Diameter	Standoff	Relative Density	PPI	Facesheet Thickness	P/NP
HITF05036-2	6.90 km/s	1.2 mm	12.7 mm	6-8 %	40	0.254 mm	NP
HITF05036-3	6.45 km/s	1.4 mm	12.7 mm	6-8 %	40	0.254 mm	P

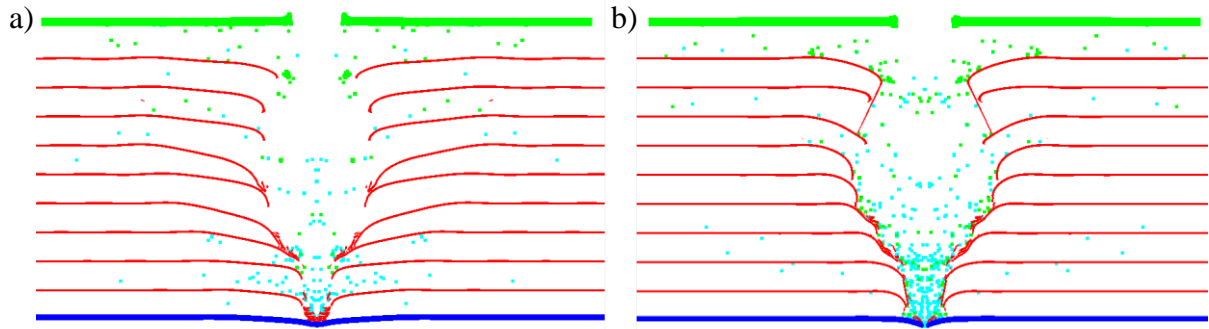


Figure 6.5: Simulation results of HITF05036-2 (a) and HITF05036-3 (b)

Both simulations concluded as expected from the NASA experiments: non-perforation for test HITF05036-2 (Figure 6.5a) and perforation for the HITF05036-3 (Figure 6.5b). As with the two-layer simulation of HITF03147-2, the simulation of HITF05036-2 was run for an extended period to ensure that the rear wall was not penetrated. Thus, it can be concluded that the mass-conserved multi-layer model of foam with effective PPI successfully predicts perforation or non-perforation of the foam, however, the shape of the simulated damage in the foam is narrower in comparison with the experimental data.

6.3 CONCLUSIONS

First in this chapter a simple method to determine an initial standoff when designing a foam core panel to withstand HVI was found. Using the BLE's for an aluminium Whipple shield, which is the most well-studied set of BLE's, a good initial approximation of the necessary foam core size to resist a specific impact can be found. From here, design engineers can proceed with simulating the initial model in two dimensions, using the model also described in this chapter.

To find an appropriate geometry to represent a foam core in two dimensions, eight NASA experiments were simulated. These experiments show that the simplified 2D foam geometry that best represents the behaviour of an aluminium foam core sandwich panel is mass-conserved multi-layer model with effective PPI. This model allows to accurately predict the HVI test outcome in a time frame ranging from a few hours to a week. Compared to over a month for even a small three-dimensional simulation, it is clear why this method is superior for initial foam design, whereas the three-dimensional simulations provide more detailed results, which is better for further testing of an already designed panel.

7 CONCLUSIONS AND FUTURE WORK

This thesis was written with the intent of answering three questions;

- How should the numerical simulation technique be selected and calibrated to properly simulate HVI events?
- Which combinations of material model components are most effective when simulating HVI events?
- Can known impacts involving honeycomb and foam-core sandwich panels be recreated in a two-dimensional numerical experiment?

Each of these questions was answered while conducting research for this thesis, and the conclusions drawn will be presented below. It can be said that, with this thesis, it was shown that non-symmetric multifunctional panels undergoing HVI can be simulated in two dimensions, with minimal losses in accuracy.

7.1 CONCLUSIONS AND CONTRIBUTIONS

- A new approach for simulating the foam-core sandwich panels in two dimensions was developed. It was demonstrated that a 2D multi-layer model can be used to represent the actual foam core of equivalent mass accurately predicting the outcome of HVI on aluminium foam core panels.
- The developed method is faster than using a three-dimensional simulation, and less expensive to use than physical experiments, satisfying the objectives of this thesis. A 0.5 inch foam core panel undergoing HVI can be simulated in a day of computer time using this model, compared to two months for an equivalent three-dimensional simulation.
- The parameters of the numerical model, as well as, SPH particle size and erosion factor, were calibrated. It was found that the best SPH particle size varied depending on whether the simulation was being conducted in two or three dimensions. In two dimensions, an SPH particle size of 0.015 mm provided the best balance between accuracy and simulation run time. In three dimensions, the best SPH particle size was found to be 0.06 mm, as there are exponentially more SPH particles in a three-dimensional simulation. The unitless erosion factor, which determines when deformed finite elements are removed from the simulation, was found to be 1.5. The above parameters were used in all numerical experiments.
- Six combinations of material model components were evaluated, comparing the numerical results with test data such as impact hole diameter, debris cloud shape, and rear wall damage. It was found that the Johnson-Cook strength and failure models, with a Mie-Gruneisen equation of state best modelled the behaviour of aluminium being impacted at hypervelocity.

- The selected computational parameters and material model were applied to validate the two-dimensional model of honeycomb-core sandwich panels. It was found that, while the two-dimensional model would predict perforation of the rear wall as expected, it did not fully model the damage to the core structure.
- The developed numerical model was validated using HVI test data and proved to be suitable for the analysis and design of foam-core sandwich panel with enhanced capability for orbital debris protection.

7.2 LIMITATIONS OF THE ANALYSIS

This thesis was conducted using only 6061-T6 aluminium, being impacted within the fragmentation and partial melt regime, between 3-7 km/s [6]. Simulation of foam-core panels made from other materials, or being impacted at speeds outside this regime will require that all the steps outlined in chapter 3 this thesis be repeated. It is known that the Johnson-Cook strength and failure models do not represent phase changes well, so it is very likely that other equations must be used for modelling impacts at higher velocities.

This model also cannot be used to simulate impacts at angles other than 90° to the panel, nor projectiles that are not axially symmetric. This is a limitation of the axial symmetry model, where the entire simulation space is duplicated along the axis of symmetry ($y=0$). The use of planar symmetry was investigated to overcome this limitation, but it was found that the simulated projectiles impacted the panel with too much energy.

Finally, it should be noted that the time to simulate larger models can still be in the range of 2-4 weeks. Foams more than 2 inches thick and with more than 40 PPI can be expected to take

over a month to complete. Note that this is still much faster than performing the simulation in three dimensions, but is a notable limitation.

7.3 FUTURE WORK

The developed multi-layer model of foam successfully predicts perforation or non-perforation of the foam, however, the shape of the simulated damage in the foam is narrower in comparison with the experimental data. This discrepancy occurs since flat layers representing the ligaments bend during the debris penetration. Besides, the off-axis fragments of debris cloud must expend more energy to pass through a layer since their path through the layer is longer, as illustrated in Figure 7.1. These factors prevent the lateral expansion of debris cloud forming a channel-like damage.

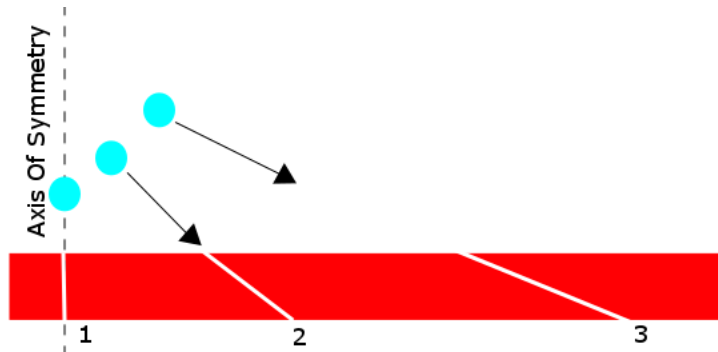


Figure 7.1: Paths of off-axis fragments through the layer of multilayer model of foam

The curving the ligaments seems a possible way to mitigate this problem. Figure 7.2 shows an example with an exaggerated curve, in reality it is likely that the radius of curvature will change for each layer. Finding the exact arc that means that fragments will impact the layers at the angle close to normal incidence is viewed to be the direction for further research. This model will bring the appearance of the damage to the foam core more in line with what is expected based on NASA test data.

One major limitation of the model presented in this thesis is that it can only simulate impact angles of 90° to the bumper. It is assumed that modification of numerical test setup as shown in Figure 7.3 could make it applicable for simulation of the oblique impact. This will require the implementation of planar symmetry in the model.

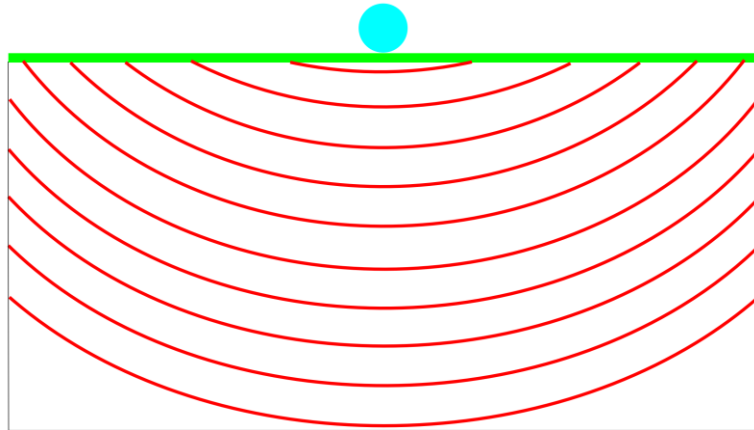


Figure 7.2: Illustration of curved layered design

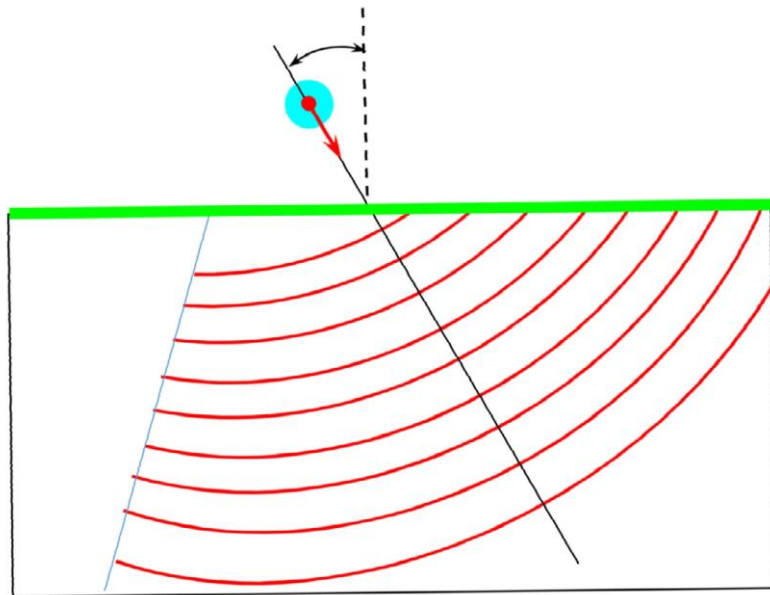


Figure 7.3: Application of curved layered design to simulation of oblique impact

One advantage of using numerical experiments to test HVI shielding performance was not addressed by this report, it is very difficult to use non-spherical projectiles in physical HVI tests,

yet few MMOD particles will be spherical. A future report could address the effect of projectile shape on foam-core panel HVI performance.

Similarly, other materials should be tested for the projectile and foam panel composition, requiring further research into the applicable material equations. Using SPH particles to generate the foam layers is an option for future research, but current limitations within Autodyn prevent so many SPH particles from being used in one simulation.

REFERENCES

- [1] National Research Council, *Orbital Debris - A Technical Assessment*, Washington D.C.: National Academy Press, 1995.
- [2] IADC WG3 Members, *Protection Manual, Inter-Agency Space Debris Coordination Committee*, 2012.
- [3] M. Capderou, *Satellites: Orbits and Missions*, Paris: Springer, 2005.
- [4] M. Capderou, *Handbook of Satellite Orbits: From Kepler to GPS*, Paris: Springer, 2014.
- [5] P. Fortescue, L. Mottershead, G. Swinerd and J. Stark, *Spacecraft Systems Engineering*, John Wiley and Sons, 2003.
- [6] E. Christiansen, "Handbook for Designing MMOD Protection," NASA, Houston, 2009.
- [7] J. West, "Space Security Index 2016," Pandora Press, Kitchener, 2016.
- [8] NASA Orbital Debris Program Office, *Orbital Debris Quarterly News*, vol. 17, no. 1, p. 8, January 2013.
- [9] E. Christiansen, S. Ryan and D. Lear, "Development of the Next Generation of Meteoroid and Orbital Debris Shields," NASA, Houston.

- [10] A. Cherniaev and I. Telichev, "Weight-Efficiency of Conventional Shielding Systems in Protecting Unmanned Spacecraft from Orbital Debris," *Journal of Spacecraft and Rockets*, vol. 54, no. 1, pp. 75-89, 13 July 2017.
- [11] J. Yasensky, "Hypervelocity Impact Evaluation of Metal Foam Core Sandwich Structures," NASA, Houston, 2007.
- [12] S. Ryan, E. Christiansen and D. Lear, "Development of the Next Generation of Meteoroid and Orbital Debris Shields," NASA, Houston.
- [13] W. Rae, T. Riney, J. Taylor and J. Walsh, *High-Velocity Impact Phenomena*, New York: Academic Press, 1970.
- [14] J. Zukas, *Introduction to Hydrocodes*, Baltimore: Elsevier Direct, 2004.
- [15] C. Belk, J. Robinson, M. Alexander, W. Cooke and S. Pavelitz, "Meteoroids and Orbital Debris: Effects on Spacecraft," NASA, 1997.
- [16] E. Christiansen, "Meteoroid/Debris Shielding," NASA, Houston, 2003.
- [17] S. Dodge, "Orbital Debris Management and Risk Mitigation," NASA, 2012.
- [18] F. Whipple, "Meteorites and Space Travel," *The Astronomical Journal*, vol. 52, p. 131, 1947.
- [19] J. Crews, E. Christiansen, J. Williamsen, J. Robinson and A. Nolen, "Enhanced Whipple Shield". US Patent 5,610,363, 15 February 1995.
- [20] K. McClymonds, "Spacecraft Shield". US Patent 5,601,258, 25 July 1994.

- [21] E. Christiansen, "Advanced Meteoroid and Debris Shielding Concepts," in *DOD Orbital Debris Conference: Technical Issues and Future Directions*, Baltimore, 1990.
- [22] E. Christiansen and J. Kerr, "Mesh Double-Bumper Shield: A Low-Weight Alternative for Spacecraft Meteoroid and Orbital Debris Protection," *International Journal of Impact Engineering*, no. 14, pp. 169-180, 1993.
- [23] B. Cour-Palais and J. Crews, "Hypervelocity Impact Shield". US Patent 5,067,388, 26 November 1991.
- [24] B. Cour-Palais and J. Crews, "A Multi-Shock Concept for Spacecraft Shielding," *International Journal of Impact Engineering*, no. 10, pp. 95-106, 1993.
- [25] R. Bigelow, "Orbital Debris Shield". US Patent 7,309,049 B2, 18 December 2007.
- [26] A. Jones, "Conceptual Design of Space Platform for Refueling and Servicing of Satellites," University of Manitoba, Winnipeg, 2014 - Undergraduate Thesis.
- [27] S. Ryan, T. Hedman and E. Christiansen, Honeycomb vs. Foam: Evaluating a Potential Upgrade to International Space Station Module Shielding for Micrometeoroids and Orbital Debris, NASA, 2009.
- [28] S. Ryan, E. Ordonez, E. Christiansen and D. Lear, "Hypervelocity Impact Performance of Open Cell Foam Core Sandwich Panel Structures," in *Proceedings of the 11th Hypervelocity Impact Symposium*, Frieberg, 2010.

- [29] S. Hiermaier, *Structures Under Crash and Impact: Continuum Mechanics, Discretization and Experimental Characterization*, Springer, 2008.
- [30] L. Dursi, “Computation in Astrophysics Seminar,” University of Toronto, Toronto, 2006.
- [31] ANSYS, *Explicit Dynamics Lecture 1: Introduction to Explicit Dynamics*, 2011.
- [32] V. Springel, “High performance computing and numerical modeling,” Heidelberg University, Heidelberg, 2013.
- [33] M. Liu and G. Liu, “Smoothed Particle Hydrodynamics (SPH): an Overview and Recent Developments,” *Archives of Computational Methods in Engineering*, no. 17, pp. 25-76, 2010.
- [34] V. Nguyen, T. Rabczuk, S. Bordas and M. Duflot, “Meshless methods: a review and computer implementation aspects,” *Mathematics and Computers in Simulation*, vol. 79, no. 3, pp. 763-813, 2008.
- [35] ANSYS, *Explicit_STR Lecture 6: Material Models*, 2012.
- [36] T. Ahren, “Equation of State,” in *High-Pressure Shock Compression of Solids*, New York, Springer-Verlaug, 1993, pp. 75-113.
- [37] J. Tillotson, “Metallic Equations of State for Hypervelocity Impact,” Department of Defence, 1962.
- [38] H. Chen, W. Tang, J. She, X. Ran and Z. Xu, “The PUFF Equation of State Parameters for Synthetc Rubber,” *Mechanics of Materials*, no. 43, pp. 69-74, 2010.

- [39] G. R. Johnson and W. H. Cook, "A Constitutive Model and Data for Metals Subjected to Large Strains, High Strain Rates and High Temperatures," in *Proceedings of the 7th International Symposium on Ballistics*, 1983.
- [40] J. Fish, C. Oskay and R. Fan, "AL 6061-T6 - Elastomer Impact Simulations," Rensselaer Polytechnic Institute, Troy, 2005.
- [41] J. Peng, C. Hu, Y. Li, L. Zhang and F. Jing, "Determination of Parameters of Steinberg-Guinan Constitutive Model with Shock Wave Experiments," *International Journal of Modern Physics*, vol. 22, pp. 1111-1116, 2008.
- [42] D. Steinberg, "A Rate-Dependant Constitutive Model for Molybdenum," *Journal of Applied Physics*, vol. 74, no. 3, pp. 3827-3831, 1993.
- [43] W. Dabboussi and J. Nemes, "Modeling of ductile fracture using the dynamic punch test," *International Journal of Mechanical Sciences*, no. 47, pp. 1282-1299, 2005.
- [44] D. Lesuer, G. Kay and M. LeBlance, "Modelling Large-Strain, High-Rate Deformation in Metals," in *Third Biennial Tri-Laboratory Engineering Conference*, Pleasanton, 2001.
- [45] A. Cherniaev, "Design and Analysis of Orbital Debris Protection for Spacecraft Composite Pressure Vessels," University of Manitoba, Winnipeg, 2016 - PhD Thesis.
- [46] M. Matney, "NASA's Orbital Debris Environment Model ORDEM 3.0," [Online]. Available: <https://ntrs.nasa.gov/archive/nasa/casi.ntrs.nasa.gov/20150003495.pdf>. [Accessed 06 11 2017].

[47] D. Weaire and R. Phelan, "A counter-example to Kelvin's conjecture on minimal surfaces," *Philosophical Magazine Letters*, vol. 69, no. 2, pp. 107-110, 1994.

[48] A. Piekutowski, "Effects of scale on debris cloud properties," *International Journal of Impact Engineering*, vol. 20, no. 6-10, pp. 639-650, 1997.

Appendix A: Unused Material Models

CONTENTS

1	Material Models	A1
1.1	Equation of State	A1
1.2	Strength	A2
1.3	Failure	A3
	References	A4

1 MATERIAL MODELS

Autodyn has a large database of material models, including equations of state, strength models, and failure models [1]. Analysing all possible combinations would take far too long, however some material models are inappropriate for the research being conducted, and so can be eliminated. Autodyn also contains a reference document that describes the uses of each model, and so inappropriate models could be identified quickly. All models that were not considered for use during this thesis are listed below, along with the reason they were eliminated. For all models without a separate citation, the source of the information is [1].

1.1 EQUATION OF STATE

The unused equations of state listed for use in Autodyn are as follows:

- **Linear** EOS is not appropriate for systems involving penetration of objects [2].
- **Polynomial** EOS is a more basic Mie-Gruneisen EOS than the model used. [2].
- **SESAME** database is not available to the University of Manitoba Team.
- **Two Phase** EOS is appropriate only for liquid/vapour systems [3].
- **Ideal Gas** EOS is appropriate only for polytropic gas systems [2].
- **JWL** EOS is appropriate only for explosive materials [4].
- **Lee-Tarver** EOS is appropriate only for explosive/combustible materials [5].
- **Powder Burn** EOS is appropriate only for explosive/combustible materials [6].
- **Porous** EOS is appropriate only for porous materials.
- **Compaction** EOS is appropriate only for porous materials [7].
- **P alpha** EOS is appropriate only for porous materials [8].

- **Ortho** EOS is appropriate only for linear-elastic systems.
- **Rigid** EOS is appropriate only for non-deformable bodies.
- **Hyperelastic** EOS is appropriate only for nearly incompressible, hyperelastic materials.

1.2 STRENGTH

The unused strength models listed for use in Autodyn are as follows;

- **Elastic** strength is appropriate only for elastic only deformation.
- **Viscoelastic** strength is appropriate only for strain-dependant elastic deformation.
- **Von Mises** strength is not appropriate for systems with strain hardening, strain rate sensitivity or thermal softening.
- **Piecewise JC** is a different formulation of Johnson-Cook strength.
- **Zerilli Armstrong** Insufficient data for aluminium alloy used in these experiments.
- **Cowper Symonds** strength is not appropriate for temperature-dependent systems [9].
- **Drucker-Prager** strength is appropriate only for brittle and granular materials [2].
- **MO Granular** strength is appropriate only for brittle and granular materials.
- **Johnson-Holmquist** strength is appropriate only for brittle and granular materials [10].
- **RHT Concrete** strength is appropriate only for brittle and granular materials [11].
- **Beam-Resistance** strength is appropriate only for simplified beam elements.
- **Orthotropic Yield** strength is appropriate only for composite materials.
- **Crushable Foam** strength is appropriate only for bulk porous foam.
- **Hyperelastic** strength is appropriate only for nearly incompressible, hyperelastic materials.
- **Bilinear Hardening** strength is not appropriate for temperature-dependent systems.

- **Multilinear Hardening** strength is not appropriate for temperature-dependent systems.

1.3 FAILURE

The unused failure models listed for use in Autodyn are as follows;

- **Hydro (Pmin)** is appropriate only for tensile failures.
- **Plastic Strain** is appropriate only for instantaneous failures.
- **Principal Stress** is appropriate only for instantaneous failures.
- **Principal Strain** is appropriate only for instantaneous failures.
- **Principal Stress/Strain** is appropriate only for instantaneous failures.
- **Material Stress** is appropriate only for composites.
- **Material Strain** is appropriate only for composites.
- **Material Stress/Strain** is appropriate only for composites.
- **Cumulative Damage** is appropriate only for brittle materials [12].
- **Johnson Holmquist** is appropriate only for brittle and granular materials [10].
- **RHT Concrete** is appropriate only for brittle and granular materials [11].
- **Tsai/Hoffman/Hill** models are appropriate only for composite materials [13].
- **Grady Spall Model** is appropriate only for modelling spall [14].
- **Orthotropic Softening** is appropriate only for composite materials [15].
- **MO Granular** is appropriate only for brittle and granular materials.

REFERENCES

- [1] ANSYS Academic Research Mechanical, *Autodyn User Manual, Release 17.1, Help System*.
- [2] S. Hiermaier, *Structures Under Crash and Impact: Continuum Mechanics, Discretization and Experimental Characterization*, Springer, 2008.
- [3] K. Morgan, "An Expansion Equation of State Subroutine," *Computer Physics Communications*, vol. 5, no. 1, pp. 64-68, 1973.
- [4] A. Hodgson and C. Handley, "DSD/WBL-Consistent JWL Equations of State for EDC35," in *AIP Conference Proceedings*, Reading, 2012.
- [5] E. Lee and C. Tarver, "Phenomenological Model of Shock Initiation in Heterogeneous Explosives," *Physics of Fluids*, vol. 23, no. 12, pp. 2362-2372, 1980.
- [6] A. Atwood, E. Friis and M. J., "A Mathematical model for Combustion of Energetic Powder Materials," in *34th International Conference of ICT*, 2003.
- [7] W. Chen and S. Malghan, "Investigation of Compaction Equations for Powders," *Powder Technology*, vol. 81, no. 1, pp. 75-81, 1994.
- [8] W. Herrmann, "Constitutive Equation for the Dynamic Compaction of Ductile Porous Materials," *Journal of Applied Physics*, vol. 40, no. 6, pp. 2490-2499, 1969.

- [9] C. Hernandez, A. Maranon, I. Ashcroft and J. Casas-Rodriguez, "A Computational Determination of the Cowper-Symonds Parameters from a Single Taylor Test," *Applied Mathematical Modelling*, vol. 37, no. 7, pp. 4698-4708, 2013.
- [10] T. Holmquist and G. Johnson, "The Failed Strength of Ceramics Subjected to High-Velocity Impact," *Journal of Applied Physics*, vol. 104, no. 1, 2008.
- [11] W. Riedel, *Predictive Modelling of Dynamic Processes*, Springer, 2009.
- [12] S. Durham and W. Padgett, "Cumulative Damage Models for System Failure With Application to Carbon Fibres and Composites," *Technometrics*, vol. 39, no. 1, pp. 34-44, 1997.
- [13] P. Camanho, "Failure Criteria for Fibre-Reinforced Polymer Composites," 2002. [Online]. Available: <https://web.fe.up.pt/~stpinho/teaching/feup/y0506/fcriteria.pdf>. [Accessed 03 06 2016].
- [14] D. Grady, "Solutions of Spall and Fragmentation of Solids," in *AIP Conference Proceedings*, Albuquerque, 2006.
- [15] P. Camanho, C. Davila, S. Pinho and J. Remmers, *Mechanical Response of Composites*, Springer, 2008.